Adding a Novel Material to the 2D Toolbox: Properties and Transfer of a Silica Bilayer

Dissertation zur Erlangung des akademischen Grades
doctor rerum naturalium
(Dr. rer. nat.)
im Fach Chemie

eingereicht an der
Mathematisch-Naturwissenschaftlichen Fakultät
der Humboldt-Universität zu Berlin

von
Dipl.-Chem. Christin Büchner

Präsident der Humboldt-Universität zu Berlin:

Prof. Dr. Jan-Hendrik Olbertz

Dekan der Mathematisch-Naturwissenschaftlichen Fakultät:

Prof. Dr. Elmar Kulke

Gutachter/innen: 1. Prof. Dr. Hans-Joachim Freund

2. Prof. Dr. Klaus Rademann

3. Prof. Dr. Bodil Holst

Tag der mündlichen Prüfung: 20.05.2016

Diese Dissertation wurde in der Abteilung Chemische Physik am Fritz-Haber-Institut der Max-Planck-Gesellschaft, unter der Anleitung von Prof. Dr. Hans-Joachim Freund, in der Arbeitsgruppe Rastersondenmikroskopie, Gruppenleiter Dr. Markus Heyde, angefertigt.

We are forever balancing on the shoulders of giants.

Abstract

The library of two-dimensional (2D) materials is limited, since only very few compounds remain stable when they consist of only surfaces. Yet, due to their extraordinary properties, the hunt for new 2D materials continues. Recently, an atomically defined, self-saturated SiO_2 bilayer has been prepared on several metal surfaces. This ultrathin silica sheet would be a promising addition to the family of 2D materials, if it can be isolated from its growth substrate without compromising its structure.

In this work, we explore the properties of a silica bilayer grown on Ru(0001) in the context of 2D technology applications. The bilayer sheet exhibits crystalline and amorphous regions, both being atomically flat. The crystalline region possesses a hexagonal lattice with uniform pore size, while the amorphous region requires a more complex description. In a building block study of the amorphous region, we find that medium range structural patterns correlate with a parameter describing the bond angle frustration. The resulting network of different nanopores represents a size-selective membrane, as illustrated in an adsorption study. Pd and Au atoms are shown to penetrate the silica film selectively, depending on the presence of appropriately sized nanopores.

The ultrathin silica film is shown to withstand exposure to different solvents and the stability of the structure in water is analyzed. These studies indicate extraordinary stability of this nanostructure.

We develop a polymer assisted mechanical exfoliation method for removing the film from the growth substrate, providing evidence that the film is removed as an intact sheet from the growth substrate. We subsequently present the transfer of the silica bilayer to a TEM grid, where it forms micro-ribbons. Further, the film is transferred to a Pt(111) substrate, where mm-scale transfer under retention of the structure is achieved.

Zusammenfassung

Die Sammlung der zwei-dimensionalen (2D) Materialien ist begrenzt, da sehr wenige Verbindungen stabil bleiben, sobald sie nur aus Oberflächen bestehen. Aufgrund ihrer außergewöhnlichen Eigenschaften sind 2D Materialien jedoch nach wie vor überaus begehrt. Vor kurzem wurden atomar definierte, chemisch gesättigte SiO_2 Bilagen auf verschiedenen Metalloberflächen präpariert. Eine solche ultradünne Silika-Lage wäre eine vielversprechende Ergänzung zur Familie der 2D Materialien, wenn sie vom Wachstumssubstrat isoliert werden kann, ohne die Struktur zu beeinträchtigen.

In dieser Arbeit untersuchen wir die Eigenschaften einer Silika-Bilage im Zusammenhang mit Anwendungen von 2D Materialien. Die Bilage besitzt kristalline und amorphe Regionen, welche beide atomar glatt sind. Die kristalline Region besitzt eine hexagonale Gitterstruktur mit gleichmäßiger Porengröße, während die amorphe Region einer komplexeren Beschreibung bedarf. In einer Studie von Baublöcken zeigen wir, dass mittelreichweitige Struktureinheiten in Korrelation mit einem Parameter für die Bindungswinkelfrustration auftreten. Das resultierende Netzwerk verschiedener Nanoporen stellt eine größenselektive Membran dar, wie wir in einer Adsorptionsstudie zeigen. Pd- und Au-Atome durchdringen den Silikafilm selektiv, abhängig von der Größe der zur Verfügung stehenden Nanoporen.

Der ultradünne Film hält der Einwirkung verschiedener Lösungsmittel stand und die Beständigkeit der Struktur in Wasser wird analysiert. Diese Studien deuten die außergewöhnliche Stabilität dieser Nanostruktur an.

Wir entwickeln eine polymerbasierte mechanische Exfoliationsmethode, um den Film von seinem Wachstumssubstrat zu entfernen, und zeigen, dass der Film als intakte Einheit vom Substrat abgelöst wird. Wir präsentieren anschließend den Transfer des Silikafilms auf ein TEM-Gitter, wo er schraubenartig gewundene Formen annimmt. Weiterhin wurde der Film auf ein Pt(111)-Substrat transferiert. In diesem Fall wird unter Erhalt der Struktur ein Transfer in der Größenordnung von Millimetern erreicht.

Contents

1. Introduction

1.1 Two-dimensional materials

Two-dimensional materials are an object of ongoing fascination for scientists and have been dubbed ‘A revolution of nanoscale dimensions’.[1] The first member of this material class to gain wider popularity was a single layer of carbon atoms, known today as graphene. Since the 1960ies, many researchers have studied this two-dimensional carbon crystal.[2–4] But only in the last decade has nearly every stable element and compound been scrutinized as to how thin it may be produced and what surprising properties result from this reduced dimensionality.

In the context of this work, a two-dimensional (2D) material will be defined as the thinnest possible stable arrangement in 2D of a chemical compound. In the case of some elements like carbon, silicon or hafnium, this requirement may be fulfilled by a single atomic layer.[5] Some binary chemical compounds can be produced as a single atomic layer as well, such as hexagonal boron nitride monolayers. Other compounds exhibit a different structure; two-dimensional MoS_2 is one such example. It consists of a layer of molybdenum sandwiched between two sulfur layers. Although the resulting sheet is approximately 6.5 Å thick, it is the thinnest stable sheet with a stoichiometry MoS_2 known at this point.[6] More broadly defined, a 2D material extends significantly further in x- and y-directions that it does in the z-direction, such as few-layer graphenes.[5]

Two-dimensional materials are generally fascinating, because they often exhibit surprising properties that cannot be extrapolated from any bulk analogues. Many of these properties are assigned to the unique structure of 2D materials. Few-layer nanosheets possess an extraordinary surface-to-bulk ratio and single-layer materials consist of only surfaces. Electronic states change dramatically at this length scale; an example is black phosphorus, which has a significantly larger band gap in its two-dimensional form than as

a bulk material,[7] and processes like heat or charge transfer are confined to a planar geometry.[8] Unfortunately, material properties regarding the stability also change when going from 3D to 2D. Two-dimensional materials derived from highly stable bulk counterparts are often found to corrode, decompose or are otherwise unstable in ambient conditions.[9] Therefore, the library of 2D materials available for technological applications is limited at this point.

The most widely known 2D material is graphene, which has been studied intensely under the name of graphite monolayers on metal surfaces since the 1960ies.[10–13] It experienced a renaissance when it was shown that the monolayers exfoliated from the bulk material are visible to the naked eye when supported on an oxidized Si wafer.[3] This enabled identification of single layers with an optical microscope, thereby rapidly increasing processing speed and enabling further studies of the material properties. Graphene consists of a single layer of carbon atoms, arranged in a hexagonal geometry, as indicated in Figure 1.1a. Its charge carrier mobility is ten times higher than that of silicon, making graphene an incredibly effective conductor, and its breaking strength exceeds that of steel more than a factor of 100.[14, 15] Many other extraordinary and exotic properties of this material have been documented as well.[16]

Although the excitement sorrounding graphene was acknowledged with the Nobel Prize for Physics in 2010, commercial products utilizing its properties remain few and far between. The rate limiting step for market-ready applications of 2D materials is usually the large scale material production with sufficient quality.[16] It is expected that flexible electrodes utilizing the high conductivity of graphene will be commercialized earlier than other graphene related applications, as they do not rely on large scale, structurally perfect graphene sheets. Prototypes of transparent, flexible electrodes have been manufactured using graphene based conductive inks.[17] In order to use graphene as electrode material, it needs to be combined with an insulating material in a device. Two such substrates that are often employed are silicon dioxide (also called silica) or hexagonal boron nitride.

In the form of a bulk material, silica is known to be chemically inert, thermally stable and extremely cheap due to its abundance in the earth's crust. It has found use as building material, for manufacturing objects of everyday life, but also specialized applications like semiconductor industries and catalysis, where it is used as support material. Amorphous silicon dioxide films of a few nm thickness with defect densities of 10^{-5} per surface atom are routinely obtained by oxidizing the surface of a silicon wafer.[18] Due to this well controlled thermal oxidation process, silicon dioxide has been used for decades as preferred insulator in the silicon-based semiconductor industry. Placing a graphene sheet on amorphous SiO_2 produced by thermal oxidation, however, leads to significant losses in graphene electron mobility.[19] This effect has been assigned to the silicon dioxide influence, either due to its rough morphology, scattering at defect sites or interaction with surface charges of the substrate.[20–23]

Many of these problems can be circumvented by placing graphene on thin layers of hexagonal boron nitride (h-BN).[19] This material can be produced in few-layer or monolayer sheets which are extremely flat. Nitrogen and boron atoms arrange in hexagonal symmetry, as illustrated in Figure 1.1b. The h-BN structure is isostructural to graphene, and is occasionally called "white graphene".[24] h-BN possesses a band gap of ~6 eV, is thermally stable and chemically inert.[11, 25–27] The graphene and hexagonal boron nitride lattices have an extremely small mismatch of 1.7%, and graphene has been shown to conform to atomically flat h-BN substrates without wrinkles or rippling effects.[19] Graphene layers are often supported on 10-50 nm thick h-BN sheets.[24, 28] Exfoliation of h-BN into thinner sheets is challenging, since h-BN has stronger interlayer adhesion forces than graphite. Therefore, single-layer h-BN sheets larger than a few µm are rare.[16, 24]

Graphene layers supported on h-BN have shown high free carrier mobilities, with smaller losses than on rough silica substrates.[19, 20, 28] When graphene (almost) completely retains its inherent properties on an ideal support material like h-BN, it is sometimes called freestanding or quasi-freestanding.[28, 29]

More frequently, the term freestanding is used for freely suspended 2D materials that are only in contact with their support over a fraction of their surface area.[30, 31]

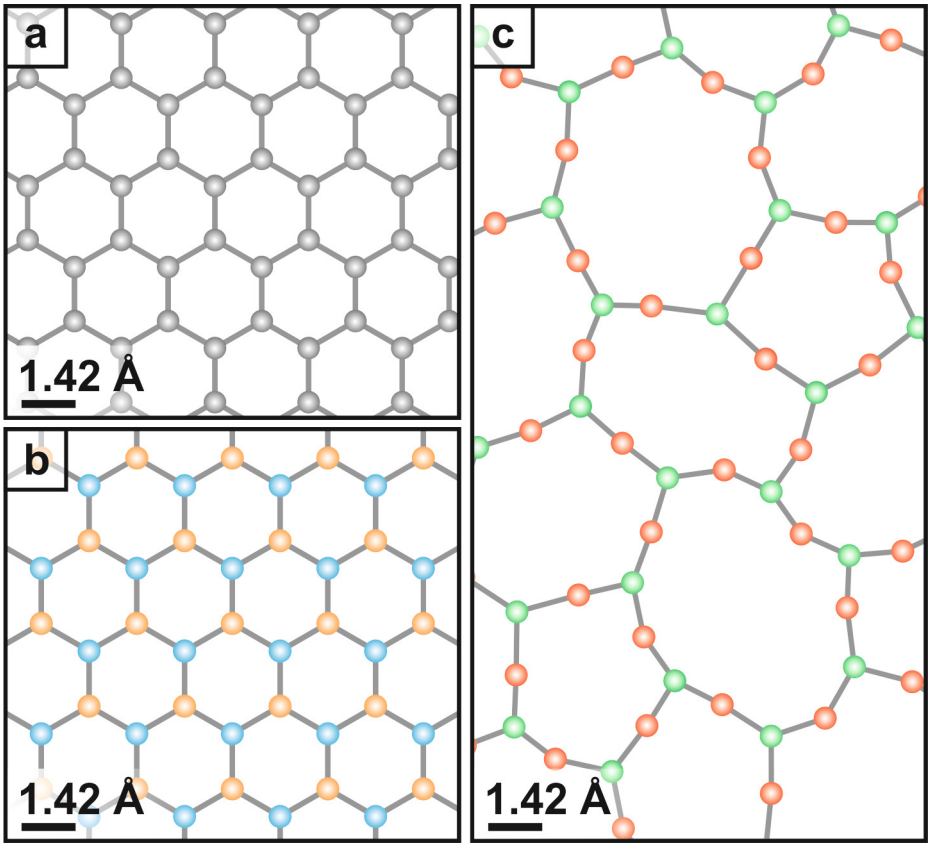

Figure 1.1: a) Model of graphene sheet with gray markers for carbon atoms. b) Model of hexagonal boron nitride sheet with blue markers for boron atoms and orange markers for nitrogen atoms. c) Model of silicon dioxide bilayer (top layer visible) with green markers for silicon atoms and red markers for oxygen atoms.

Combinations of two or more 2D sheets with a precisely defined thickness are called van der Waals solids.[9] Atomically flat sheets of any composition are expected to adhere together readily based on van der Waals forces. Entire stacks of 2D sheets may be created to exploit the extraordinary properties of these materials. Van der Waals solids of conducting graphene and insulating h-BN are challenging to produce, due to the aforementioned difficulties with producing single layer h-BN. Furthermore, the relative orientation of isostructural graphene and h-BN needs to be precisely controlled, as it influences the properties of the resulting van der Waals solid.[32]

Recently, an ultrathin, self-saturated silicon dioxide sheet has been prepared on a Ru(0001) support.[33, 34] It consists of exactly two layers of SiO_4-tetrahedra. One such tetrahedral building block is shown in Figure 1.2a. The tetrahedra are corner connected via oxygen bridges, thereby forming extended networks. Each tetrahedron is connected via three oxygen bridges in plane, while the fourth oxygen bridge extends in z-direction (out of plane), forming a bridge towards the second layer, as illustrated in a side view in Figure 1.2b. The two layers are self-saturated, without any dangling bonds and without covalent bonds to the growth substrate. Density functional theory (DFT) and infrared (IR) spectroscopy indicate that the top and bottom layer have the same arrangement of building blocks.[35] Hence, the building units can arrange in amorphous or hexagonal structures (Figure 1.2c and Figure 1.2d, respectively), while remaining atomically flat.

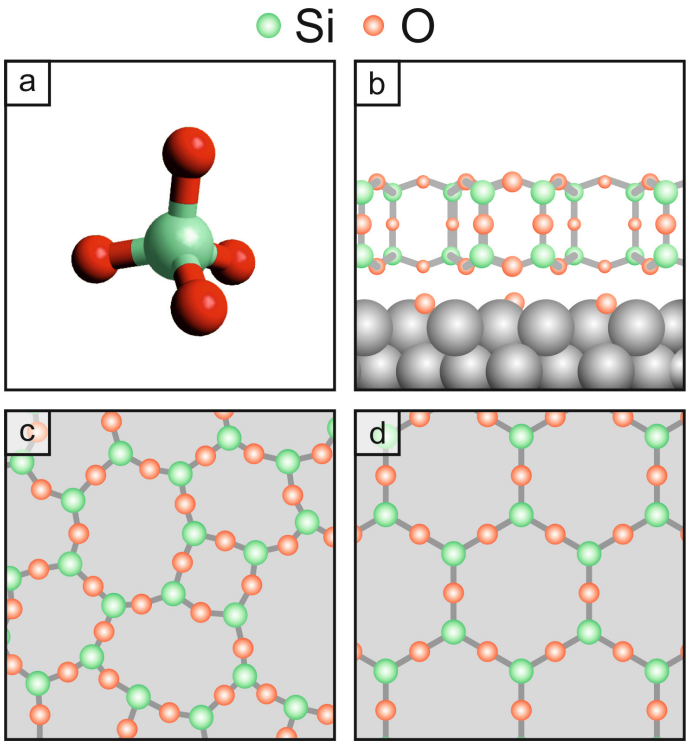

Figure 1.2: Models of silica bilayer on ruthenium substrate. a) Tetrahedral SiO_4 building block. b) Side view of bilayer. c) Top view of amorphous bilayer. d) Top view of crystalline bilayer.

This silica bilayer is the thinnest possible two-dimensional material with the stoichiometry SiO_2, as a monolayer film has been shown to have a stoichiom-

etry of $SiO_{2.5}$.[36] More recently, this system was predicted to have a band gap of 7 eV,[37] which surpasses the band gap of h-BN[6] and may be a viable alternative for an insulating, atomically flat graphene support.

If this bilayer silica sheet can be isolated from its growth substrate, it can also be utilized in other 2D materials applications such as van der Waals solids. Figure 1.1c shows a model of the amorphous silica bilayer, for direct comparison with the graphene and h-BN structures. It is apparent that the building blocks of all these 2D materials form larger, chain-like features, or rings. These 'nanopores' have been used for intercalating gold atoms through the 2D sheet in the case of graphene.[38] Intercalation can be utilized to change the properties of the 2D material or to deliver precursors for additional 2D sheets that are prepared in situ. In comparison to the graphene and h-BN nanopores in Figure 1.1a and b, the nanopores formed by the silica sheet (Figure 1.1c) are roughly twice as large in diameter. This indicates that for intercalation experiments on 2D silica, a larger variety of small species may be accommodated.

Incorporation of one or several SiO_2 bilayers into van der Waals solids would provide well defined dielectric spacer layers, which crucially influence the properties of the entire stack. One such example is a layer-cake structure of graphene and insulating layers. Precise control over the interplanar spacing is predicted to facilitate high-temperature superconducting properties.[9] In the case of the amorphous bilayer structure, handling of the 2D layers is simplified, as the properties are expected to be isotropic.

In order to make the silica bilayer accessible for 2D applications, it either needs to be grown in situ on the substrate required by the application or transferred post-growth to such a substrate. At this point, successful growth of a bilayer silica film has been reported for only a few substrates, most of them being metal single crystals.[34, 39–42] It is therefore assumed that the highest quality films can be grown using these substrates and well-documented growth procedures. Hence, a transfer is currently the most promising option for exploring silica bilayers in the context of 2D materials appli-

cations in basic research. Several requirements must be met in order to regard a transfer procedure as successful. An as-grown silica film needs to be sufficiently structurally characterized. Then, a method needs to be developed to remove the sheet, ideally structurally intact, from the growth substrate. Subsequently, the exfoliated silica bilayer needs to be deposited on a new substrate and its structure needs to be characterized. Preservation of structure throughout this process would be the condition to employ a silica bilayer film in 2D materials applications.

1.2 Aims of this project

An ultrathin, self-saturated SiO_2 film has been prepared on different substrates.[33, 34, 39–42] This silica film is potentially relevant for 2D materials applications, especially as an ultrathin dielectric material. Such insulating materials are rare in the current library of two-dimensional materials, but urgently needed for constructing nanoelectronic devices. Generally, the properties of a 2D material may vary greatly from its bulk counterpart. Therefore, it will be one goal of this project, to investigate the properties of an ultrathin silica bilayer, especially in conjunction with application as 2D material.

To this end, the amorphous pore structure of the silica bilayer film needs to be characterized in detail, to enable exploiting its porous properties. The porosity of the silica film may be utilized for creating a molecular or atomic sieve, where a mixture of species is separated by selective penetration through a silica bilayer membrane. The adsorption properties of the nanosheet can also be employed for intercalating reactive species to the film-support interface, in order to create van der Waals heterostructures.

In order to employ silica thin films in diverse technical applications, it must be stable enough to exist in ambient conditions and allow transfer to substrates on which it may not be grown directly.

Finally, suitable methods need to be developed to exfoliate the bilayer sheet from the growth substrate, with appropriate characterization of the exfoliated films and the plain substrate. Demonstrating a successful transfer of a silica bilayer to a foreign substrate is the final goal of this project. Ideally, a large-scale film should be transferred with minimal structural damage.

1.3 Thesis structure

In Chapter 2, background information is provided on experimental techniques used in this work. Additionally, the general preparation procedure for silica bilayer films on Ru(0001) is described, along with relevant previous studies carried out to characterize this system.

Chapter 3 investigates properties of silica bilayers that are relevant to future applications as a 2D material. Section 3.1 presents structure studies that help to define and understand the amorphous domain of the silica film in terms of ring sizes and larger building units. Section 3.2 contains results on adsorption experiments that highlight the structure-selective adsorption behavior of the silica bilayer. This property could be exploited for membrane-type applications in the case of a freestanding silica bilayer. In Section 3.3, different exposure studies are conducted to benchmark the structural stability of the bilayer and the robustness against different solvent treatments.

The robustness of our system is the precondition for the transfer of this bilayer film, which is presented in Chapter 4. Section 4.1 discusses methods to exfoliate and transfer 2D materials and presents a procedure that allows complete removal of the 2D silica film. In Section 4.2, the transfer of a silica bilayer to a TEM grid is presented. Section 4.3 shows results on the transfer of a silica film to a new metal substrate, proving that the structure is retained.

2. Background

In this chapter, technical information is provided as context for the results presented in the later chapters. Section 2.1 addresses the different experimental techniques employed in this work. Section 2.2 provides details on the preparation procedure used to obtain silica bilayer films. It also provides a brief overview on the insights published previously on silica bilayer films on ruthenium supports.

2.1 Experimental techniques

This section provides a brief overview of the experimental techniques used in this work. General remarks on working in ultrahigh vacuum are relevant for most of these techniques. They include different microscopy techniques, ranging from atomic resolution to mm-scale imaging. The elemental composition for each sample was probed using Auger electron spectroscopy (AES). Low energy electron diffraction (LEED) was used to investigate the surface structure. The working principle for each technique is outlined. Additionally, technical limitations and the consequences for applicability are discussed.

2.1.1 Ultrahigh vacuum studies

The systems investigated in this work are dominated by surface properties. Highly clean ruthenium crystal surfaces are crucial for the successful preparation of a silica bilayer. The subsequent characterization of the bilayer requires the surface to remain free from adsorbates. Furthermore, many of the surface science techniques used in this work (STM, AES, LEED, TEM) are based on the assumption that electrons travel to and from the sample and to the detector unperturbed. Hence, these studies were carried out in an ultrahigh vacuum (UHV) chamber.

The setup used in this study achieves pressures below 10^{-9} mbar through constant evacuation using turbomolecular pumps and ion getter pumps. The microscopy unit is furthermore surrounded by a liquid helium cryostat, which lowers the pressure by several orders of magnitude.[43] The sample can be positioned in front of different preparation components and detection units with the help of external manipulators.

Preparation of ultraclean surfaces utilizes ion bombardment ("sputtering") and electron impact heating. Heating in the presence of oxygen is used to remove carbon contaminations from the surface. Ultrathin silica films are prepared using physical vapor deposition (PVD). Details on the preparation procedure are provided in Section 2.2. The components of the UHV chamber used in this project have been described in great detail elsewhere.[44]

2.1.2 Scanning tunneling microscopy

Scanning probe microscopy (SPM) techniques represent one way of circumventing the diffraction limit observed in classical optical microscopy. Scanning tunneling microscopy (STM) relies on the quantum mechanical phenomenon of electron tunneling. The term *tunneling* is used to describe the process of an electron moving across an energy barrier that is larger than the potential energy of the electron.

When a surface is scanned with a sharp tip at very close distances with an applied bias voltage, a tunneling current can be measured. For image acquisition, a sharp tip probes the sample surface laterally in a scanning motion and a feedback mechanism monitors the tunneling current between tip and sample. The axis perpendicular to the sample is typically denoted as z, while scanning directions are denoted as x and y. The xy-plane is also called the imaging plane. The general measurement principle is shown schematically in Figure 2.1a. Possible imaging modes include recording the tunneling current versus the lateral position in a constant height scan or continuously correcting the tip position in order to hold a constant current setpoint. The corresponding

characteristic line profiles recorded in the I_T-channel and the z-channel are shown in Figure 2.1b and Figure 2.1c.

The tunneling current I_T depends strongly on the tip-sample distance s,

$$I_T \approx \frac{V}{s} e^{-A\sqrt{\bar{\Phi}}s} \tag{1}$$

with V denoting the sample bias, A = 1.025 $(\text{eV})^{-1/2}\text{Å}^{-1}$ and $\bar{\Phi}$ the average barrier height.[45] Due to this dependence, tunneling current measurements are very sensitive to changes in the tip-sample distance. For example, sample corrugations of 1 Å and respective changes in the tip-sample distance can lead to a current increase of one order of magnitude.

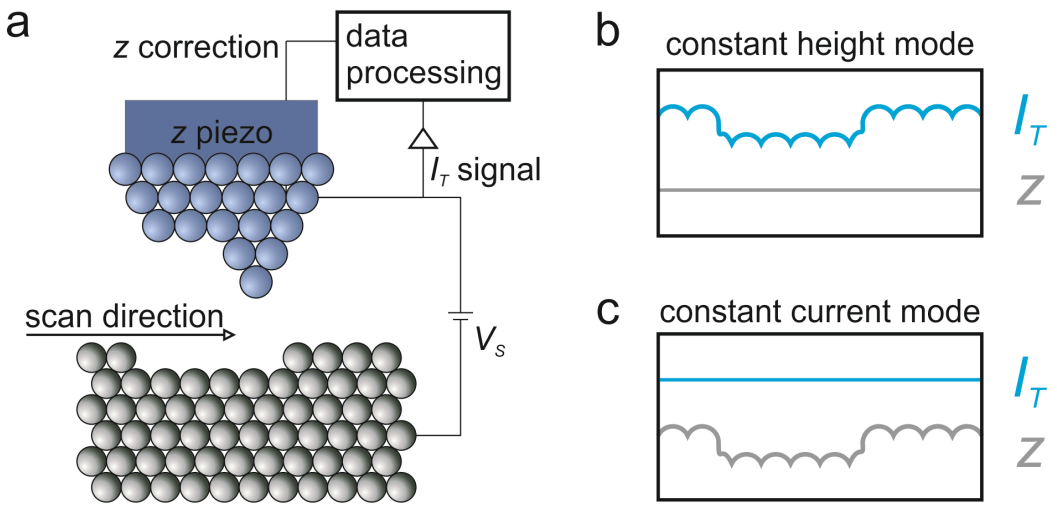

Figure 2.1: General schematic for STM imaging. a) Sketch of the main elements in an STM: a bias (V_S) is applied between sample (gray) and scanning tip with z piezo (blue). The tunneling current (I_T) and height (z) signal form a feedback loop, controlled by a data processing unit. The scan direction (x or y) along the surface is indicated with an arrow. b) Corresponding line profiles in constant height mode. I_T shows the local electronic variations while z is held constant. c) Corresponding line profiles in constant current mode. I_T is held constant by varying the tip height. The z signal corresponds to the local height profile and the local electronic structure.

As seen from Equation (1), the tunneling current is influenced by several parameters, including the local electronic properties of the surface. Therefore, STM images are mainly useful for studying the overall surface morphology.

The local height information cannot be directly extracted, when contrast formation is governed by changes in the local electronic structure.

Obtaining images in STM can take several minutes per image. During this time, the surface under investigation needs to be stable and stay free of contaminants. Therefore, the STM setup used in the work presented here is housed in a UHV chamber system. The microscope unit is surrounded by a bath cryostat which is filled with liquid helium. The ultralow temperature environment not only improves the vacuum, but also stabilizes the tip and reduces noise and drift effects.

The resolution limit of the STM is mainly determined by the exact movement of the piezo actuators and the sharpness of the probing tip. For the work presented here, a full metal tip (made from Pt/Ir wire) was used that can be conditioned in situ by voltage pulses to achieve sub-nanometer resolution.

Conducting samples are required for STM studies. Many oxides, however, are semiconductors or insulators. If they are prepared as ultrathin films, these can still be studied with STM.[46, 47] The limiting thickness for imaging depends on the band gap of the material. Stable imaging of thicker insulating films often requires high bias voltages, which can cause film damage. At a thickness of two monolayers, the silica bilayer allows unhampered investigation by STM.

2.1.3 Atomic force microscopy in liquids

Atomic force microscopy (AFM) is used in addition to STM for characterizing surfaces at high spatial resolution. It is complementary to STM, as it yields height information and is not limited to conducting samples. The working principle for AFM at the first glance is similar to the STM depicted in Figure 2.1. A sharp tip probes the surface in a scanning movement, while a feedback loop controls the tip-sample distance. In the case of AFM, the force between tip and sample is the monitored quantity. Interaction forces can be any com-

bination of Coulomb forces, mechanical contact forces, and van der Waals forces. If the electrostatic force is compensated by applying a bias voltage, direct height information can be extracted from the imaged sample morphology. However, the feedback mechanism required for AFM is different from STM, due to the different distance dependence of both kinds of interaction. Figure 2.2 shows typical curves that are recorded for the tunneling current (Figure 2.2a) and the force interaction (Figure 2.2b) while the height z of the tip is varied. Both curves were measured in a UHV environment. The tunneling current exhibits monotonic behavior, increasing steadily as the tip moves closer to the surface. The force interaction, plotted in terms of frequency shift Δf, is non-monotonic, revealing two distinct regimes, one of attractive and one of repulsive interaction. The feedback mechanism regulating towards a certain setpoint value needs to correctly determine whether the measured interaction lies on the repulsive or attractive branch of the interaction curve. This added complexity requires more advanced electrical feedback for AFM, which was realized experimentally only several years after the invention of STM. It can also lead to AFM measurements taking significantly longer, although considerable progress has recently been made to accommodate imaging of dynamic systems.[48]

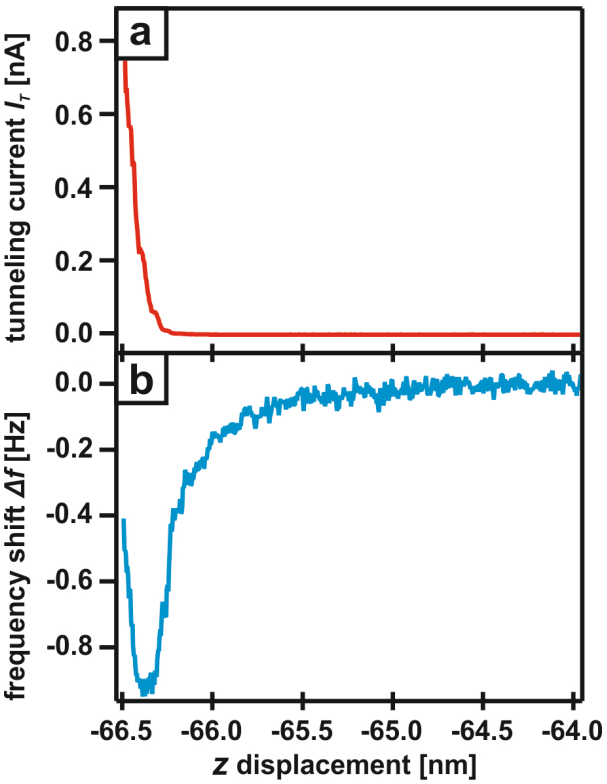

Figure 2.2: Example measurements of tip-sample interaction vs. tip height z. a) Tunneling current curve, showing monotonic behavior. b) Frequency shift curve, showing the non-monotonic force interaction. Adapted from [139].

Another difficulty in conventional AFM measurements is called jump-to-contact. This happens when the probe tip is exposed to strong attractive interaction and “crashes” into the sample surface, damaging both tip and surface

in the process. This problem can be overcome with employing a so-called noncontact measuring mode. In this mode, the sensor is excited into a resonant vibration mode while scanning the surface. Local interaction forces influence the resonance frequency, analogous to an oscillating spring which is affected by adding a weight to it. It is assumed that this kind of interaction can be sensed already when tip and sample are in close vicinity, without touching. Hence this technique is called noncontact atomic force microscopy (nc-AFM).

The AFM measurements presented in this work were carried out in a liquid environment cell, using the Cypher™ AFM from Asylum Research. This instrument enables AFM imaging while sample and AFM tip are immersed in a small volume of aqueous solution. The measurement cell can be kept static or inlets and outlets can be utilized to exchange the solution over the course of time. This environmental cell is suitable for realistically modeling different material application conditions or surroundings in biological systems.

A liquid environment affects AFM measurements in several ways. The surrounding medium damps the oscillating probe considerably, effectively leading to higher noise levels. The images presented in this work were recorded at room temperature, therefore significantly stronger thermal drift is expected compared to imaging at 5 K with the STM. Both of these challenges necessitate fast image acquisition.

Through interaction with the aqueous environment, solvation layers can form on surface and tip. The exact structure of these layers is not fully understood, which complicates interpretation of imaging contrasts. In the past, elaborate 3D topology measurements have been undertaken to shed light on this topic. The resulting solvation structure maps can provide insights on contrast formation and electronic surface termination.[49]

In the case of ionic surfaces or tips, electrostatic forces can exacerbate imaging. Often, this difficulty can be mitigated by using salt solutions, which need to be chosen with the appropriate concentration and valence.

2.1.4 Electron microscopy

For some studies reported in Chapter 4, electron microscopy techniques have been utilized. A brief overview on electron-matter interaction will be followed by details on transmission electron microscopy (TEM), electron energy loss spectroscopy (EELS) and environmental scanning electron microscopy (ESEM).

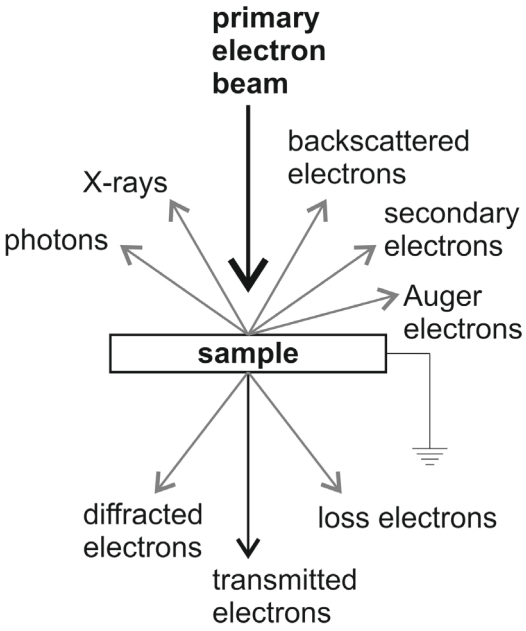

Figure 2.3: Different interaction pathways of electrons and solid samples. Redrawn from [50].

All of these techniques rely on the interaction of an electron beam with a solid sample, which can manifest itself in a manner of ways, as shown in Figure 2.3. If the sample is very thin, a portion of the primary electron beam can pass through the sample without any loss of energy. These transmitted electrons are detected to obtain images in the most common imaging mode in TEM, called bright-field mode. In this mode, contrast is created by the partial absorption and diffraction of electrons by the sample. The image will appear bright where very little or no matter obstructs the electrons and darker, where thicker parts of the sample are in the path of the electron beam. Therefore, in order to obtain sufficient image contrasts, the sample thickness must be on the order of the mean free path of the probing electrons, which typically have an energy of 100 – 200 keV.[50] Sample thicknesses of less than 100 nm are usually achieved by cutting, milling or grinding samples.[51] Alternatively, ultrathin 2D materials can be obtained through exfoliation techniques, which are discussed in Section 4.1. Ultrathin samples are usually supported on fine metal grids in order to perform TEM.

Electrons that undergo diffraction are detected at a different angle than the primary electrons. In the mode of dark-field imaging, only a fraction of the diffracted electrons are selected for detection. The resulting image contrast shows those sample regions that cause the selected diffraction mode, while all other sample regions remain dark. Hence, dark-field imaging can be utilized to collect crystallographic information on the sample.

Generally in TEM, a sample area is imaged by illuminating it at once by an array of parallel electron beams. Scanning transmission electron microscopy (STEM) imaging is performed by focusing the primary beam on a small sample region and scanning the beam across the sample surface. This technique allows high resolution and simultaneous analysis of different signals, such as bright-field imaging, dark-field imaging and electron energy loss spectroscopy (EELS).

EELS measurements can conveniently be incorporated in TEM-setups. They allow studying the composition of the sample by detecting so-called loss electrons with a different energy E

$$E = E_0 - h\nu \tag{2}$$

than the primary energy E_0. The energy difference $h\nu$ can be assigned to electronic or vibronic excitations that were caused by the impinging electron beam. Chemical compounds present in the sample can be identified by comparing characteristic loss spectra with a reference database.

Another electron microscopy technique used in this work is scanning electron microscopy (SEM), where the electron beam is focused to one point and scanned across the sample surface to obtain an image. In SEM however, the secondary electrons (resulting from ionization through the primary beam) and the backscattered electrons are detected. Due to their low energy, the secondary electrons have a limited mean free path. Therefore, secondary electrons that reach the detector provide surface-sensitive information. Secondary electron contrast results mainly from sample topography. Backscattering is more

effective for heavy elements; therefore backscattered electrons can be used to determine the distribution of such elements in the sample.

SEM can be carried out on bulk samples, but has high requirements for sample conductivity, as surface charging from the impinging electron beam obstructs imaging contrast. Environmental scanning electron microscopy (ESEM) presents an elegant solution to this constraint, by providing a reactive gas as a partial pressure in the vacuum chamber during the imaging process. Hereby, the secondary electron signal is amplified through cascading reactions with the residual gas, while the positive ions are drawn to the sample, which prevents charging. By choosing the gas mixture appropriately, sample surfaces can be investigated under reactive conditions, which is crucial for heterogeneous catalysis as well as material science.

Bright-field imaging, dark-field imaging and EELS measurements were performed using a commercial JEOL ARM200F that is equipped with a cold field emission gun. The acceleration voltage V_A of the electrons was 200 kV. Additionally, a GIF Quantum® filter provides the option to detect secondary electrons for imaging.

ESEM imaging was carried out with an FEI™ Quanta 200 system, on a custom built heating stage. The custom designed gas-feeding system allows imaging under controlled atmospheres of up to 20 mbar.[52, 53]

2.1.5 Auger electron spectroscopy

Auger electron spectroscopy (AES) is used as an element sensitive technique to assess the presence of certain species on our samples.

The basic principle of AES is shown in Figure 2.4a. The Auger effect by definition is a three-electron process. In the beginning, an impact from a high energy electron (kV range, step 1 in Figure 2.4a) removes a core-electron (2). The core hole thus created is filled with an electron from a higher energetic

level (3). The excess energy is transferred (4) to a third electron, which is then emitted from the atom (5). The kinetic energy of this Auger electron is detected in AES. The emission of an X-ray photon (6) is an alternative pathway to release the excess energy.[50]

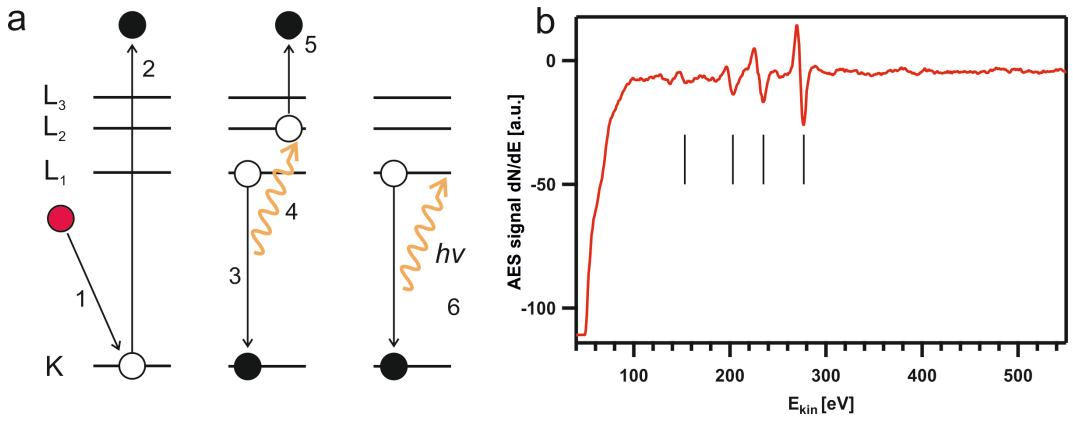

Figure 2.4: Auger electron spectroscopy. a) Elementary steps of the Auger process. An incoming high-energy electron (1) removes a core-electron (2). The core-hole is filled by an electron from a higher orbital (3), which transfers excess energy to another electron (4), which leaves the atom as Auger electron (5). Alternatively, the excess energy is emitted as an X-ray photon (6). b) Typical AES spectrum for a clean Ru(0001) crystal. Minima at 153 eV, 203 eV, 235 eV and 277 eV are characteristic element features.

The kinetic energy of the Auger electron E_{kin} is detected in Auger electron spectroscopy. This value is directly connected with the orbitals involved in the process:

$$E_{kin} = E_K - E_{L_1} - E_{L_2} \tag{3}$$

with E_K, E_{L1} and E_{L2} denoting the energies of participating orbitals. Smaller shifts in the measured energies are contributed by the work function of the detector, final state effects and matrix effects. The primary energy needs to be sufficiently large for the initial removal of the core electron, but does not directly influence the measured energies. Conducting samples are required to prevent charging effects, which especially perturb electrons with low energies (<100 eV).[54]

At the detector, elastically scattered electrons (at the primary electron energy), electrons that have transferred energy in excitation processes (loss electrons and plasmon losses) and secondary electrons contribute to a large background signal. In front of this background, the peaks corresponding to Auger electrons appear relatively small. It is therefore customary to plot the energy-derivative of the detected intensity against the electron energy. The peak positions of Auger transitions are better discernible in this way. Such a spectrum for a clean Ru(0001) crystal is shown in Figure 2.4b. As a general convention, the peak position is reported as minimum value of each transition feature, as indicated with black dashes in Figure 2.4b.

AES is a surface sensitive technique, as the characteristic kinetic energies can only be detected when the Auger electrons do not undergo inelastic scattering. Thus, in the energy range of 50 eV to 500 eV that is typical for the Auger electrons discussed in this work, mostly electrons from the top 1 nm layer of the sample will reach the detector.

The spatial resolution of AES measurements may be estimated by determining the size of the probing beam. This parameter depends on the primary beam energy and the beam current.[55] For typical beam energies of 3 kV and beam currents of 10 µA or more, we estimate our electron beam to have a minimum diameter of 10 µm.[55]

Beam damage during AES measurements can be an issue, especially for delicate samples like reactive organic molecules. However, beam damage of the silica bilayer on ruthenium due to AES has not been observed in this project.

2.1.6 Low energy electron diffraction

Low energy electron diffraction (LEED) provides information on regular structural features on the sample surface. Therefore, it is most useful for investigation of surfaces with crystalline order, but also the short range order

that is observed in amorphous covalent systems, can be characterized with LEED.

A schematic of the working principle for LEED is shown in Figure 2.5a. The technique relies on an electron beam (1) with moderate energy. Our four-grid optics ErLeed by SPECS™ is capable of accelerating electrons up to 3000 eV. For the LEED patterns presented in this work, the energy was adjusted from 60 eV to 140 eV. The DeBroglie wavelengths of such electrons are on the order of 1 Å, which matches the length scale of interatomic distances in solids. Electrons with this energy range have a mean free path of only a few monolayers. This means that elastically scattered electrons which are detected, will originate with a significantly higher probability from the sample surface than from the bulk.

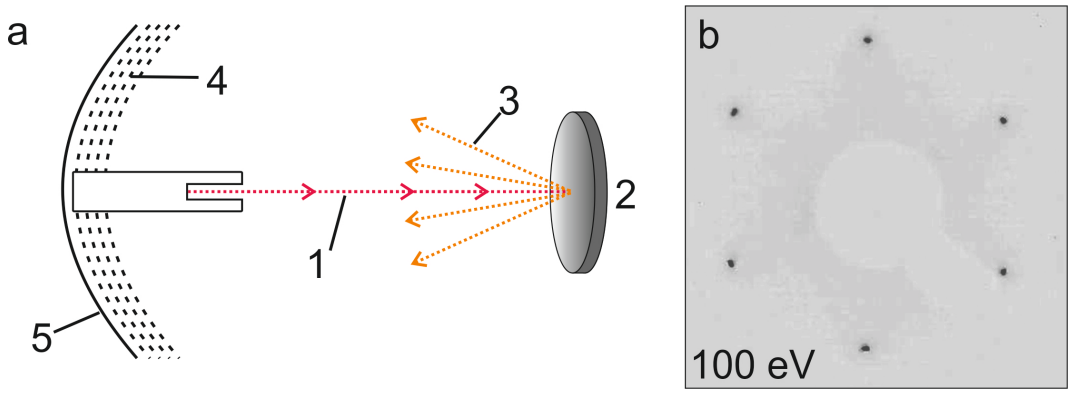

Figure 2.5: a) Schematic of LEED working principle. An electron beam (1) is accelerated towards the sample (2). The diffracted electrons (3) pass a grid analyzer (4) and produce a LEED pattern on a fluorescent screen (5). b) Typical LEED pattern of clean Ru(0001) at an electron energy of 100 eV (contrast invertet).

The focused beam probes a relatively large area on the sample (2), typically on the order of 100 µm. These probe electrons undergo mostly elastic scattering interactions with the surface atoms. The diffracted electrons (3) pass the hemispherical grid analyzer (4) where contributions from inelastic scattering are cut off. The probe electrons produce a diffraction pattern on a fluorescent screen (5).

The low energy electrons are diffracted on each point of the sample surface, depending on the local electrostatic potential. Waves emanating from the surface undergo constructive or destructive interference. The maximal enhancement is described in the Laue equations, using a reciprocal representation.

$$\begin{aligned} \overrightarrow{a_1}\,\Delta\vec{k} &= h\,\lambda \\ \overrightarrow{a_2}\Delta\vec{k} &= k\,\lambda \end{aligned} \tag{4}$$

where $\overrightarrow{a_1}$ and $\overrightarrow{a_2}$ denote the lattice vectors, h and k the lattice indices, λ the wavelength, and the scattering vector $\Delta\vec{k} = \vec{k} - \overrightarrow{k'}$ is determined by the incoming wave vector $\vec{k}$ and the scattered wave vector $\overrightarrow{k'}$. The condition for constructive interference is

$$\frac{\Delta\vec{k}}{\lambda} = h\overrightarrow{a_1^*} + k\overrightarrow{a_2^*} = \vec{\boldsymbol{g}} \tag{5}$$

with $\overrightarrow{a_1^*}$ and $\overrightarrow{a_2^*}$ as the primitive vectors of the reciprocal lattice vector $\vec{\boldsymbol{g}}$. Hence, the scattering vector needs to coincide with the reciprocal lattice vector (rescaled by the wavelength) in order for constructive interference to occur. From this relationship of the scattering vector and the reciprocal lattice, it follows that the pattern of diffraction spots (points of maximum positive interference) is a reciprocal representation of the sample crystal structure. While the electron beam approximately has a diameter of 100 µm, the length for coherent scattering is usually smaller, typically 10-20 nm. Hence, longer-range correlations are not captured in LEED.

Diffraction spots for clean, highly ordered surfaces typically are sharp and intense. Figure 2.5b shows a LEED pattern of a clean Ru(0001) crystal surface. The sharply defined diffraction pattern exhibits a hexagonal symmetry, which is characteristic for this crystal facet. The intensity of the diffraction spots is limited by the surface cleanliness and absence of adsorbates, therefore, LEED is typically carried out in UHV environments. Conductive sam-

ples are another requirement for LEED studies, as surface charging interferes with the experiment.

2.2 Preparation of a two-dimensional silica bilayer

The preparation procedure of a two-dimensional (2D) silica bilayer was reported previously[33, 34, 56] and a detailed growth study was presented by Lichtenstein in 2012.[57] The preparation steps will be reviewed in brief and the characteristics of bilayer films mainly used in this study will be emphasized. All temperatures given in this section were determined using a type K (chromel – alumel) thermocouple. For all preparation steps, a pyrometer may be used as well.

A clean Ru(0001) single crystal surface is prepared by a sputtering/annealing treatment. Initial annealing to 1273 K in an atmosphere of 2×10^{-6} mbar O_2 mainly serves to remove carbon contamination. Repeated cycles of annealing in UHV to 1500 K and argon ion bombardment yield an atomically clean surface. An annealing step must conclude the cleaning procedure. The cleanliness of the surface should be ascertained using LEED, AES and STM.

At a sample temperature of 1243 K and in an atmosphere of 2×10^{-6} mbar O_2, a layer of oxygen is adsorbed on the Ru(0001) surface. By slowly cooling the sample to room temperature in oxygen atmosphere, a 3O(2×2)-coverage is achieved.[57] Optionally, the success of this step can be ascertained using LEED, AES and STM.

Keeping the sample at room temperature, pure silicon is deposited on the sample via physical vapor deposition from an Omicron EFM 3T triple-cell e-beam evaporator. When the flux value of the evaporator control unit is kept constant, a homogeneous deposition over time can be assumed. Therefore, the final coverage of the bilayer depends linearly on the deposition time. After depositing the desired amount of silicon (in an oxygen atmosphere of 2×10^{-7}

mbar O_2), the sample is annealed in an oxygen atmosphere of 2×10^{-6} mbar O_2 at 1263±5 K for 20 minutes. Controlling the oxidation temperature in a narrow window is crucial to obtain clean, smooth films. The sample is cooled in oxygen atmosphere. Cooling rates from 7 K/s to 1 K/s have been applied, without an obvious correlation to the resulting characteristics of the silica films.

This preparation procedure results in the formation of a bilayer film structure with a SiO_2 stoichiometry. The overall degree of order can be ascertained with LEED. AES can be used to determine the evenness of coverage of silica over the width of the sample crystal. STM can achieve high resolution on this system, as the bilayer film is atomically flat, following the morphology of the smooth underlying substrate. STM is used to determine the atomic structure and the exact coverage. The following convention is used to denote film coverages: a closed bilayer equals a coverage of 2 monolayers (2 ML). Typically, less than 2 ML equivalents are deposited. The system's tendency to form the chemically saturated bilayer then results in the formation of a bilayer film with holes exposing patches of the first layer or the metal substrate. In order to evaluate the final coverage of each preparation, a sufficient number of STM images showing flat terraces and open patches is evaluated in the data processing software WSxM.[58] The flooding tool of this software allows easy assessment of the relative image area that is covered by open patches, as illustrated in Figure 2.6.

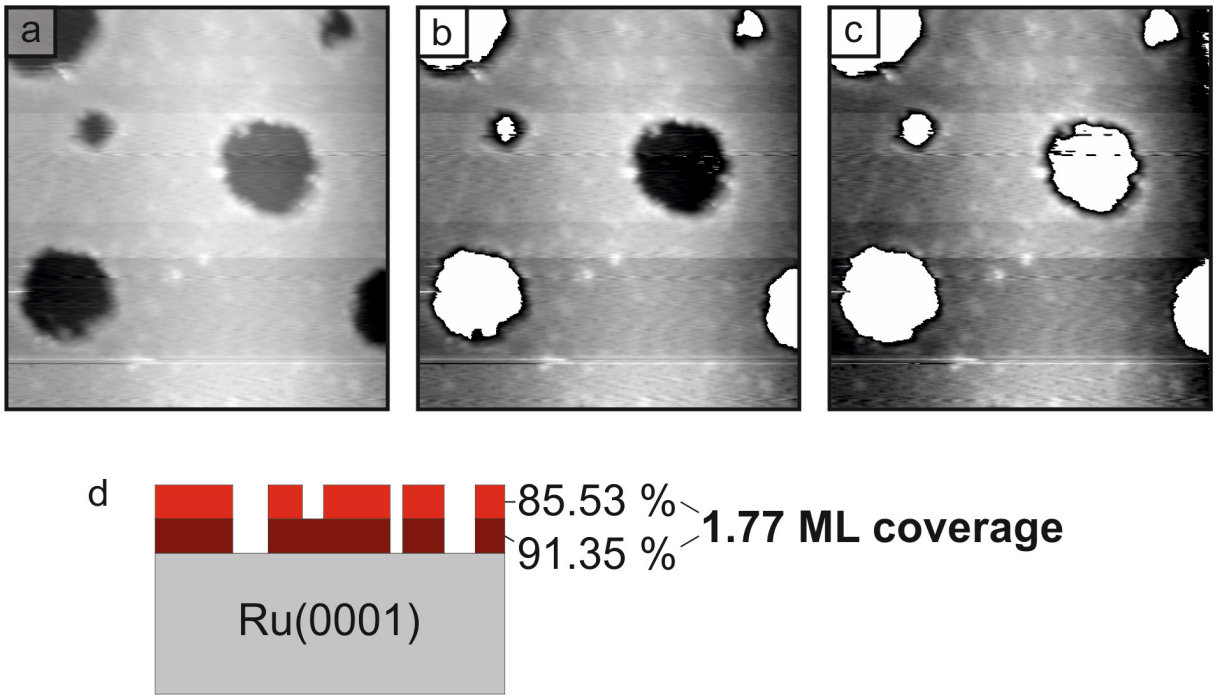

Figure 2.6: Coverage analysis of silica bilayer films. a) STM image of a typical SiO_2 bilayer on Ru(0001), exhibiting holes to the 1st layer and to the substrate. 38 nm × 40 nm, recorded at V_S = 0.5 V, I_T = 50 pA. b) Open patches revealing the substrate (white areas) are quantified. The coverage of the first layer is determined to be 91.35%. c) The coverage of the second layer is determined to be 85.53 %. Below: Schematic shows overall coverage of 1.77 ML.

The preparation procedure described above typically yields silica films exhibiting predominantly amorphous network structures. These can be investigated with high-resolution STM. A detailed analysis of the amorphous network structures can be found in Section 3.1.

The successful preparation of this silica bilayer on Ru(0001) was first reported in 2012[34] and has been studied intensively since then. We will now briefly summarize some key properties that have been previously reported on this system, in order to provide context for the results presented in this work.

The silica bilayer consists of SiO_4 building units with a tetrahedral shape. Two structurally equivalent layers of tetrahedra form a silica bilayer, either exhibiting amorphous morphologies or crystalline order. In the two-dimensional top-view that is obtained in microscopy, the building units ap-

pear as SiO_3 triangular units, as the fourth oxygen bridge connects to the bottom layer. For the crystalline and the amorphous variety, the interatomic distances and angles within each tetrahedron are identical. In the crystalline variety, the building blocks are connected at regular angles to form a hexagonal network with long range order. In the amorphous variety, they exhibit a range of connecting angles, and form a network of differently sized rings, ranging from four- to nine-membered, and very rarely from ten- to twelve-membered. The stability of each ring size, determined by DFT calculations, is in qualitative agreement with the occurrence frequency of the ring sizes.[34]

Atomic resolution images typically show only one atomic species, oxygen or silicon; a selectivity that results from tip termination. Thus, for structure analysis, the positions from the imaged species are used to infer the second species. Simultaneously recorded AFM- and STM-measurements can reveal the positions of both species, thus corroborating the method for atomic position retrieval.[59]

Due to amorphous and crystalline domains coexisting on one sample, it was also possible to study the interface of these two domains with atomic resolution.[60] This coexistence is observed only on a ruthenium substrate, while purely crystalline or purely amorphous structures have been observed on other substrates. The oxygen affinity of the metal has been identified as a parameter that correlates with the structural influence that the metal exerts over the oxide layer.[40]

3. Properties of a two-dimensional silica bilayer

A bilayer of SiO_2 has been prepared on an atomically flat support. A remarkable feature of this system is its well defined thickness. As the film growth self-terminates at two layers, the stoichiometry and layer structure are well-known and reproducible. Additionally, the self-saturated structure forms no covalent bonds with the substrate, but exhibits weak van der Waals interaction with the support. Such a well-defined layer structure with strong in-plane bonds but weak van der Waals-like interaction with an underlying material is perfectly suited for building up stacks of 2D nanosheets, or van der Waals solids.[9] Hence, this silica bilayer may be regarded as a new addition to the class of 2D materials.

The bulk analogue silica glass is widely used as an insulator, due to its large band gap, as well as remarkable thermal, mechanical and chemical properties. Recently, a band gap of 7 eV was predicted for the silica bilayer.[37] This combination of well-defined layer structure and wide band gap make 2D silica a very promising material. Contemplating the silica bilayer in the light of possible 2D material applications, however, underscores the need for a more detailed investigation of certain properties.

In order to apply this system as a new 2D material, we must understand its atomic structure. Due to weak structural influence of the ruthenium support, a silica bilayer on this substrate exhibits coexisting crystalline and amorphous domains. The crystalline domain has been described experimentally and theoretically elsewhere.[33] The amorphous domain has no unit cell that can be used for concise description. An appropriate description of the amorphous bilayer is required for several reasons. On the one hand, it provides a means of distinction between various amorphous structures. This diversity may be observed when amorphous silica bilayers are prepared on different substrates or using different preparation procedures. On the other hand, a proper description of the structure facilitates theoretical modeling, which is the key to predicting material properties and interpreting experimental results. In Section

3.1, we present a building block study of the amorphous silica bilayer. By investigating the arrangement of rings, a medium range structural correlation is revealed.

This improved description of the ring network is the basis for informed utilization thereof. The existence of such rings of varying diameter inspires several types of application for the silica bilayer. Penetration or intercalation of small species in a 2D material is a prime approach for creating van der Waals solids, which are used for building nanodevices.[9] Furthermore, the bilayer may be used as a membrane, acting as an atomic or molecular sieve. We have studied the selective penetration of the bilayer with single metal atoms; the results are presented in Section 3.2.

Ultimately, any technical application of a silica nanosheet very likely will require the bilayer to be placed on substrates other than ruthenium. For establishing a successful transfer procedure of the silica film, the system needs to be sufficiently stable. We ascertain the chemical and structural stability in several experiments in Section 3.3. In Section 3.3.1, we demonstrate that the film prepared in UHV can withstand ambient conditions and treatment with solvents. In Section 3.3.2, we demonstrate that the morphology is retained in a liquid environment.

3.1 Structural properties of a silica bilayer

A full description of the structures in a 2D silica sheet is an essential requirement for its utilization in nanotechnology. With a thorough understanding of the network structure, deliberate intercalation of small species may be carried out, as shown in Section 3.2. Furthermore, evidence suggests that the local network structure influences the local electronic configuration in a silica bilayer.[61]

The tetrahedral building unit and the nearest neighbor distances have been previously evaluated by Lichtenstein et al..[34, 57, 62] These studies of the short-range order showed strong similarities between the crystalline and the amorphous structure with an equivalent rigid small building unit. This corroborates the established understanding that amorphous solids equal their analogue isomeric crystalline compounds in terms of short-range order, as predicted by Zachariasen.[63] Only from the connection of two or more building blocks, are those parameters derived (i.e., the connection angle or the Si-Si distance), which allow distinction of crystalline versus amorphous structures. The medium-range topology of amorphous networks has been much debated, mainly due to a lack of experimental data regarding real space structure. Historically, amorphous solids have been investigated with diffraction techniques, which allow deriving pair correlation functions. However, for investigating geometries in the medium range length scales, correlations of atom pairs are not sufficient, since they inherently contain only two-body properties.[64] Larger building units need to be studied to describe many-particle geometries adequately.

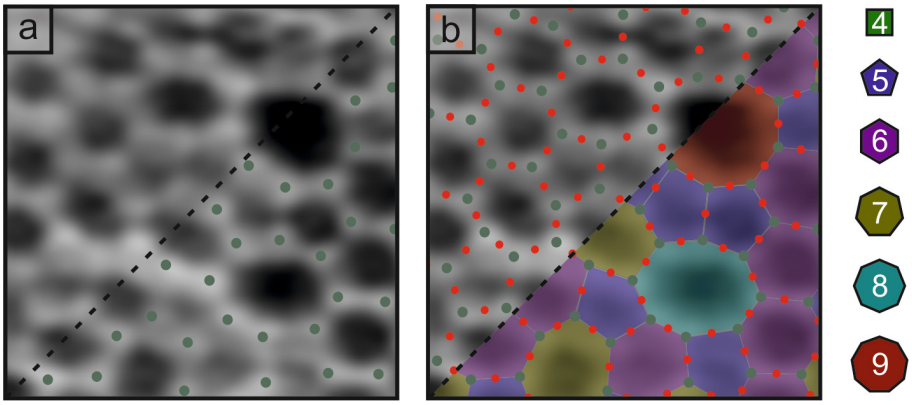

Figure 3.1: STM of a 2D silica sheet, imaged in atomic resolution with a chemical sensitivity to the Si positions. 2.5 nm × 2.5 nm, recorded at V_S = 1 V, I_T = 50 pA. a) The lower half of the image is superimposed with green markers for the Si positions. b) The upper half of the image shows Si positions, and subsequently determined O positions (red markers). The lower half of the image shows different ring sizes color coded according to their size. The color coding is referenced on the right.

Ring structures may be used to investigate this medium range. Due to the network being atomically flat, it was possible to achieve atomic resolution with SPM methods.[33, 34, 57, 65] Real space atomic position data derived from the silica bilayer finally enables the study of geometric properties on different length scales. To this end, rings and ring clusters on a large sheet of the experimentally observed network were analyzed and compared against predicted distributions, assuming random arrangements. The resulting discrepancies of observation and prediction indicate that network formation follows an underlying influence, for which we propose a simple geometric model.

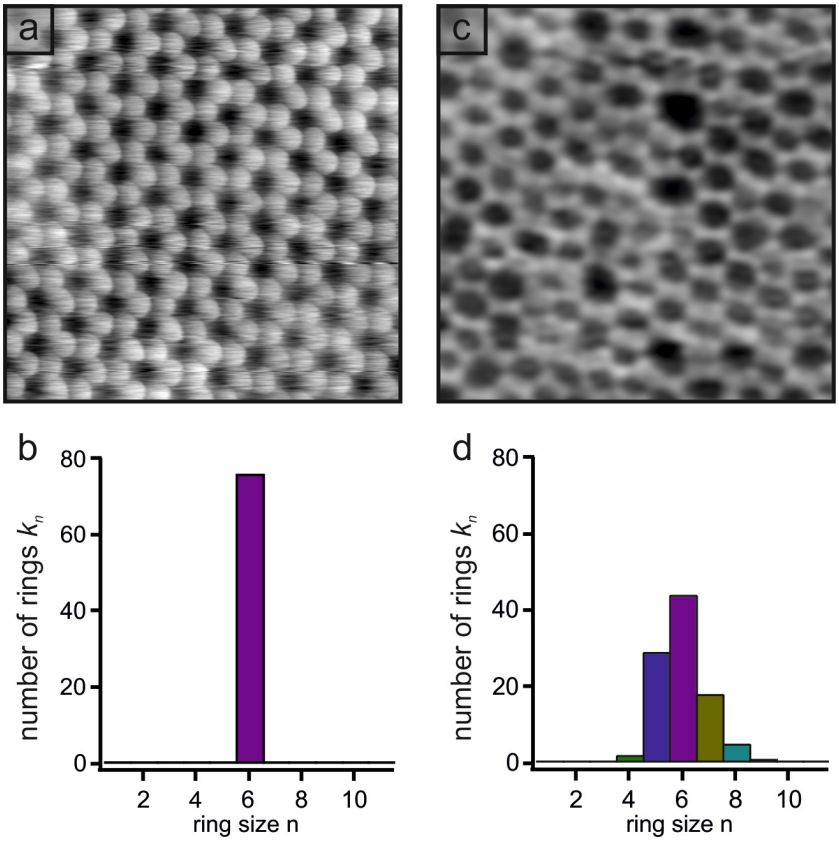

Figure 3.2: Crystalline and amorphous domains of silica bilayer. a) STM image of crystalline silica bilayer. 5 nm × 5 nm, recorded at V_S = 3 V, I_T = 100 pA. b) Corresponding ring size histogram. c) STM image of amorphous silica bilayer. 5 nm × 5 nm, recorded at V_S = 1 V, I_T = 50 pA. d) Corresponding ring size histogram.

A straightforward approach is analyzing the very prominent ring features which stand out in the STM images of this system. The term *ring* means a chain of Si-O-building blocks forming a closed loop. An example is shown in

Figure 3.1. Figure 3.1a shows an atomic resolution STM with a contrast sensitive to Si. In the lower half of the image, Si positions are marked with green circles. The oxygen positions can be inferred from the silicon positions.[57] In Figure 3.1b, the image is superimposed with green markers for Si positions and red markers for O positions. In the lower half of the image, differently sized rings formed by Si vertices are accentuated through different colors, corresponding to their ring size.

The ring network formed by the Si vertices can exhibit either crystalline hexagonal structures or amorphous structures. An example for the crystalline silica bilayer is shown in Figure 3.2a. In this case, six-membered rings are the only ring size observed. The hexagons are arranged in an ordered honeycomb structure with 5.42 Å periodicity that is commensurate with the substrate lattice.[57]

The amorphous network regions consist mainly of rings ranging from four to nine vertices, as shown in Figure 3.2c. They are arranged in a disordered fashion, without any obvious pattern. The corresponding ring size histogram in Figure 3.2d shows the non-Gaussian distribution of rings.

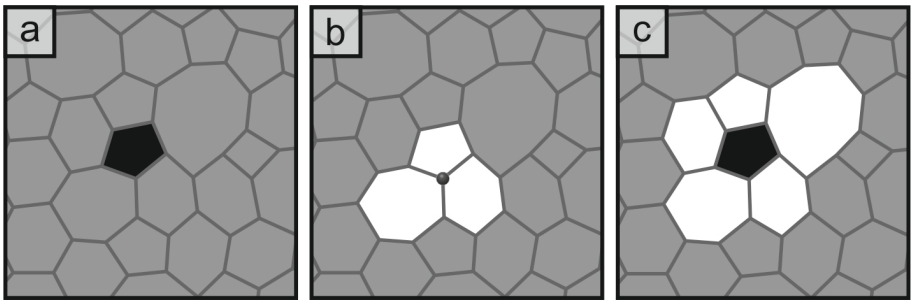

Figure 3.3: Schematic of network building blocks. a) A five-membered ring is marked within the network. b) A triplet consisting of a five-, six- and seven-membered ring sharing a single Si atom is marked within the network. c) A five-membered ring is marked in black and all neighboring rings (i.e., rings that share an edge with the central ring) are marked in white within the network.

In order to shed light on the seemingly random ring network, we analyzed the building blocks of a large STM image, which are schematically shown in Figure 3.3 The investigated building units were single rings (Figure 3.3a), tri-

plets of rings sharing a Si atom (Figure 3.3b), and typical neighborhoods of central rings (Figure 3.3c). The results presented in this section have been published in the Journal of Non-Crystalline Solids.[66]

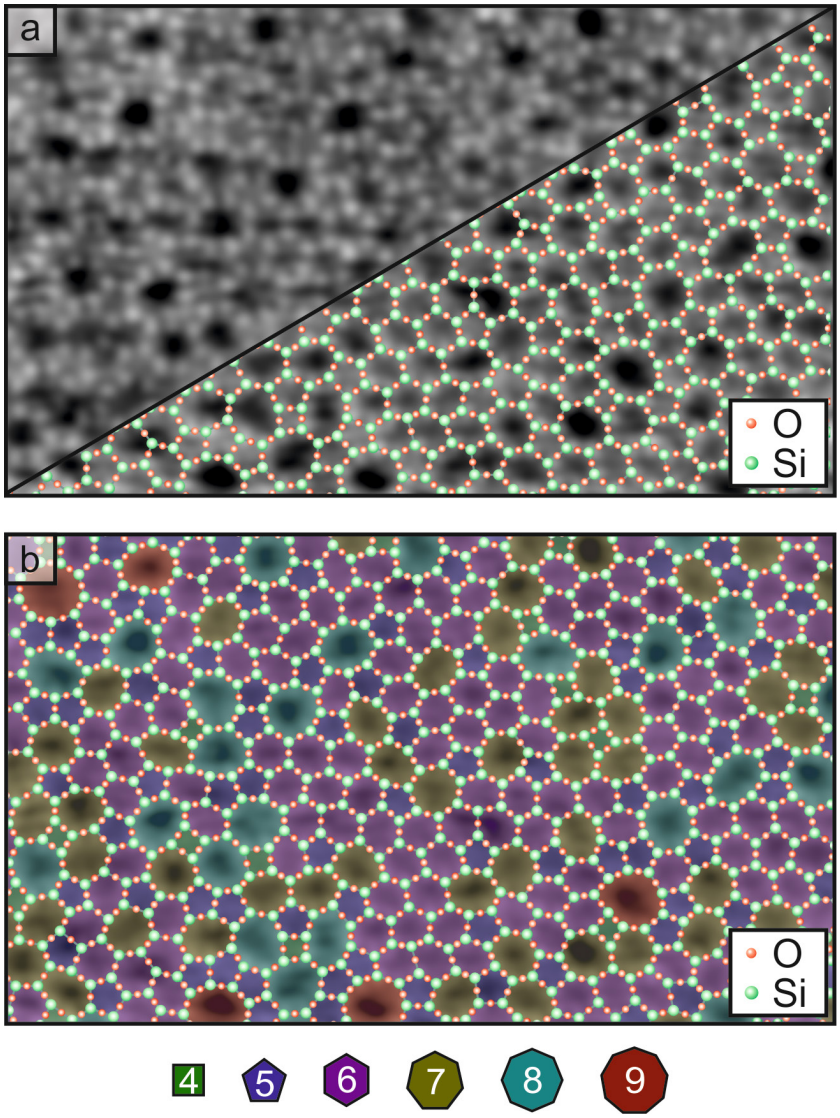

Figure 3.4: Large STM of an amorphous silica bilayer. a) STM 12.2 nm × 6.6 nm, recorded at V_S = 2 V, I_T = 50 pA (image from [62]), partially superimposed with red markers for oxygen positions and green markers for silicon positions. b) Same image entirely superimposed with atomic position markers and ring sizes in different colors, according to color code shown beneath.

The ring network study is based on a large STM image containing 403 rings, providing a statistical basis for analysis. The silica bilayer was prepared using the method described in Section 2.2. The image is shown in Figure 3.4,

showing the positions of Si atoms directly. The positions of O atoms are inferred mathematically. The Si atoms form a network of different sized rings.

The ring statistics have been historically debated strongly, since ring sizes in bulk glass can only be inferred indirectly from data such as Raman spectroscopy[67, 68] or diffusivity measurements.[69–73] Additionally, nuclear magnetic resonance measurements (NMR) can deliver bond angles and Si-Si distances,[74–76] but rings and ring arrangements have not been directly determined experimentally for bulk silica. From the 2D network studied here, we observe ring sizes ranging from four-membered to nine-membered rings. The straightforward way to enter into a building block investigation is to count the different ring sizes. The corresponding ring size histogram for the STM above is shown in Figure 3.5. The distribution of ring sizes is not symmetric with respect to the main species, the six-membered ring. The occurrence probabilities for each ring size correspond well with the relative energies that were previously determined by DFT.[34]

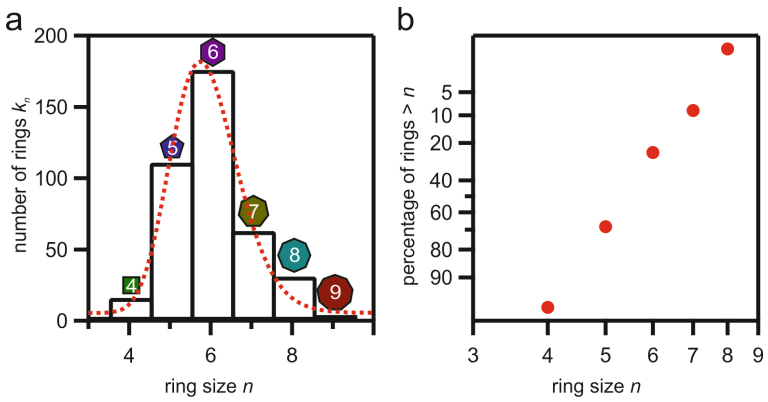

Figure 3.5: Ring size data from STM shown in Figure 3.4. a) Histogram of ring sizes. A lognormal fitting function is plotted as red curve. b) Log-normal probability plot of ring size, indicating that ring sizes follow a log-normal distribution.

A more general treatment of the ring sizes can be obtained using Euler's characteristic, which is a geometrical property predicted by Euler for different geometric shapes. In case of a two-dimensional plane, each divergence from the perfect hexagonal building block induces a curvature. In a honeycomb network, for example, a pentagon induces a convex deformation. The struc-

tural influence of rings smaller than six-membered is balanced by larger rings. An ideally flat, infinitely large sheet therefore has an Euler characteristic of zero. The total curvature of the different sized rings can be determined by summing up the collective deviation from the hexagon, considering k_n rings of ring size n:

$$\sum_{Euler} = \sum(6 - n)k_n = 0 \tag{6}$$

While the ideal, infinite 2D sheet will yield $\sum_{Euler} = 0$, a system that is limited in size will deviate from the ideal value. The silica sheet in this example yields an Euler sum of $\sum_{Euler} = 6$. As the silica bilayer in AFM measurements has shown height fluctuations between atomic positions of less than 0.2 Å,[77] and thus is extremely flat, we assume that this deviation is merely an effect caused by the finite size of the sampled area. In order to verify this assumption, we can regard the relative deviation per ring, which is defined as

$$\sum_{rel} = \frac{\sum_{Euler}}{\sum k_n} \tag{7}$$

with the total number of rings denoted as $\sum k_n$. In the case of the silica network shown in Figure 3.4, $\sum_{\mathrm{rel}} = \frac{6}{403}$ is very low, but this value rapidly increases when smaller network samples are investigated. This consideration verifies the assumption that the deviation from zero in $\sum_{Euler}$ is due to a finite size effect.

We can conclude that the silica bilayer possesses only a small overall deviation from the Euler sum, and therefore the structure is not deformed strongly out of a flat two-dimensional plane.

Moving on to the next larger building unit, we observe that one Si atom is always coordinated in a threefold manner, and therefore always involved in three rings. These ring triplets are the object of our next investigation, in which we strive to determine whether the single rings arrange randomly in triplet clusters. The formation of single rings definitely has to conform to the

energetic limitations of bond angle distortion, but how do three rings form a cluster? In order to shed light on this building unit, we extract the probability distribution of different triplet combinations from the STM shown in Figure 3.4. This observation can be compared with a predicted distribution, which uses the observed probabilities for each single ring size and assumes all ring sizes arrange in an uncorrelated way. Figure 3.6 shows the observed amount of each combination in black bars. The predicted amount is shown in a second, colored bar. The combinations are plotted in ascending order of occurrence in the network.

The random prediction seems to model the general trend of small, medium and large counts for the investigated combinations with only a few exceptions. It is clear however, from comparing the random prediction with the experimental data, that the formation of ring triplets is influenced by an additional factor. Since the prediction of triplets is a purely probabilistic concept, we additionally consider the geometric frustration of rings involved in different combinations.

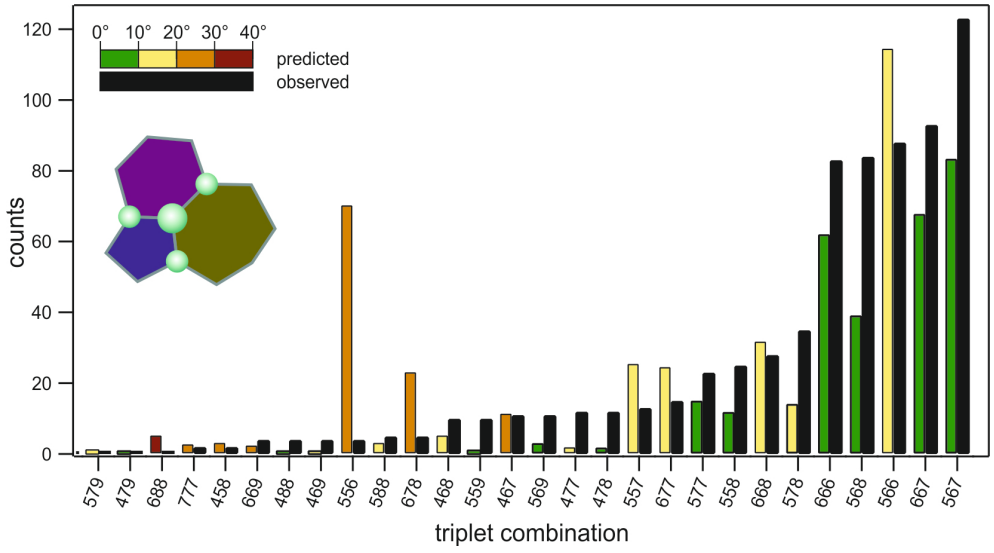

Figure 3.6: Histogram of predicted versus observed triplet distribution. Black bars show the observed amount for each ring combination. Colored bars show the predicted amount for each ring combination, color coded for the estimated angle error. A 567-triplet is shown as an example.

To do this, we consider the tiling of the 2D plane with ideal polyhedra first. An example is shown in Figure 3.7 in gray. Here, a symmetric quadrilateral, hexagon and heptagon form a triplet. In this example, the internal angles do not fully cover 360°. In our experimental silica bilayer, we observe however, that the network is atomically flat, without buckling or gaps, and consistently exhibits threefold coordination, without over- or undercoordination. Therefore, three rings around one Si atom must fill out the plane, their internal angles adding up to 360°. This is achieved through distortion of the rings from their ideal symmetric shape, as shown on the right side of Figure 3.7. For each triplet combination, we determine the difference of the total internal angles of ideal polyhedra and 360°:

$$\Delta_{klm} = |\mathbf{360°} - (\boldsymbol{\alpha} + \boldsymbol{\beta} + \boldsymbol{\gamma})| \qquad (8)$$

with α, β and γ denoting the internal angle of ideal polyhedra k, l and m. Δ_{klm} is called the angle error and a unique value can be assigned to each triplet combination, given the size of the involved polygons. Δ_{klm} is indicated in the schematic shown in Figure 3.7. It gives an approximation for the amount of stress that is accomodated when three rings arrange in a triplet. For the analysis of triplet combinations, we will not regard the sign of the angle error and treat deviations from 0 in both directions the same by considering absolute values. The angle error can take absolute values from 0° (for the combination of three hexagons) to 90° (for the combination of three four-membered rings) in theory. The experimentally observed combinations yield values from 0° to 30° for this network.

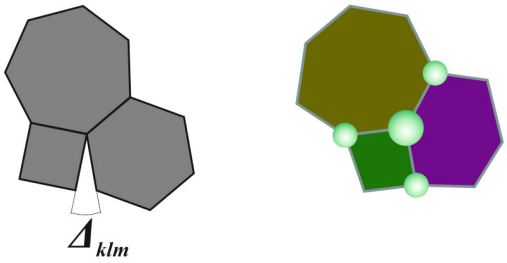

Figure 3.7: Comparison between tiling of ideal quadrilateral, hexagon and heptagon and experimentally observed 467-triplet building block. Δ_{klm} indicates the angle error.

The histogram bars for the predicted count in Figure 3.6 are color coded for the magnitude of their angle error. The uncorrelated prediction in conjunction with the angle error allows placing the differ-

ent triplet combinations into three distinct categories. The category of favorable geometry is characterized by angle errors smaller than 10° (green histogram bars). In this category, the predicted count is exceeded by the observed count for every combination. The category of intermediate geometry is characterized by angle errors between 10° and 20° (yellow histogram bars). Here, prediction versus reality does not follow a common trend. In the third category of unfavorable geometry, angle errors >20° are assigned (orange and red histogram bars). For this category, the counts predicted on the basis of single ring occurrence always exceed the observed counts. This indicates that the angle error can be used to gain some insight into the geometric frustration of a triplet combination.

While the angle error approaches geometric favorability from the point of single ring or bond angle distortion, the aforementioned Euler sum creates an argument based on distortion from the flatness of a 2D sheet. A local value for the Euler sum can be determined from Equation (6) for each triplet. The absolute value of the local Euler sum equals two or lower for all triplet combinations that are observed frequently (10 or more counts). A small value signifies a combination that induces low curvature. The highest value for observed combinations is 4, while the hypothetical maximum would be 9. This observation shows the Euler sum is a simple tool to approximate the flatness or curvature of network building units. Additional theoretical studies should be conducted, however, as they are needed to uncover further factors influencing amorphous networks and to develop a predictive model.

Moving beyond ring triplets, the study of complete ring neighborhoods is also of interest, as this property was historically often referenced to characterize network structures. Beginning with macroscopic structures in nature like the Giant's Causeway,[78] polygon networks have always sparked the interest of scientists. With the invention of microscopy, cell networks of plants and animals became accessible for structural investigations.[79] F. T. Lewis already observed that in cell tissue, few-sided cells are usually next to many-sided cells.[79] D. A. Aboav suggested a fixed relation between a central ring with

size n and the average size of the neighboring rings m_n. S. Chiu provides a useful overview on the development of this law,[80] which is known as the Aboav-Weaire law today:

$$\boldsymbol{m_n = (6 - a) + \frac{(6a + \mu_2)}{n}} \tag{9}$$

The parameter a is a fitting factor, which varies for each system.[81] A universal fit factor of a = 1.2 was determined to be "a general property of naturally occurring nets"[82] by studying soap bubble networks,[83] metallic glasses[82] and chalcogenide glasses.[84] The law also includes the network variance, or second central moment of the ring size distribution, μ_2. This parameter is derived from the ring size distribution $p(n)$.

$$\mu_2 = \sum_n \boldsymbol{(n - 6)^2 p(n)} \tag{10}$$

The smallest possible value for the variance is zero, meaning that the ring network is comprised only of one ring size, such as hexagonal rings. Larger values stand for a wider ring size distribution. Equation (9) can be multiplied with n, yielding a linear expression.

$$\boldsymbol{m_n \cdot n = n(6 - a) + (6a + \mu_2)} \tag{11}$$

This linear dependence can be plotted and analyzed conveniently. The atomic resolution data from Figure 3.4 can be analyzed for the neighborhood of each ring of size n. For this evaluation, complete neighborhoods should be analyzed for each ring. Therefore, only 317 rings were counted as central rings, and rings at the border of the image were considered only as neighbors.

The neighborhood distributions for each central ring size are shown in Figure 3.8. The observed distribution of neighbor ring sizes can be again compared to an uncorrelated neighborhood, which assumes that all single rings can arrange independently of each other. This predicted neighborhood distribution

corresponds to the single ring size distribution, normalized for the cumulative number of neighbors of one central ring size, e.g. 10 four-membered rings have 40 neighboring rings altogether.

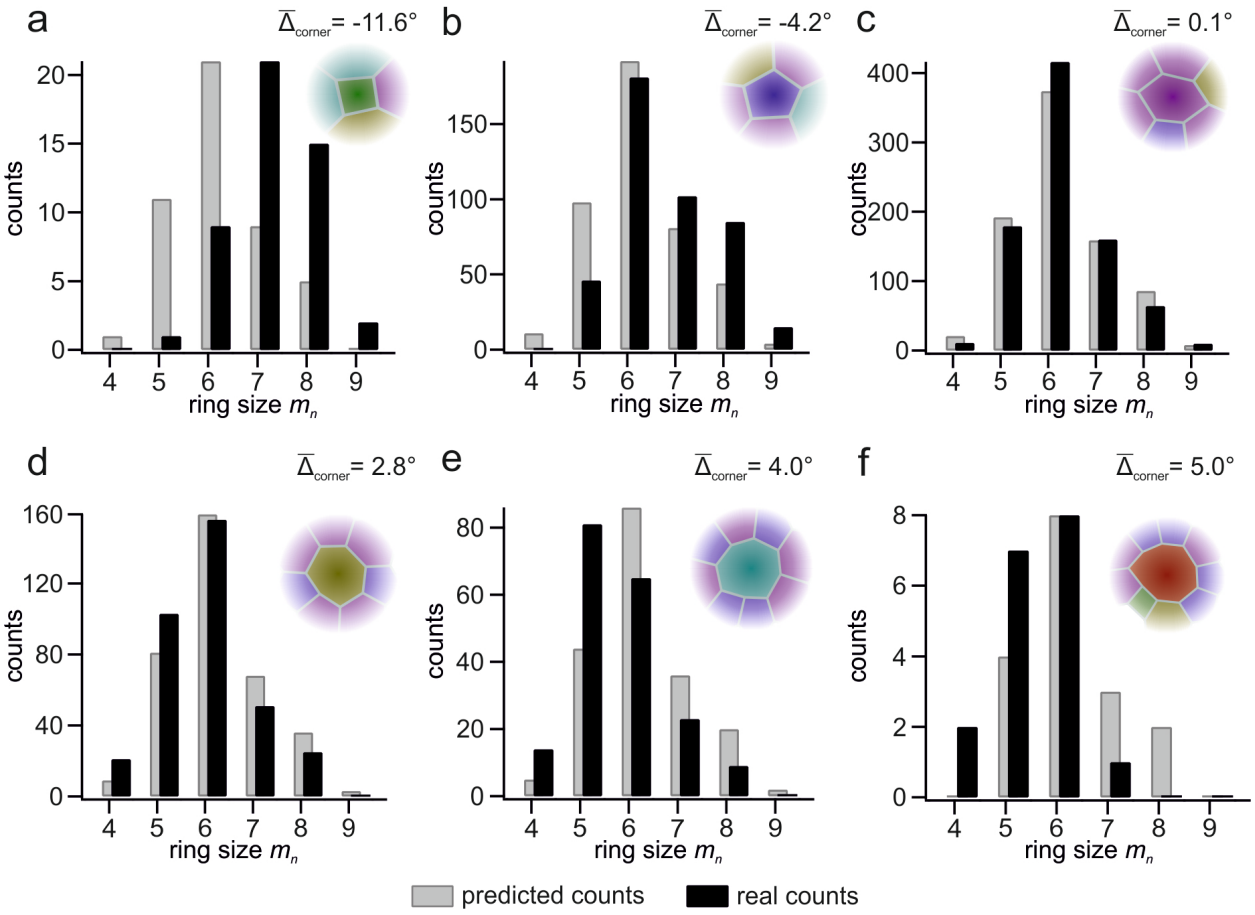

Figure 3.8: Ring neighborhoods of 2D silica. a) Observed ring sizes around central four-membered ring are shown in black bars. A random prediction for the ring size distribution is shown in gray bars. $\overline{\Delta}_{corner}$ indicates the average angle error at each Si atom. Corresponding data are presented in b) for five-membered central rings, in c) for six-membered central rings, in d) for seven-membered central rings, in e) for eight-membered central rings and in f) for nine-membered central rings.

The observed histograms (black bars) in Figure 3.8 match the prediction reasonably well for the six-membered and seven-membered central rings. The neighbor distributions for the small central rings are skewed towards larger ring sizes and vice versa, concurring with F. T. Lewis' observation on cell

networks that "few-sided polygons are predominantly in contact with many-sided and vice versa".[79]

By determining the angle error at each Si atom according to Equation (8) and averaging for all atoms that are part of a certain central ring size, we can state an average angle error $\overline{\Delta}_{corner}$ for each central ring size. This value is indicated above each histogram, including the sign. The evolution of $\overline{\Delta}_{corner}$ from four- to nine-membered central rings indicates that this value expresses whether bond angles are forced to widen or to compress in order to tile the 2D plane in a flat sheet.

From each observed ring neighbor distribution, an average neighbor size m_n can be derived and plotted as $m_n \times n$ versus n in order to test whether the Aboav-Weaire law holds for this covalent continuous network, see Figure 3.9.

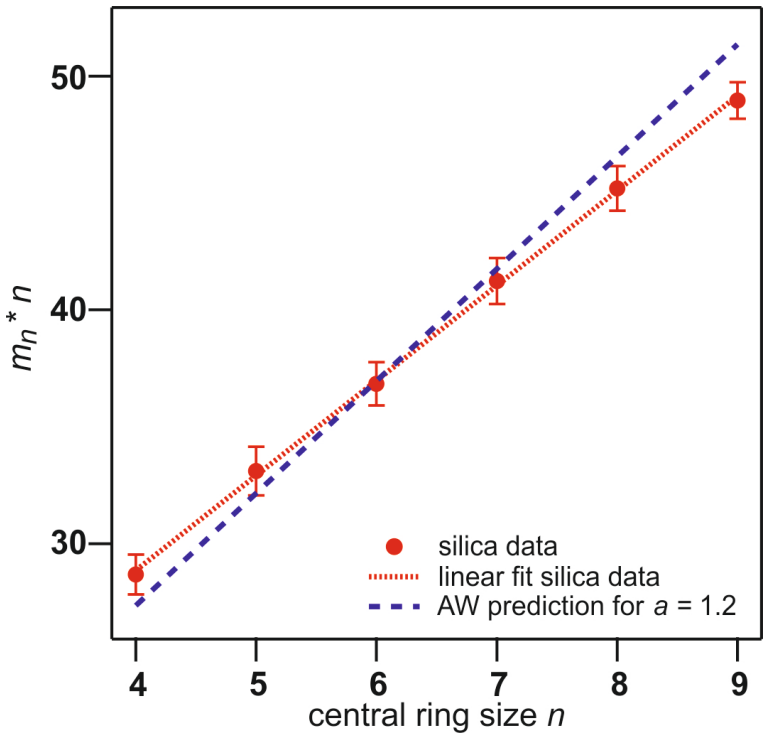

Figure 3.9: Aboav-Weaire law plotted as $m_n * n$ vs. n. Red data points correspond to average neighbor ring size m_n determined from STM. A red line marks the linear fit to the data. A blue curve marks the predicted neighborhood for the "universal value" a = 1.2.

Indeed, the observed average ring neighbors, plotted in Figure 3.9, follow a linear behavior. From the linear fit, we can infer the fit parameters μ_2 = 0.97 ± 0.01 and a = 1.94 ± 0.05, showing good agreement with the variance determined directly from the ring statistic, μ_2 = 0.99. However, the derived value for a diverges considerably from a = 1.2 which was proposed as universal fitting parameter. It must therefore be assumed that the fitting parameter a depends on the system under investigation and is not a universal constant for all systems.

In summary, we have analyzed the ring network of an extended sheet of amorphous silica, based on atomic resolution data from STM on a SiO_2 bilayer. A good understanding of the occurrence probability of ring sizes as well as commonly occurring arrangements of rings is crucial for purposeful usage of a bilayer film in membrane-type applications.

In order to explore this possibility further, we studied size-selective penetration over the silica bilayer. The results of this investigation are presented in Section 3.2.

3.2 A silica bilayer acting as an atomic sieve

An intriguing consequence of the amorphous network structure that was discussed in Section 3.1 is that the network of differently sized rings can act as atomic or molecular sieve. Intercalation of 2D materials is utilized for a number of reasons. Size-selective penetration has recently been studied for graphene membranes, which may be utilized for highly efficient reverse osmosis water desalination.[85, 86] Similarly, zeolite membranes with carefully chosen pore sizes have been employed to separate ions in vanadium flow batteries.[87] Transporting small species to the interface between a chemical vapor deposited (CVD) 2D material and the growth substrate can be used for tuning the material properties. Intercalation of Au atoms to the interface of graphene on

Ni(111) was shown to reduce the coupling of graphene to the substrate.[38] The electronic and magnetic properties of graphene that was decoupled in such a way, have been shown to be similar to freestanding graphene.[88] Furthermore, the possibility to deposit reactive species which pass through the 2D membrane, opens a path for building up 2D heterostructures, also called van der Waals solids. Such stacks of 2D materials have been proposed for many different applications, for example nanosized electronics.[1] While isolated nanosheets may be stacked manually to explore the potential for any novel combination of 2D materials, this approach can hardly be scaled up to produce devices on an industrial scale. Intercalation through epitaxially grown graphene sheets, has been used to prepare thin oxide films underneath the graphene, thus demonstrating possible routes for building van der Waals solids.[89–91]

The ring network of the silica bilayer allows penetration of small species, but different ring sizes will allow different particle sizes to migrate through them. In Section 3.1, we analyzed the ring statistics and worked towards understanding the building blocks of the network in greater detail. This knowledge can be employed for utilizing the silica network as an atomic sieve. We have investigated this property of the 2D silica film by conducting metal adsorption experiments. Parts of the results presented in this section have been published in the Journal of Physical Chemistry C.[92]

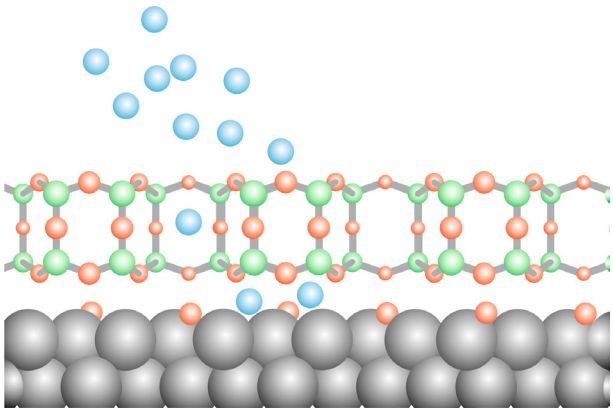

Figure 3.10: Schematic of metal atom deposition over a silica bilayer on ruthenium.

We have conducted single metal atom adsorption experiments on a mixed domain silica bilayer and identified a size-selective adsorption behavior. As shown in Figure 3.2, crystalline regions consist of only six-membered rings, providing uniformly sized pores for adsorption of small species. In the case of amorphous regions, different pore diameters represent different penetration possibilities.

A pristine silica bilayer was prepared according to the procedure described in Section 2.2. Characterization with our low-temperature STM revealed a system with roughly equal fractions of crystalline and amorphous bilayer regions. The measurement in UHV ensures that the surface stays stable and free of adsorbates for long time spans. Two custom-built micro-evaporators are situated in close vicinity to the microscopy unit.[93] Each consists of a filament, coated with palladium or gold, respectively. By applying a low current to the filament, evaporation of the coating metal is induced. This method enables us to deposit very small amounts of metal atoms directly onto the silica bilayer in a low-temperature environment. Figure 3.10 shows a schematic of the metal deposition procedure. Possible adsorption sites for adsorbates are on top of the oxide, within the oxide bilayer or between the oxide and the substrate. The sample temperature of 5 K, however, prevents the adsorbate species from diffusing across the surface over long distances and forming larger aggregates.

Figure 3.11 presents typical examples of the silica bilayer after metal adsorption experiments. Figure 3.11a shows an STM image with a crystalline region covering the top half of the image, and an amorphous region in the bottom half of the image. Adsorbed single Pd atoms change the local electron density and appear brighter in the STM image. Pd adsorption is observed on the crystalline region as well as on the amorphous region of the bilayer. For enhanced visibility, Figure 3.11c shows the same image with the morphological domains and adsorbates color coded. Figure 3.11b shows an STM image of another silica bilayer preparation, exhibiting comparable amounts of crystalline and amorphous domains. Adsorbed gold atoms again show as brighter regions in

the image. It is clearly visible that adsorption of this species is not homogeneous over the entire film. The positions of the bright features are either within, or on the edge of the amorphous region. Figure 3.11d shows the same image with the film structure and the adsorbate positions marked in different colors. Note that the features of low brightness in Figure 3.11b are assigned to native SiO_2/Ru(0001) species, which are observed before evaporative loading experiments.

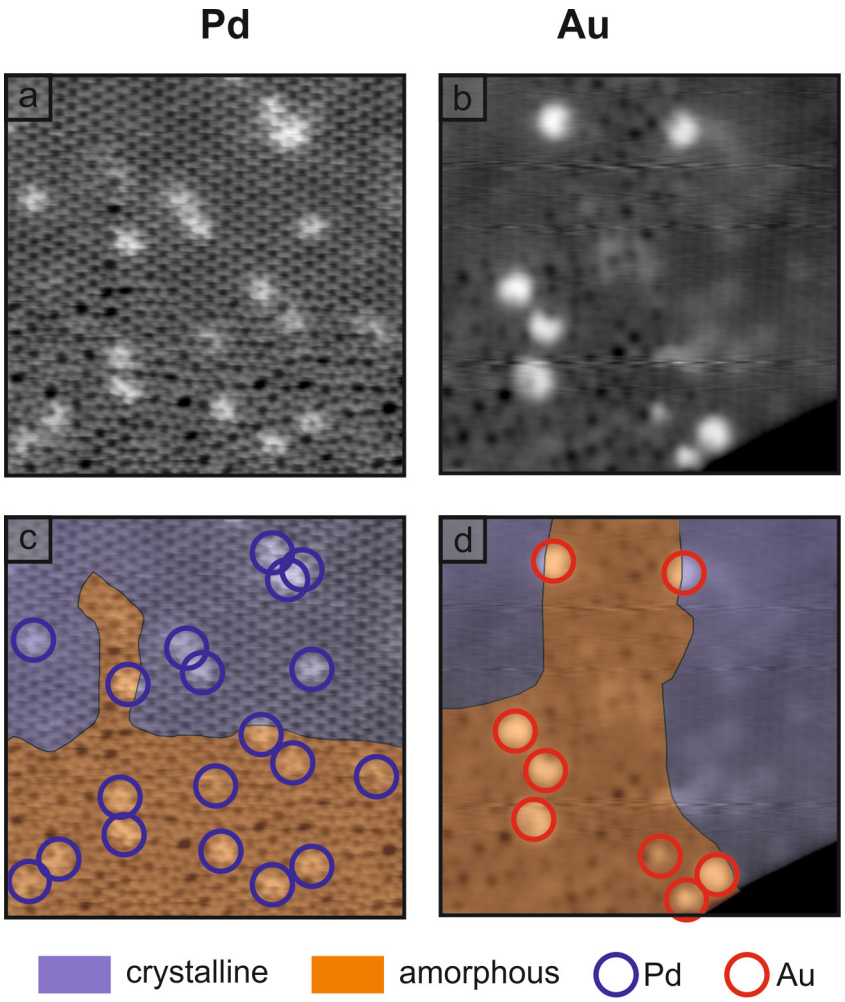

Figure 3.11: STM images of metal atom deposition over a mixed-domain silica bilayer. a) STM showing crystalline silica in the top portion, amorphous silica in the bottom. Adsorbed Pd atoms appear as bright protrusions. b) STM showing crystalline silica on the right portion and top left corner and amorphous silica in the remainder of the image. Adsorbed Au atoms appear as bright regions. c,d) Same STM images, with crystalline domains, amorphous domains, Pd adsorbate positions and Au adsorbate positions color coded. All images: V_S = 2 V, I_T = 100 pA, 15 nm × 15 nm.

The observed differences in adsorption tendency of Pd versus Au are expressed quantitatively in Figure 3.12. The amount of adsorbates was analyzed with respect to the preferred adsorption region. Different preparations with different deposition times were included in this analysis. Therefore, coverage per deposition time is plotted. It is obvious that Pd adsorbs equally well on crystalline regions as on amorphous regions. On the other hand, Au atoms are exclusively observed in the amorphous phase.

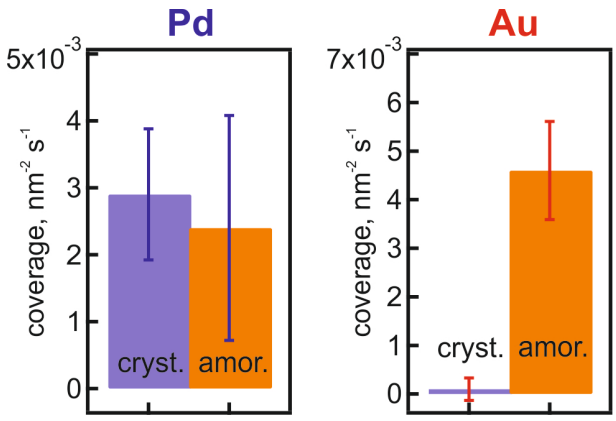

Figure 3.12: Adsorption statistics for Pd and Au deposition on silica. Analysis includes STM areas of 3700 nm² and 3000 nm², respectively. The coverage per nm² is normalized for different deposition times.

A natural conclusion is to connect these findings with the different ring sizes which are available as adsorption sites in the different domains of the silica bilayer. The amorphous phase is made up of rings ranging from four- to nine-membered. The crystalline phase, on the other hand, consists solely of six-membered rings, with the exception of the domain boundaries. These line defects within the hexagonal phase can be employed to shed more light on the size-selective adsorption behavior of this 2D material.

Figure 3.13a shows such a domain boundary in the right half of the image. The boundary is comprised of eight-membered rings alternating with pairs of five-membered rings, forming a straight line. This is the most frequently observed type of domain boundary of the silica bilayer on Ru(0001). Figure 3.13b shows an STM image of a hexagonal silica region after deposition of Au atoms. Bright features are observed along the domain boundary. This find-

ing shows that Au atoms are able to adsorb at the boundary, presumably at the eight-membered rings of the boundary, while they do not adsorb on the crystalline patch, where only six-membered rings are present. This is another strong piece of evidence that the adsorption mechanism is influenced by the ring size.

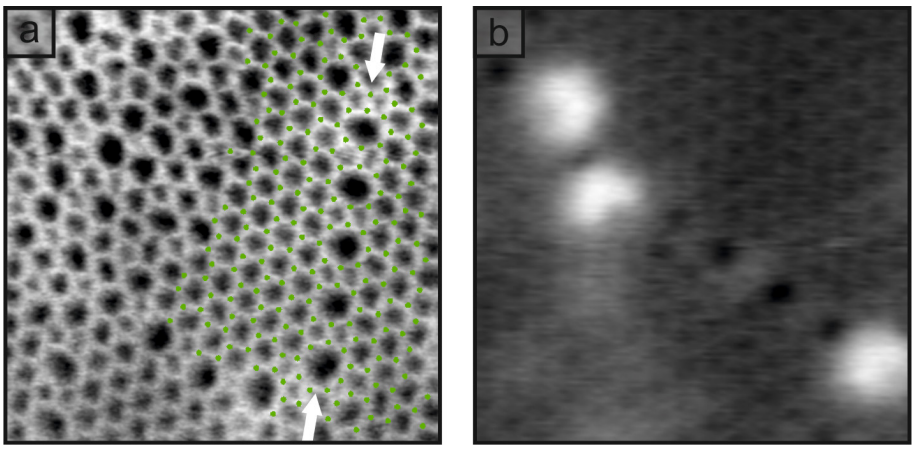

Figure 3.13: STM study of adsorption on domain boundaries. a) STM image of a pristine preparation of mixed domain silica, exhibiting a crystalline phase on the right half of the image. Si positions are marked with green circles. A domain boundary within the hexagonal phase consisting of eight- and five-membered rings is indicated with white arrows. Image parameters: V_S = 0.5 V, I_T = 100 pA, 7 nm × 7 nm. b) STM image of a hexagonal region of the silica bilayer, including a domain boundary of equivalent structure. Au single atoms were deposited on this sample. Adsorbed Au atoms appear as bright crescent-shaped features. Image parameters: V_S = 2.0 V, I_T = 100 pA, 7 nm × 7 nm.

The STM employed for these studies also allows higher resolution imaging of adsorbates. Figure 3.14 shows 6 nm × 4 nm STM images of adsorbed Pd and Au atoms, exhibiting different shapes. Figure 3.14a shows the typical contrast observed for Pd atoms bound between SiO_2 bilayer and metal support, which can be described as butterfly or crescent shape. It appears to be located off-center in the six-membered rings of the SiO_2 network. DFT calculations of this system verified that the adsorption site at the threefold-hollow site with respect to the substrate and off-center with respect to the silica ring structure is energetically preferred. Figure 3.14b shows Au adsorbates on an amorphous region of the silica bilayer. The majority of adsorbates appear in a similar

crescent shape as palladium adsorbates. A small fraction of the adsorbates appear in an almost-round shape, while also possessing a significantly larger apparent height than the crescent-shaped adsorbates. These round adsorbates are assigned to Au atoms on top of the bilayer film. DFT calculations indicate a weak adsorption on the surface, "with the preferred adsorption site in the center of the ring where the dispersion interaction is maximized".[92]

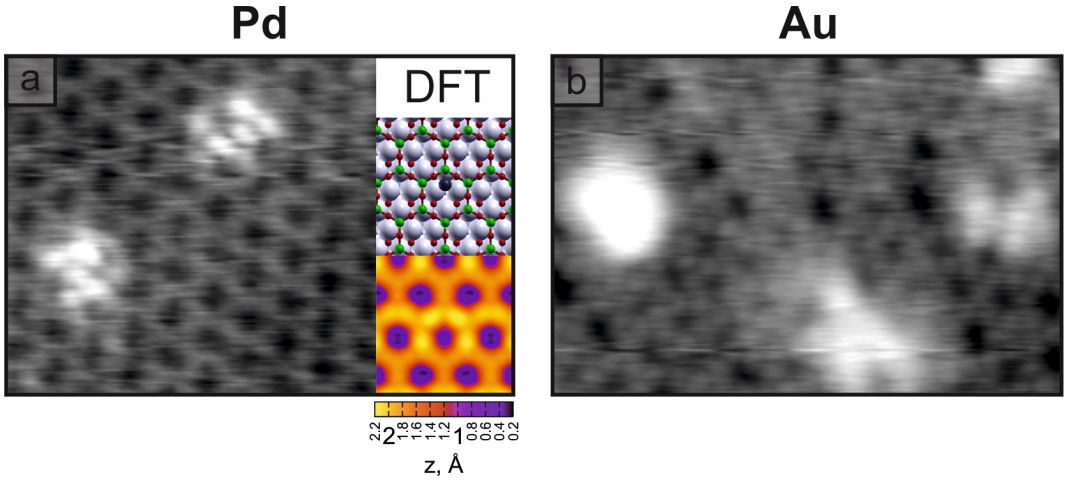

Figure 3.14: High-resolution STM of metal adsorption. a) High-resolution STM of Pd single atoms adsorbed over crystalline region of SiO_2/Ru(0001). Image parameters: V_S = 2.0 V, I_T = 10 pA, 6 nm × 4 nm. Inset: DFT model of a Pd atom adsorbed at oxide-metal interface, below simulated STM contrast from DFT (reproduced with permission from [92]). b) High-resolution STM of Au single atoms adsorbed over amorphous region of SiO_2/Ru(0001), exhibiting two different shapes. Image parameters: V_S = 1.0 V, I_T = 100 pA, 6 nm × 4 nm.

All of the adsorption features referred to did not diffuse on the surface during the entire investigation with STM. Furthermore, intentional manipulation of atomic species with the STM tip was not possible, which implies that the majority of metal atoms are bound below the surface. X-ray photoelectron spectroscopy (XPS) measurements were carried out in our department to verify this assumption.[92, 94] Due to technical limitations, these experiments were carried out at higher temperatures (~150 K), resulting in higher mobility and more clustering of the metal atoms. Two distinct peak positions in the XPS spectra were assigned to metal clusters and single metal atoms, respectively. Measurements at more grazing angles are generally more sensitive to surface species. Moving the collection angle from the surface normal at 0°, to 65°,

the features assigned to single metal atoms were observed to decrease in intensity. Hence, XPS corroborates the assumption that single metal species are bound beneath the surface of the silica bilayer.

Both STM and XPS studies suggest subsurface adsorption of the metal atoms. This leaves the possibility of metal atoms adsorbing within the silica bilayer or penetration through the material and eventual adsorption at the interface of silica and ruthenium. The preferred adsorption site as well as the size-selective mechanism observed in STM can be understood with the help of DFT calculations carried out in the group of Prof. Gianfranco Pacchioni.[92] First, adsorption energies on a bilayer slab were considered. For both Pd and Au, weak adsorption energies, mainly consisting of van der Waals contributions, were found in the case of adsorption on the surface. This is concurrent with the finding that only few adsorbates were positioned on the top layer. The energetically optimal position for surface-adsorption was found to be in the center with respect to the silica rings. Adsorption within the silica bilayer was not favoured. Instead, binding at the interface was found to be energetically the most favorable state. Both Pd and Au atoms were found to donate some electron density to the Ru(0001) substrate, which is in agreement with electronic shifts observed in XPS.

In order to elucidate the size selective adsorption behavior, energy barriers for metal atom penetration through each ring size were determined with DFT by our collaborators. For this investigation, unsupported cluster models as shown in the bottom of Figure 3.15 were used to model ring sizes from four- to nine-membered. It was found that Pd atoms can permeate through a six-membered ring without experiencing any barrier. Au on the other hand, has to overcome significant barriers for permeating through a six-membered ring and still perceives a certain energy barrier for diffusing through a seven-membered ring. No energy cost is found for the penetration through an eight-membered ring. This finding is in line with the observation in STM of Au atoms binding to domain boundaries, which possess eight-membered rings.

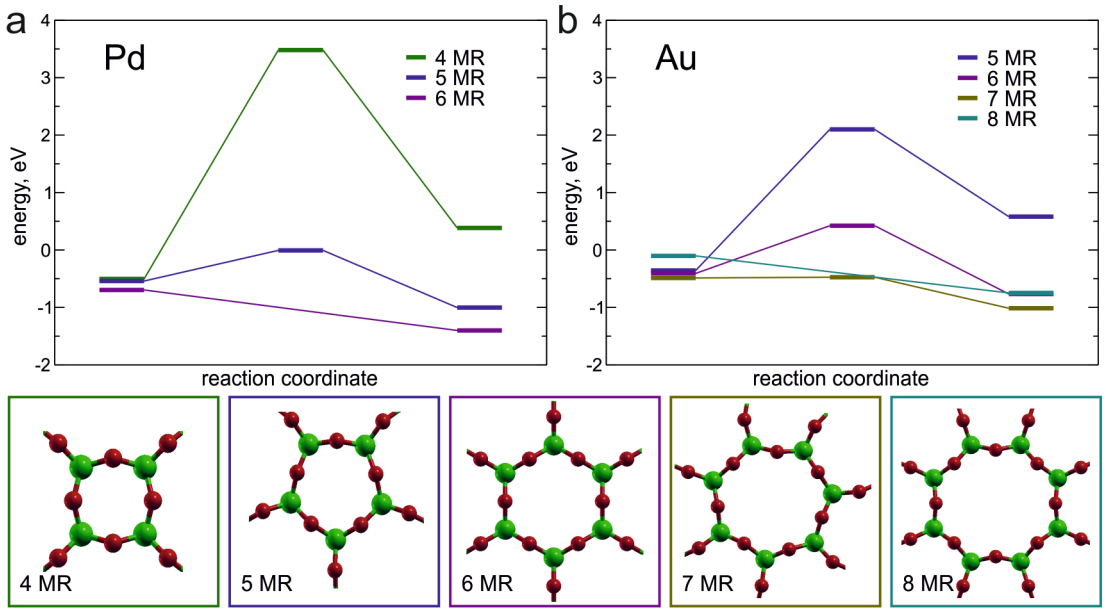

Figure 3.15: DFT Energy barriers for atom penetration through different rings (reprinted with permission [92]). a) Energy barriers for Pd atom penetration through four-membered, five-membered and six-membered ring. b) Energy barriers for Au atom penetration through five-membered, six-membered, seven-membered and eight-membered ring. Bottom: model structures for silica clusters that were used to estimate the barriers in DFT.

A similar study was previously carried out for adsorption of Pd, Ag and Au atoms on a silica monolayer supported on Mo(112).[36, 95] This thin film is covalently bound to the metal substrate and exhibits mainly hexagonally ordered domains with six-membered rings. The strain in the structure is only released by domain boundaries, consisting of four- and eight-membered rings. It was found that Pd ad-atoms show no preference for either binding site on the film, while Ag ad-atoms penetrate through the eight-membered rings with a higher preference. This can be intuitively understood by looking at the van der Waals radii. Pd is listed with 163 pm, while Ag is significantly larger with 172 pm.[96] Au atoms however, while listed with an intermediate van der Waals radius of 166 pm, do not penetrate through the crystalline silica film and only bind to the domain boundary, where larger rings are present. This behavior is in line with our observation on the bilayer film. The structure selective adsorption behavior is influenced by the electronic structure of the metal species. Ag and Au, have occupied 5s and 6s states, while the Pd 5s

states are unoccupied. This leads to a stronger repulsive interaction of the penetrating Ag and Au species with the electron density of the oxide structure.

Various coverages were deposited in this study, however, no consistent variation of adsorption site or particle size was observed in the low-temperature environment. Adsorbate density scales linearly with deposition time. The reduced thermal mobility prevents the metal atoms from aggregating. This allowed us to study preferred adsorption sites, while other pathways like cluster formation are blocked. Therefore, the observed mechanism of size-selective adsorption by the network of silica rings is assumed to hold for penetration of other species. Employing the 2D silica film as a membrane for diffusion of gases or liquids will exploit exactly this feature. Especially in the case of gas mixtures, the silica network can act as a size-selective filter. Further experiments and theoretical studies already explored the penetration of other metal species[97] and small molecules[98–100] through the bilayer. Additionally, the intercalation properties of 2D silica may be exploited to create large-scale van der Waals solids.

In conclusion, the adsorption of small metallic species over the silica bilayer film has been studied. A structure selective penetration behavior was found and is explained mainly by the electronic structure of the adsorbing species. Exact energetic barriers for penetration of different ring sizes can be determined with the help of DFT calculations and threshold ring sizes for successful penetration can thus be predicted. Together with a good understanding of the amorphous ring size network gained from studies presented in Section 3.1, the application of the silica bilayer as an atomic or molecular sieve becomes feasible.

3.3 Chemical and structural stability of a silica bilayer

After sufficient characterization of the film on the ruthenium substrate, the robustness of the silica bilayer system must be investigated in anticipation of transferring the silica sheet. On the one hand, the procedure of transferring the silica bilayer from the growth substrate to a different target substrate is bound to exert a certain amount of stress on the structure. On the other hand, a more stable system may ultimately be used in a larger array of technological applications.

We mainly use two characterization methods for ascertaining whether the silica film withstands a treatment. Both were carried out on different positions across the sample, to ensure homogeneous coverage. In AES, the surface coverage with a material containing Si is established. In LEED patterns, a ring feature is characteristic for the amorphous structure prevalent in our bilayer films.

We have approached the study of the film stability in two ways: First, by removing the system from UHV and exposing it to different environments for a limited amount of time. Characterization was carried out after the sample was transferred to UHV again. This study is described in Section 3.3.1.

Secondly, we investigated the structure of the silica bilayer directly in a liquid environment. Here, we were able to use a state-of-the-art liquid-AFM, allowing us to study the local structure of the silica bilayer directly while immersed in liquids. Those results are presented in Section 3.3.2.

3.3.1 Stability in air and in solvents

Bulk silica is known to be an inert material, which can withstand high temperatures, pressures and many chemicals. Can the same be expected for an ultrathin silica bilayer, which was grown under UHV conditions?

We explore this question by exposing the ruthenium-supported silica bilayer to some of the most commonplace solvents that occur in a chemistry laboratory. Any reactivity that is found for the silica film towards water, ethanol or acetone, must intuitively be assigned to defect sites in the network, which are more reactive than regular network positions.

Another effect that might be expected from the solvent treatment is the intercalation of solvent molecules and eventual adsorption between the oxide film and the substrate. Such an adsorption behavior has been observed for single metal atoms, as described in detail in Section 3.2. The solvent molecules employed for this study are significantly larger than single gold and palladium atoms. However, access for molecules to the interface can be gained not only through large rings, but also open patches in the film. The aforementioned open patches resulting from partial coverages (see Figure 2.6) are found to be as large as 30 nm across, which will potentially admit a variety of solvent molecules. As the solvent deposition is carried out at room temperature, the molecules possess a significantly larger mobility, enabling them to find access sites to the interface. Intercalation of large amounts of solvents is expected to decrease the adhesion forces holding the silica bilayer on the ruthenium substrate. This process may even lead to full delamination of the film.

The samples were prepared in UHV, according to the procedure laid out in Section 2.2. They were characterized prior to solvent exposure by STM, LEED and AES. The treatment procedure consisted of the following steps:

- removal from UHV-chamber via air-lock
- deposition of a drop of solvent, followed by a short waiting time (5 mins)
- rinsing the entire sample with same solvent
- drying the sample with pressurized air
- transfer into UHV chamber including 10 hour degas at 400 K
- oxygen annealing step, 10 mins, 1243 ± 5 K, 2×10^{-6} mbar O_2

The entire procedure was repeated for each solvent. After the complete procedure, samples were again characterized using LEED and AES. All LEED patterns presented in the following figures were taken at electron energies of 120 eV. An overall asymmetry of the LEED pattern is caused by an offset in the alignment of the sample in front of the detector screen. This misalignment was due to a damaged sample clasp at the time of the measurements. All AES spectra were recorded with a primary beam energy of 3 kV.

Figure 3.16 summarizes the results from the treatment of the silica film with ultrapure water. Before the treatment, the LEED pattern shows clearly visible hexagonal reflexes, which are assigned to the Ru(0001) surface. A clear ring feature indicates the mainly amorphous silica bilayer. A certain crystalline fraction of the silica bilayer is manifested however, in the faint (2×2) superstructure.

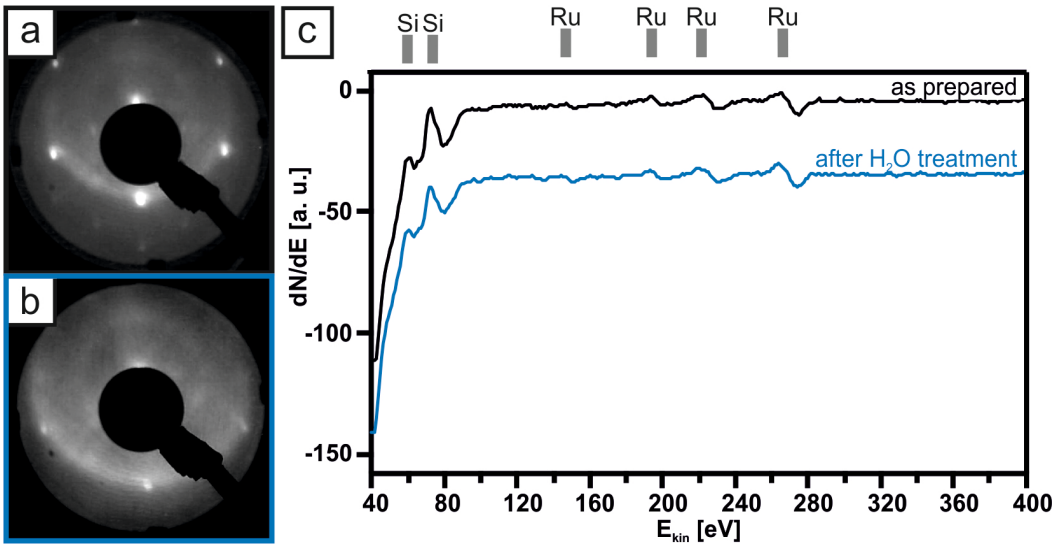

Figure 3.16: LEED and AES on silica bilayer before and after treatment with ultrapure water. a) LEED pattern before H_2O treatment. b) LEED pattern after H_2O treatment. c) AES spectra before and after H_2O treatment, with typical peak positions for Si and Ru indicated.

In Figure 3.16c, the corresponding AES spectra are shown and the typical peak positions for Si and Ru are marked. The comparison from before and af-

ter the solvent treatment shows that the silica film is not affected by the influence of water. Both LEED images exhibit the clear ring feature, indicating a structure with short-range order. The position of the pattern on the fluorescent screen is slightly shifted, due to an offset in the sample position in front of the LEED optics. The AES spectra both show comparable amounts of Si on the surface before and after the solvent treatment. Both LEED and AES measurements were carried out on different positions over the sample surface, and indicate that the crystal coverage remained the same throughout the procedure.

The equivalent measurements for treatment of the silica bilayer with ethanol are presented in Figure 3.17. Panel a and b show the LEED patterns of the silica film before and after solvent treatment, respectively. The ring pattern, which is indicative of the amorphous silica bilayer, dominates the LEED pattern both before and after the ethanol treatment.

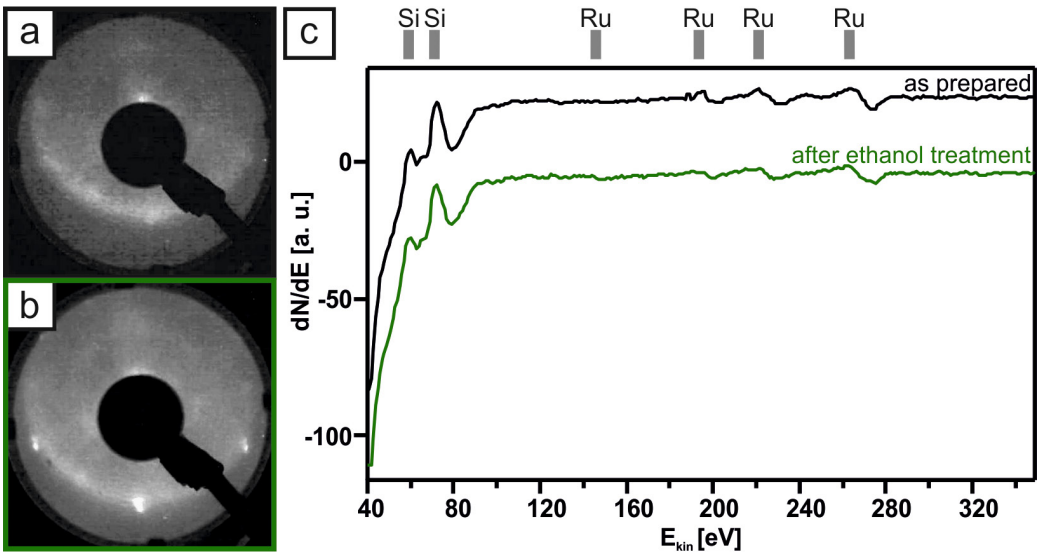

Figure 3.17: LEED and AES on silica bilayer before and after treatment with ethanol. a) LEED pattern before ethanol treatment. b) LEED pattern after ethanol treatment. c) AES spectra before and after ethanol treatment, with typical peak positions for Si and Ru indicated.

From the AES spectra, it is obvious that the silica sheet is not affected by the ethanol treatment. By measuring on several positions on the surface, this consistency was confirmed for the entire sample.

For treatment with acetone, the same behavior as with H_2O and ethanol is observed. The corresponding results are shown in Figure 3.18. The ring is the dominating feature in LEED, indicating an amorphous structure. No significant change is observed here, comparing the LEED patterns before and after treatment. In AES, the amount of silicon on the surface is stable.

This study shows that the silica bilayer sheet is extremely robust against ambient and different liquid environments. Like its bulk counterpart, it does not undergo chemical reactions with water, ethanol, or acetone. This inertness is assigned to the fact that the two silica layers are self-saturated and very low in defect sites.

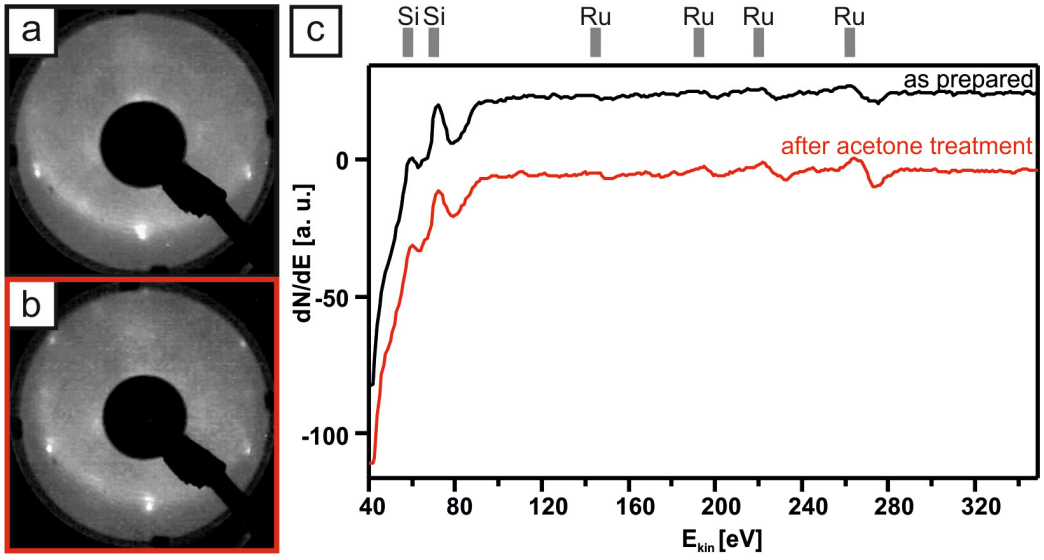

Figure 3.18: LEED and AES on silica bilayer before and after treatment with acetone. a) LEED pattern before acetone treatment. b) LEED pattern after acetone treatment. c) AES spectra before and after acetone treatment, with typical peak positions for Si and Ru indicated.

The adhesion of the bilayer on the substrate is also strong enough to prevent intercalation of solvents. Even though the deposited solvent molecules had sufficient mobility to reach access sites in the large open patches of the film

system, the adhesion forces were not weakened to the extent that the film would delaminate during the rinsing step. Hence, the attractive interaction between silica sheet and substrate is relatively strong. This can be assigned to the absolute flatness of the bilayer and the substrate. Nominally weak van der Waals forces acting between a large number of atom pairs over the surface accumulate to a high overall attraction. To overcome this attractive force will be the main challenge for developing an exfoliation technique (see Section 4.1.).

3.3.2 The structure of 2D silica in water

In the previous section, we have reported on the stability of a silica bilayer sheet against commonly used solvents. The samples were exposed to a small volume of solvent and subsequently rinsed and dried. After transferring the samples back into a UHV chamber, the retention of the structure was demonstrated using diffraction and element sensitive spectroscopy. The requirements of ultrahigh vacuum for these surface science techniques meant that the structure analysis was only possible *after* solvent exposure.

We now want to understand how the structure behaves under the influence of a liquid environment. This knowledge can be used to assess the implications of water (or other solvents) impacting the silica bilayer in a technological application such as surface coating. Furthermore, a liquid environment is expected for the usage of the material in any kind of biological system. This is possible by imaging the sample in situ in a special liquid-AFM that was introduced in Section 2.1.3.

The silica bilayers were prepared according to the procedure laid out in Section 2.2 and characterized using LEED, AES and STM. The LEED pattern indicating mainly amorphous structures and AES spectra were recorded on different positions over the sample to ascertain an even coverage of the substrate. From high resolution STM images, the area of visible open patches in the film was evaluated to determine the exact coverage. The samples trans-

ferred from UHV to the liquid environment ranged over a large range of coverages from 1.5 ML to 1.9 ML. For the transfer from the UHV chamber we used a designated air lock and provided a flow of nitrogen gas, reducing exposure time of the sample to air prior to covering the sample surface in ultrapure water to less than 10 s.

The images in the liquid-AFM were obtained at room temperature in ambient conditions. The sensor unit and the sample surface were immersed in a small volume of ultrapure water during the measurement. With this technique, we are able to record very large overview images of the sample; one such image of 200 nm × 200 nm is shown in Figure 3.19.

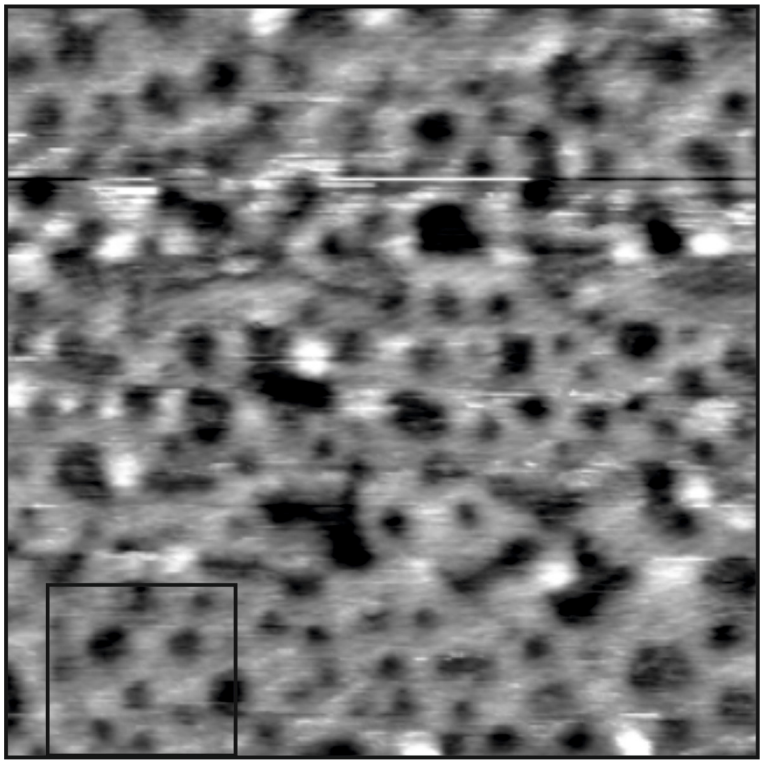

Figure 3.19: 200 nm × 200 nm AFM image of silica bilayer in ultrapure water. The image shows a large terrace with open patches of different sizes. The square frame in the lower left corner indicates the region where Figure 3.20 was zoomed in. Imaging parameters: f = 409 kHz, A = 1 nm, k = 24.7 N/m.

This image exhibits a terrace of the SiO_2 bilayer with many open patches in an environment of ultrapure water. These large holes result from the deposition of less than 2 ML of silica and mainly expose the ruthenium substrate.

This sample was prepared with a coverage of 1.7 ML. A few higher lying features that appear very bright in the image are tentatively assigned to air bubbles that get trapped on the surface. By scanning over them repeatedly with the AFM sensor it has been possible to “pop” these bubbles.

A smaller frame in the lower left corner of Figure 3.19 indicates the area that is shown in higher resolution in Figure 3.20a. Panel b shows an STM image that was acquired in UHV of the same sample preparation before transfer from the UHV chamber. Both images show the flat film and holes with five to ten nanometers in diameter. The image taken in water exhibits significantly higher noise levels, but an overall morphology that is comparable with the image in panel b. On the STM, the effect of a double-tip is visible in the shadows around holes. Also, the left edge of the frame exhibits an artifact that is caused by a temporary piezo charging effect. Even with these different measurement artifacts, the overall morphology of the two images is strikingly similar.

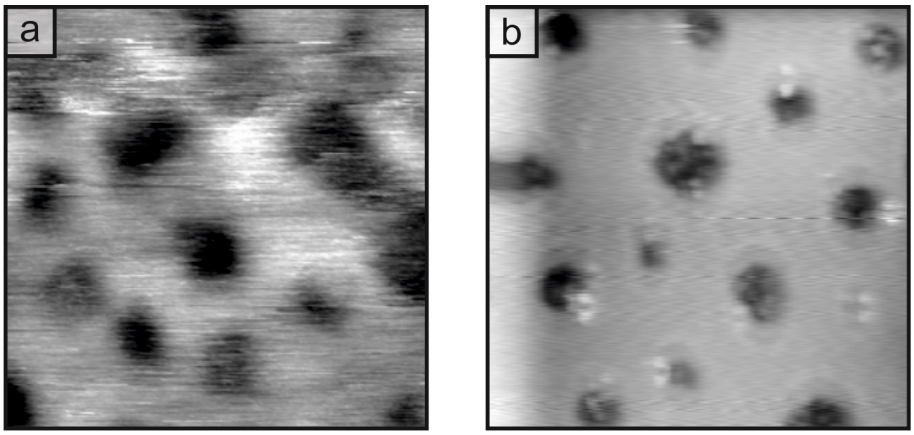

Figure 3.20: a) 50 nm × 50 nm liquid-AFM of silica bilayer in water. Imaging parameters f = 409 kHz, A = 1 nm, k = 24.7 N/m. b) 50 nm × 50 nm STM of same sample, taken in UHV. Imaging parameters I_T = 50 pA, V_S = 0.5 V.

The overall impression of the two images showing a comparable morphology is quantified in the following table. Here, we evaluated the open patches in several images both from liquid-AFM and from UHV-STM regarding their size, depth and density on the surface. The features are in quantitative agreement for liquid-AFM and UHV-STM.

	liquid-AFM	UHV-STM
Hole Density	4.2×10^{-3} nm^{-2}	4.0×10^{-3} nm^{-2}
Hole Size	32 ± 27 nm²	21 ± 16 nm²
Hole Depth	0.4-0.5 nm	0.4-0.45 nm

While the image shown in Figure 3.20b shows a pristine preparation in ultra-high vacuum, panel a was taken after one week of exposing the sample to water. The main limitation for imaging this system stems from air bubbles which accumulate on the surface over time. Some additional material on top of the structures has also been observed after extended periods of imaging. This is tentatively assigned to debris from the sensor cantilever itself, as the imaging chamber is designed to minimize dust contamination from outside the measurement cell.

In liquid-AFM, long-range electrostatic interactions are assumed to play a large role. In an aqueous environment, surfaces of the sample and of the tip may undergo ionization, such as hydroxylation reactions. Depending on the respective materials of tip and sample, the resulting electric double layers lead to long-range repulsive or attractive forces, which interfere with high resolution imaging. Salt solutions are often used instead of ultrapure water, as they have been shown to suppress the electric double layer forces.[101] We have employed this strategy to improve resolution on the silica bilayer film in liquids.

Figure 3.21a shows a 5 nm × 5 nm image of the silica bilayer in a 400 mM NaCl solution. It was recorded on a flat terrace, such as can be seen between the open patches in Figure 3.20. The resolution was found to improve significantly when imaging in a solution of sodium chloride. Small features are recognizable which are comparable in size to the n-membered rings that form the amorphous 2D network. A few of those features are marked with white dotted circles. For comparison, Figure 3.21b shows a high-resolution STM image obtained on a similar silica film preparation in ultrahigh vacuum. Here, the

positions of Si atoms are clearly visible. A few of them are marked with green circles in the bottom of the image. The atoms are arranged in the amorphous ring network and a few rings are marked with dotted white circles.

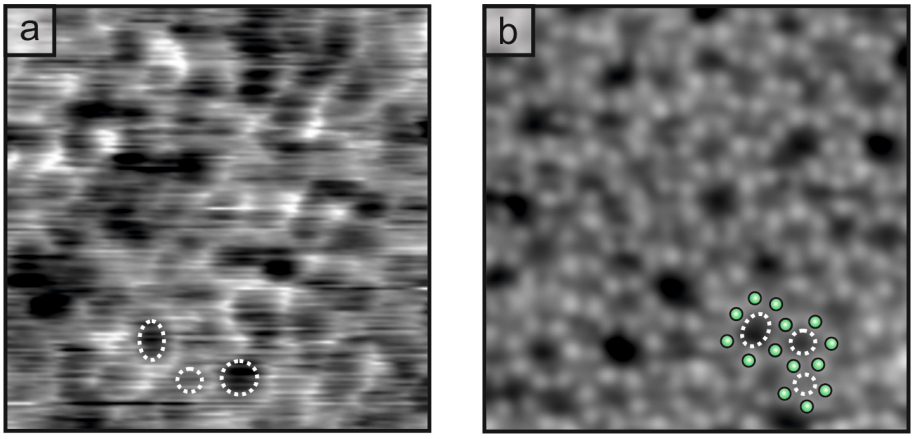

Figure 3.21: a) 5 nm × 5 nm liquid-AFM of silica bilayer in salt solution. Imaging parameters f = 337 kHz, A = 0.2 nm, k = 26.4 N/m, 400 mM NaCl solution. b) 5 nm × 5 nm STM of a comparable sample, taken in UHV. Imaging parameters I_T = 50 pA, V_S = 2 V.

Overall, we find good agreement between the structural features of the silica bilayer in liquids and in UHV. Over prolonged exposure, no solvation effects like migration of step edges or disappearance of the film has been observed. This indicates a high stability of this surface against an aqueous environment, in agreement with evidence presented in Section 3.3.1.

The combination of well-defined samples prepared in UHV and imaging in liquid environments is a powerful strategy to test further model systems under application conditions.

4. Transfer of a two-dimensional silica bilayer

In the previous sections, an atomically flat SiO_2 bilayer has been described, which exhibits a complex network structure and size-selective adsorption behavior. These properties indicate promising applications of the bilayer film as a 2D material.

From previous studies of the film it is known to be self-saturated and weakly bound to the growth substrate.[33, 34] In fact, when this system was presented for the first time, the adhesion energy between substrate and oxide was predicted to be comparable to the interlayer adhesion in graphite.[33] We have shown in Section 3.3, that like its bulk counterpart, the bilayer is chemically inert, can withstand high temperatures and remains stable at atmospheric pressure. Furthermore, it shows structural robustness against solvent treatments and prolonged exposure to water. The observed high stability is surprising for a film of this thickness and indicates a low number of reactive defect sites.

These preliminary studies suggest that the silica bilayer might be stable enough to remove it from its substrate while preserving its structure. The successful transfer to a new substrate is the prerequisite for making the film accessible to many technical applications. If the film can be transferred post-growth to new substrates, then applications are not limited to substrates that withstand the growth of the bilayer film in UHV and at high processing temperatures.

We will report the results achieved on transfer procedures for a silica bilayer in the following sections. Section 4.1 discusses commonly known methods to exfoliate 2D materials. Drawbacks and applicability of each method to SiO_2/Ru(0001) will be commented on and a working method to exfoliate the bilayer sheet in its entirety will be presented.

Section 4.2 describes the results of a transfer of the exfoliated SiO_2 film to a TEM grid, while Section 4.3 presents the transfer to a Pt(111) single crystal.

4.1 Exfoliation of a two-dimensional silica bilayer

Ever since graphene was re-discovered in 2004,[102] the field of 2D materials has grown tremendously. As single-layer and bilayer materials consist entirely of surface area, their properties are often dramatically different from those of the corresponding bulk material. Furthermore, charge and heat transport are confined to a plane, which leads to new phenomena.[8]

All methods for creating nanomaterials can be categorized into top-down and bottom-up methods. In top-down approaches, the nanosized material is obtained from a bulk material that is reduced to smaller dimensions. In the field of 2D materials, this is mainly achieved by exfoliating a layered bulk material into thinner and thinner sheets, until a single layer is obtained. A bottom-up method involves creating a nanoobject from single atomic or molecular building blocks. Building blocks that assemble into two-dimensional structures in a self-guided, template-free process are well known from natural structures such as cell membranes.[103] This principle is mainly used in the self-assembly of bio- and macromolecules, which consist of some form of directional interaction, that can be used for guiding 2D self-assembly.[104] Recently, a similar material has been created from two to five nm sized inorganic nanoparticles, which possess a dipole moment and exhibit directional hydrophobic interaction. These particles assemble into free floating sheets in aqueous solution.[105] In order to design 2D materials from significantly smaller building blocks, phase interfaces can be used to guide self-assembly into two-dimensional structures. In the creation of a silica bilayer from building blocks provided in the gas phase, natural substrate choices are single-crystals with flat surfaces or stacks of other 2D materials. Often the intended application for a 2D material involves a support material which is not suitable as a growth substrate. In this case, exfoliation from an appropriate growth substrate and subsequent transfer can be a solution to obtain high quality 2D materials for the desired application. Therefore, exfoliation methods for 2D materials are useful in order to develop new types of nanosheets, both from top-down processes and from bottom-up processes.

A reliable transfer method for a 2D material allows that structurally perfect ultrathin layers can first be created by employing the ideal growth substrate and preparation procedure, but the applicability is not limited by this substrate requirement. For this to be the case, the 2D material of choice must withstand the removal from the growth substrate as well as a deposition procedure to the new substrate. During either step, 2D materials can experience mechanical stress, which often leads to tears, cracks and wrinkles in the transferred film.[106–109]

As the field of 2D materials is still relatively young, a variety of transfer methods have been presented, without one of them being established as clear preference over others. Each method may have a comparative advantage for a certain sample system. Since this work, to our knowledge, represents the first attempt at transferring an atomically defined silica bilayer, several methods from 2D materials literature were tested on this system. We strongly believe that in such a case, unsuccessful attempts provide useful insights that benefit further studies. Hence, we will give a brief overview of all exfoliation methods applied to the silica bilayer system and finally present the most effective procedure we use for the exfoliation of a silica bilayer from ruthenium.

In order to test different exfoliation methods, a general exfoliation protocol was developed, and the central exfoliation step was varied to find a successful method for removing the complete bilayer sheet from the substrate. The silica films were prepared in UHV, as described in Section 2.2. They were characterized using STM, LEED and AES prior to exfoliation. The general steps for each procedure are:

- removal from UHV-chamber via air-lock
- exfoliation step (variations described in the following section)
- transfer into UHV chamber including 10 hour degas at 400 K
- oxygen annealing step, 10 mins, 1243 ± 5 K, 2×10^{-6} mbar O_2

Success of the exfoliation was mainly ascertained using LEED and AES, which is shown in the comparative study in Section 4.1.1. LEED can be used

to indicate the presence of an amorphous material with short-range order, while AES can provide evidence on whether Si is present on the surface. Both methods are used on different positions on the sample, and information on the coverage is inferred. They provide an overview of the whole sample surface in a significantly shorter time than high-resolution microscopy. We provide supplementary microscopy data for the case of a successful exfoliation, presented in Section 4.1.2.

Note that the same experimental steps were carried out after each of the solvent treatments described in Section 3.3.1. The silica bilayer was then found to be undamaged by the transfer to air, transfer back into UHV, and a subsequent heating step. We can exclude that any of those steps impair the silica bilayer. Therefore, we can now correlate the result of each procedure with the exfoliation step in particular.

4.1.1 Application of standard methods

The Scotch-tape assisted layer exfoliation used to produce graphene in 2004[102] has garnered significant attention and is easily reproducible due to its simplicity. In scanning probe microscopy, cleaving layered minerals with the help of adhesive tape is a typical approach for creating pristine surfaces.[45] This micromechanical cleavage method can be used to extract single graphene layers from highly oriented pyrolytic graphite (HOPG), a multilayer bulk material. Adhesive tape is placed on the surface of the multilayer material and upon removal exfoliates a thin layer of the material, if the adhesive force of the tape exceeds the interlayer attractive force. The procedure is repeated several times to obtain successively thinner sheets, and finally, single layer graphene. This method is suitable when the layers are held together by relatively weak interactions, often van der Waals forces. The tape can be removed using suitable solvent or etchant solutions. The main drawback of this method is the low yield of truly single layer flakes.[110]

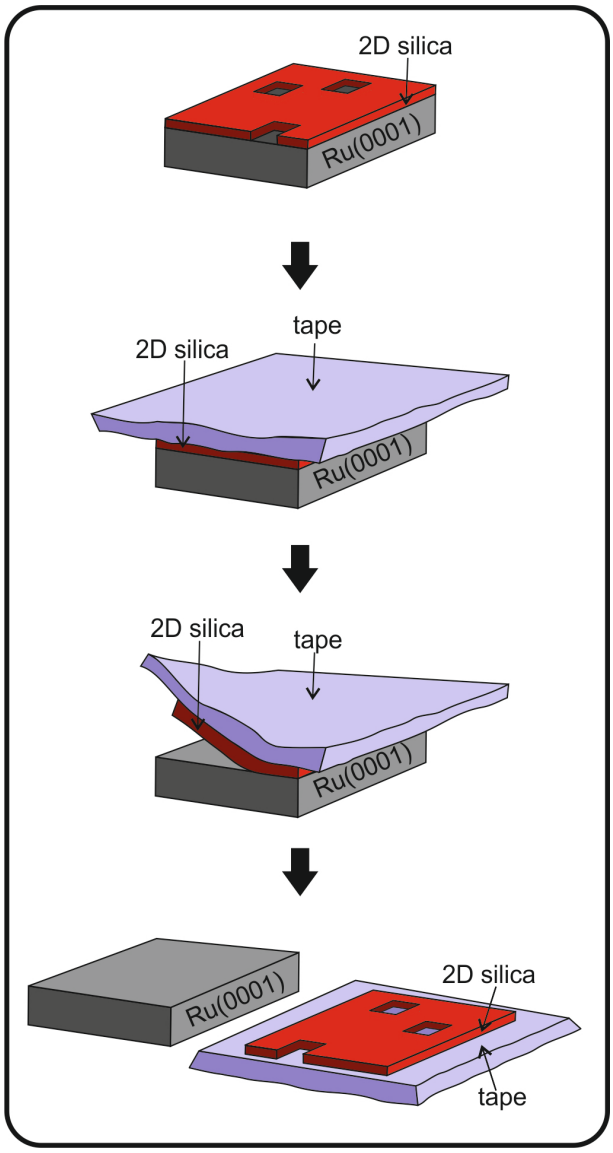

Figure 4.1: Schematic of Scotch-tape assisted exfoliation of silica/Ru(0001). From top to bottom: the silica bilayer is supported on Ru(0001); adhesive tape is placed on the top side; adhesive tape is mechanically cleaved; silica is supported on adhesive tape and the ruthenium surface is clean. This approach failed to exfoliate the silica bilayer from ruthenium.

Furthermore, the mechanical exfoliation is expected to exert mechanical stress on the 2D material during the bending and pulling movements of the procedure. The 2D material therefore must have strong in-plane-bonding to withstand this procedure. Often, the lateral size of single layers that are obtained through micromechanical cleavage is limited due to the grain size of the bulk source material. This prevents efficient scaling up, and therefore mi-

cromechanical cleavage is not the preferred method in industrial thin-layer production. Due to its convenience and simplicity, however, it finds wide application in research laboratories.[16]

The adhesion of the silica bilayer on ruthenium was estimated with DFT calculations to be similar to the interlayer adhesion of graphene layers in graphite.[33] Hence, the Scotch-tape assisted exfoliation was attempted on our thin film system. As indicated in the schematic in Figure 4.1, a silica preparation with sub-bilayer coverage was used for this experiment. The corresponding LEED pattern, shown in Figure 4.2a, exhibits a ring feature, indicating short range order without long range order, which is characteristic for the amorphous 2D silica film. A piece of adhesive tape (brand name *Tesafilm® kristall-klar*) was pressed on the sample and pulled upwards on the assumption that the silica layer would stick to the tape. The ruthenium crystal was transferred back into the UHV-chamber and a short annealing step in oxygen was carried out to remove potential surface adsorbates that interfere with LEED analysis.

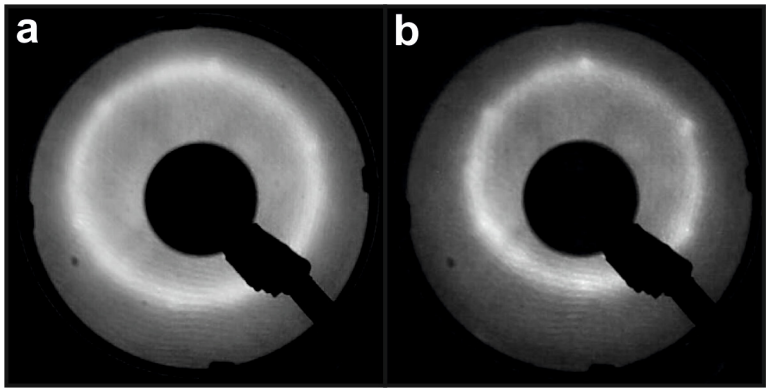

Figure 4.2: LEED of a silica bilayer on Ru(0001) a) before exfoliation using Scotch-tape and b) after exfoliation using Scotch-tape. E_{kin} = 136 eV for both measurements.

LEED carried out subsequently shows that the surface is still covered by an amorphous layer (Figure 4.2b). The small changes in the size and position of the diffraction pattern can be assigned to a slightly different sample position in front of the LEED screen. We must therefore conclude that the amorphous silica bilayer is unaffected by the adhesive tape exfoliation. It is possible that

the adhesive force of the tape is not sufficient to overcome the adhesion of the silica bilayer on the substrate.

A second technique for preparing 2D materials is known as liquid exfoliation or solvent assisted delamination. These terms include a variety of protocols which generally immerse the supported ultrathin layer in a liquid environment. Then, various effects like interface oxidation, ion exchange or solvent intercalation help to decrease the attractive forces that hold the 2D material on its substrate.[111] Treatment of the samples with ultrasound has also been reported as successful.[110]

Liquid-assisted exfoliation methods are successful at producing high yields[110, 112] of single-layer materials. The 2D layer must be bound to the substrate weakly enough to allow access to the interface for solvent molecules or cations. The solvent choice plays an important role for stabilizing the resulting nanosheet dispersion.[16]

As indicated in Figure 4.3, we rinsed the silica films using ultrapure water, ethanol and acetone, respectively. A drop of each solvent was also deposited on the surface with sufficient time (~ 5 mins) for molecules to migrate to the interface between oxide film and substrate crystal. After potential solvent intercalation and thus during potentially weakened substrate adhesion, tape assisted exfoliation was performed. Samples were then rinsed with the respective solvent, allowing for the potentially weakly coupled silica film to “wash off” the substrate. This experiment was performed directly after the solvent exposure treatments that were presented in Section 3.3.1. The samples were then transferred back into the UHV chamber. However, in all three cases (exfoliation with H_2O, ethanol and acetone), the silica layer remained intact. This was shown by comparing LEED patterns, as well as AES spectra, from before and after the transfer. These measurements, presented in Figure 3.16, Figure 3.17 and Figure 3.18, showed no significant difference in the silica film before versus after the solvent-assisted transfer.

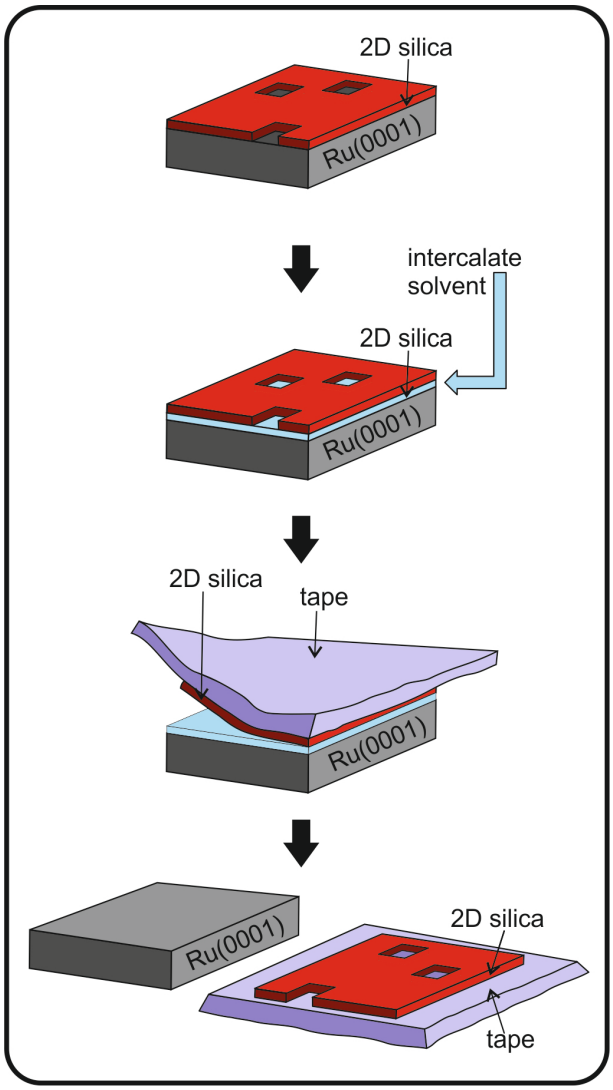

Figure 4.3: Schematic of solvent assisted exfoliation of silica bilayer. From top to bottom: the silica bilayer is supported on Ru(0001), solvent molecules intercalate to the interface, the sample is exfoliated with adhesive tape; silica is supported on adhesive tape and the ruthenium surface is clean. This approach, carried out using water, ethanol and acetone as intercalating solvent, failed to exfoliate the silica bilayer from ruthenium.

Neither adhesive tape assisted nor solvent assisted exfoliation methods yielded silica sheets that could be transferred to new supports. Rather, the presented results demonstrate the remarkable robustness of the 2D silica bilayer. No significant changes were observed when transferring the films to ambient conditions, treating them in various ways and transferring them back into UHV. The material can also undergo additional annealing steps without

changing significantly, as long as they are not harsher than the initial oxygen annealing step which is part of the preparation procedure.

We also used an ultrasound treatment as exfoliation method. Ultrasonication is frequently suggested as a method for production of single layer graphene, which is suitable for high throughput and scale-up.[113–115] If ultrasound intensities and bath temperatures are kept low, inducing defects in the material can be avoided, and unwanted reactions from radicals formed from sonolysis of organic solvents can be prevented.[113, 114] During sonication, the size of nanosheets decreases, typically yielding µm-sized flakes.[16, 110, 113, 115] The general procedure for ultrasound assisted exfoliation is shown schematically in Figure 4.4.

A 2D silica film on Ru(0001) was characterized with LEED, yielding a clear ring feature, shown in Figure 4.5a. AES, presented as black curve in Figure 4.5c, indicated silicon on the sample surface. Both measurements were carried out several times on different sample positions, showing even coverage. The sample then was completely immersed in ultrapure water and treated for 10 mins with a standard ultrasound bath (Bransonic 221, 285 Watts, 50 kHz). After this treatment, the sample was transferred back to the UHV chamber. A LEED pattern obtained on this sample after ultrasound treatment (Figure 4.5b) showed mainly the substrate reflexes and did not indicate the presence of any layer covering the Ru(0001) surface. In AES (Figure 4.5c), small shoulders are still visible in the energy range of Si peaks. They are significantly smaller, however than before the ultrasound treatment.

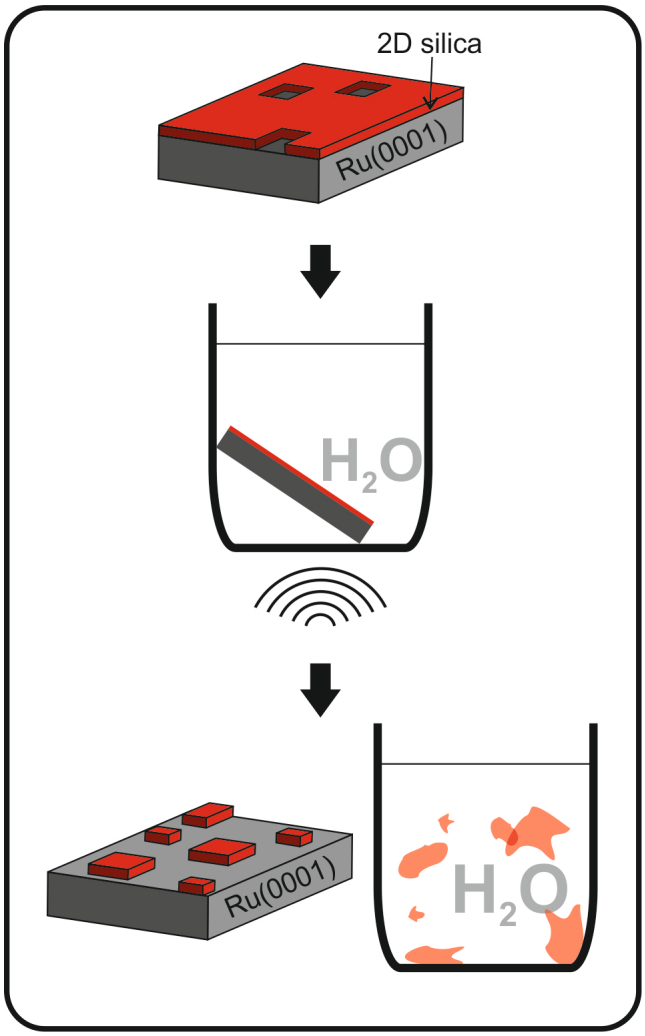

Figure 4.4: Schematic of liquid ultrasound-assisted exfoliation of SiO_2/Ru(0001) in water. From top to bottom: the silica bilayer is supported on Ru(0001); the sample is subjected to ultrasound in a water bath; silica flakes are dispersed in water and the ruthenium surface carries some residues of the silica bilayer. This method was successful in partially removing a silica bilayer from the substrate.

This experiment may serve as an indicator, that ultrasonication is a feasible exfoliation technique. As the silica bilayer is completely invisible to the naked eye, however, it was not possible to identify the exfoliated silica film or pieces of it in the volume of ultrapure water. Therefore, it was impossible to carry out characterization of the exfoliated film. This challenge might be overcome in the future by suitable processing techniques such as centrifuging, which is employed for exfoliated graphene sheets,[16] or filtration, which is used for exfoliated h-BN sheets.[6]

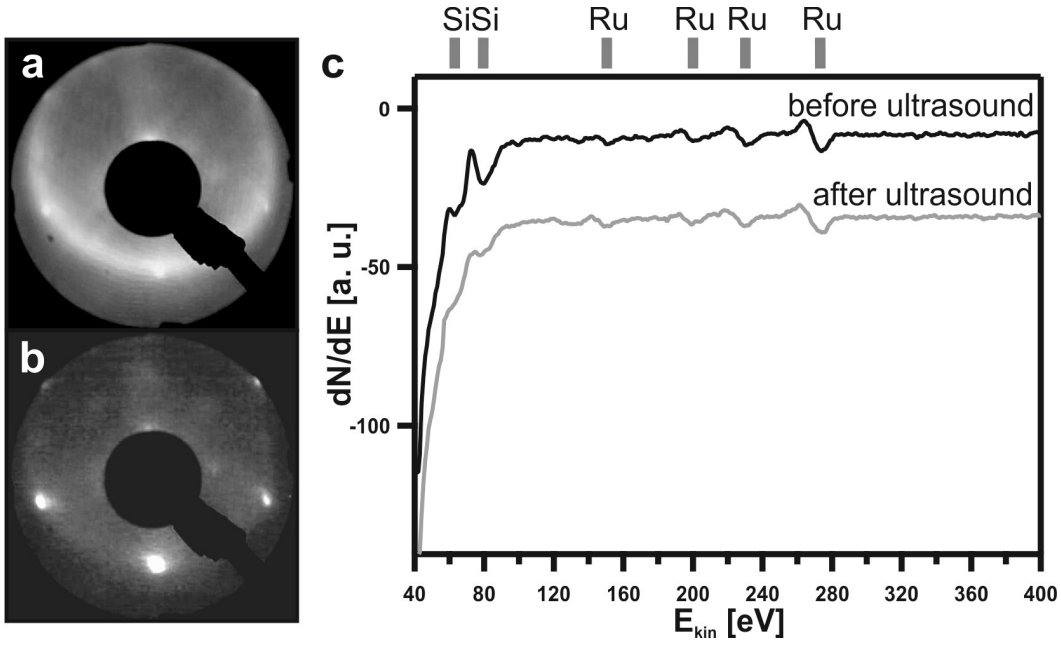

Figure 4.5: Ultrasound assisted exfoliation of a 2D silica sheet from Ru(0001). a) LEED before exfoliation, 130 eV. b) LEED after exfoliation, 130 eV. c) AES spectra before exfoliation (black curve) and after exfoliation (gray curve).

The methods proposed thus far are used to exfoliate both layered materials, like HOPG,[102] and supported thin films, for example MoS_2 on sapphire.[107] The tape-assisted mechanical exfoliation and the solvent treatment did not alter the system, while an ultrasound treatment only partially removed the silica bilayer. It is therefore assumed that the adhesion between the atomically flat ruthenium substrates and 2D silica is too strong for these methods to succeed.

A widely used method, specifically for exfoliating 2D materials grown on atomically flat substrates, consists of a sacrificial etching protocol.[116] This method is mainly used for thin layers that were grown via chemical or physical vapor deposition. These growth processes usually yield large scale, highly ordered films and allow tuning material properties by introducing dopants and precise control of film thickness. The substrates consists of a bulk crystal and a few µm thick surface layer of a sacrificial material.[117] After growing the 2D film, the sacrificial layer is removed by dissolving or etching. The 2D film floats on the etchant solution and can be transferred to a different substrate.[118] If the 2D layer is difficult to identify with the naked eye or if it is

very delicate, a polymer “handle” is attached on top of the layer prior to the etching procedure. Often, Poly(methyl methacrylate) (PMMA) or other polymers are used to create this handle.[109, 119, 120] After removal of the sacrificial layer, the 2D material remains attached to the PMMA handle and can be placed on the substrate of choice, followed by removal of the PMMA.

This method is suitable to produce large scale layers of highly ordered 2D materials by using vapor deposition methods.[121] During the exfoliation, the layers experience minimal amounts of mechanical stress.[120] The complete removal of PMMA is the main challenge in this method, as polymer residue is known to influence the electronic properties of 2D materials.[119, 122, 123]

The sacrificial etching method cannot be directly applied to the SiO_2/Ru(0001) system, as the substrate does not provide a designated sacrificial layer and partial etching of the single crystal substrate is not economical. However, it is mentioned here for several reasons. In general, it is the most important method for producing large-scale 2D materials of high quality, and may be employed in the future for exfoliating silica bilayers that are grown on a suitable support. In the context of this work, the sacrificial etching protocol inspired the development of a PMMA assisted mechanical cleavage method which we used successfully to exfoliate silica bilayers from ruthenium. A schematic of the exfoliation steps is shown in Figure 4.6.

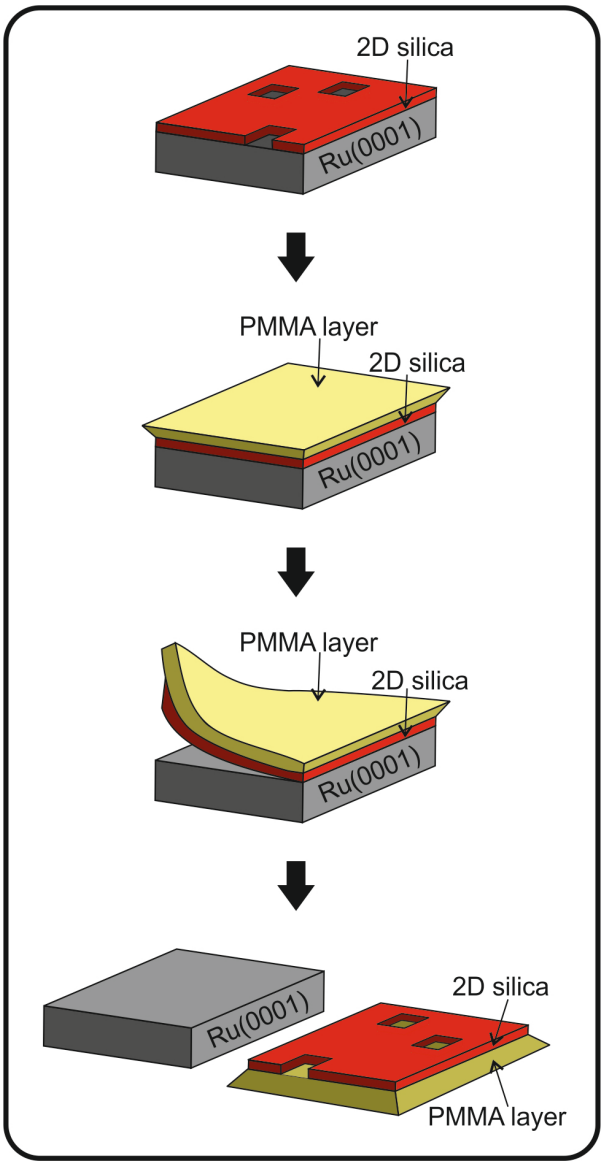

Figure 4.6: Schematic for PMMA assisted exfoliation method. From top to bottom: the silica bilayer is supported on Ru(0001); a PMMA film is deposited on the top side; the PMMA film is mechanically cleaved; the silica bilayer is supported on the PMMA film and the Ru(0001) is clean. This method successfully removed silica bilayers from their Ru(0001) growth substrate.

For this method, a silica film with a coverage between 1.5 ML and 1.8 ML is prepared on Ru(0001), as described in Section 2.2. These films usually exhibit a predominantly amorphous morphology with a characteristic amount of open patches on the surface. The sample is transferred to air and covered with a thin layer of PMMA. To this end, a 20.7 wt.-% solution of PMMA (product name “Polymethylmethacrylat Formmasse 7N”, supplier Röhm GmbH, Darm-

stadt, Germany, now sold by Evonik Industries AG, molecular weight approximately 120 kDa[124]) in acetone is deposited with a spin-coater (~ 1650 rpm) on the sample surface. The concentration of PMMA in the acetone solution should not be significantly higher, as a solution of higher viscosity has been found to adhere insufficiently to the silica bilayer, resulting in unsuccessful exfoliation attempts. Furthermore, it is important to allow sufficient time for the PMMA to dissolve in acetone without the aid of an ultrasound bath, as ultrasonic treatment can lead to scission of the polymer chains.[125] Indeed, we have observed a correlation between PMMA solutions treated with ultrasound and unsuccessful exfoliation attempts. 0.5 ml of the PMMA solution form a PMMA film of approximately 0.3 mm thickness after a drying time of three to four minutes. Firm brushing on the top side of the PMMA during the drying process ensures good adhesion between silica layer and PMMA. The PMMA layer is removed from the sample, exfoliating the 2D silica film from the substrate in the process. An additional piece of adhesive tape is useful for grasping the PMMA layer. The PMMA layer supporting the silica bilayer and the bare ruthenium substrate can then be analyzed separately to verify successful exfoliation.

Figure 4.7 shows the characterization of the ruthenium support. On the left side, the SiO_2 film supported on Ru(0001) before the transfer is shown, as indicated by the schematic in Figure 4.7a. On the right side, the analysis of the substrate after the exfoliation is shown, as indicated by the schematic in panel b. In order to analyze the plain substrate after the exfoliation, it is transferred to the UHV chamber and subjected to a mild oxidation step. Panels c and d show the corresponding LEED images at 120 eV. Before exfoliation, LEED reveals hexagonal reflexes which are assigned to Ru(0001) and a ring feature, which is characteristic for the silica bilayer. After exfoliation, only the hexagonal reflexes corresponding to the plain substrate are visible. Figure 4.7e presents the corresponding AES data. Before exfoliation (black curve), AES shows peaks at 153 eV, 203 eV, 235 eV and 277 eV, corresponding to the substrate. Additional peaks at 63 and 79 eV are assigned to silicon.

After exfoliation (gray curve), these additional peaks are not observed anymore.

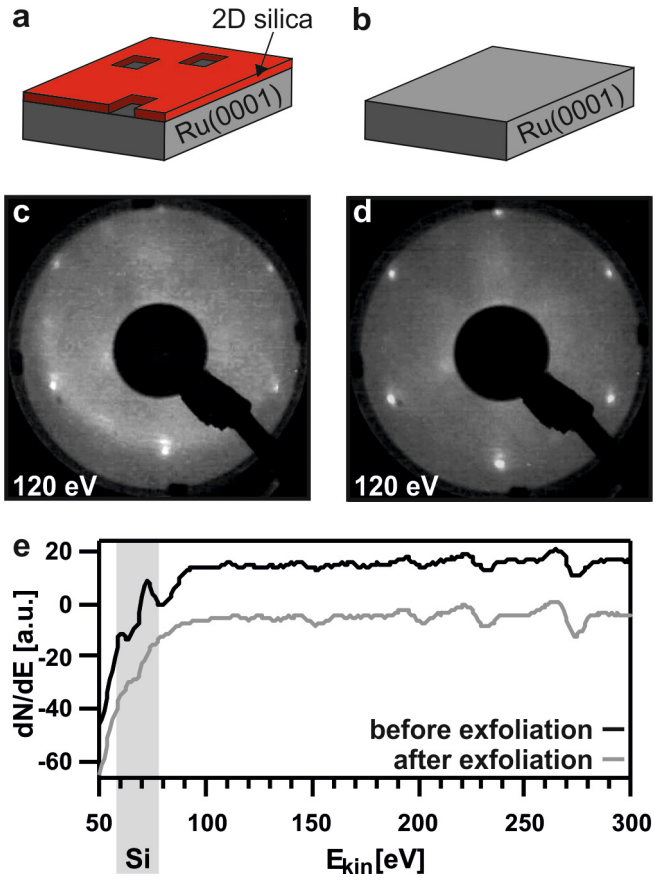

Figure 4.7: PMMA-assisted exfoliation of a silica bilayer from a Ru(0001) substrate. a) SiO_2 film on Ru(0001), c) corresponding LEED, b) plain substrate, d) corresponding LEED, e) AES spectra of bilayer before exfoliation (black curve) and of plain substrate after exfoliation (gray curve).

LEED and AES were carried out on several positions over the sample surface. On all of these points, they showed a successful removal of the silica bilayer. This indicates that the bilayer delaminates from the surface as an entire sheet, rather than partial removal in the form of flakes or pieces.

The experiments carried out in Section 3.3.1 included the same auxiliary steps (transfer to and from air, influence of acetone used for the PMMA solution, and the additional heating step prior to the LEED/AES analysis), but was not found to damage the 2D films. Hence, we can assign the PMMA assisted exfoliation as the cause for the silica features disappearing from LEED

and AES. In the following section, we further investigate the success of a PMMA-assisted exfoliation. We use different microscopy methods to characterize the plain substrate after exfoliation and the PMMA-supported silica film.

4.1.2 PMMA-assisted exfoliation of a silica bilayer

In the previous section, a PMMA-assisted mechanical exfoliation procedure was presented (see Figure 4.6). LEED and AES indicated successful removal of a silica bilayer from its Ru(0001) growth substrate (see Figure 4.7). In this section, we provide microscopy-based analysis of the growth substrate and the transfer medium, thereby presenting additional evidence for the exfoliation procedure. Furthermore, we discuss experimental limitations for this exfoliation method.

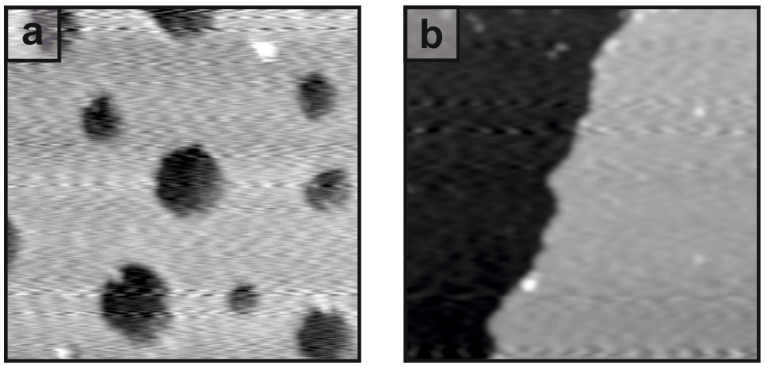

Figure 4.8: a) STM, showing SiO_2/Ru(0001) with 1.6 ± 0.1 ML coverage, V_S = 1 V, I_T = 50 pA, 50 nm × 50 nm. b) STM, showing same sample after exfoliation, V_S = 2 V, I_T = 50 pA, 50 nm × 50 nm.

Figure 4.8a shows a representative STM image of SiO_2/Ru(0001). This sample was prepared with a coverage of 1.6 ± 0.1 ML and exhibits a corresponding amount of open patches, mostly revealing the substrate. Panel b shows the same sample after exfoliation of the silica bilayer. STM reveals the plain ruthenium surface with atomic step edges and a small amount of residual surface adsorbates.

While the characterization of the plain metal substrate can be carried out readily with the surface science techniques available in our UHV setup, the analysis of the silica bilayer supported on PMMA requires different methods. PMMA is not conductive, which forbids the use of electron based analysis techniques. Furthermore, it is expected to show strong degassing effects if brought into a UHV environment. We therefore characterized the morphology of the exfoliated silica bilayer on PMMA, using an ambient AFM. The silica bilayer is imaged exactly in its post-exfoliation state, without further sample cleaning or smoothing treatments.

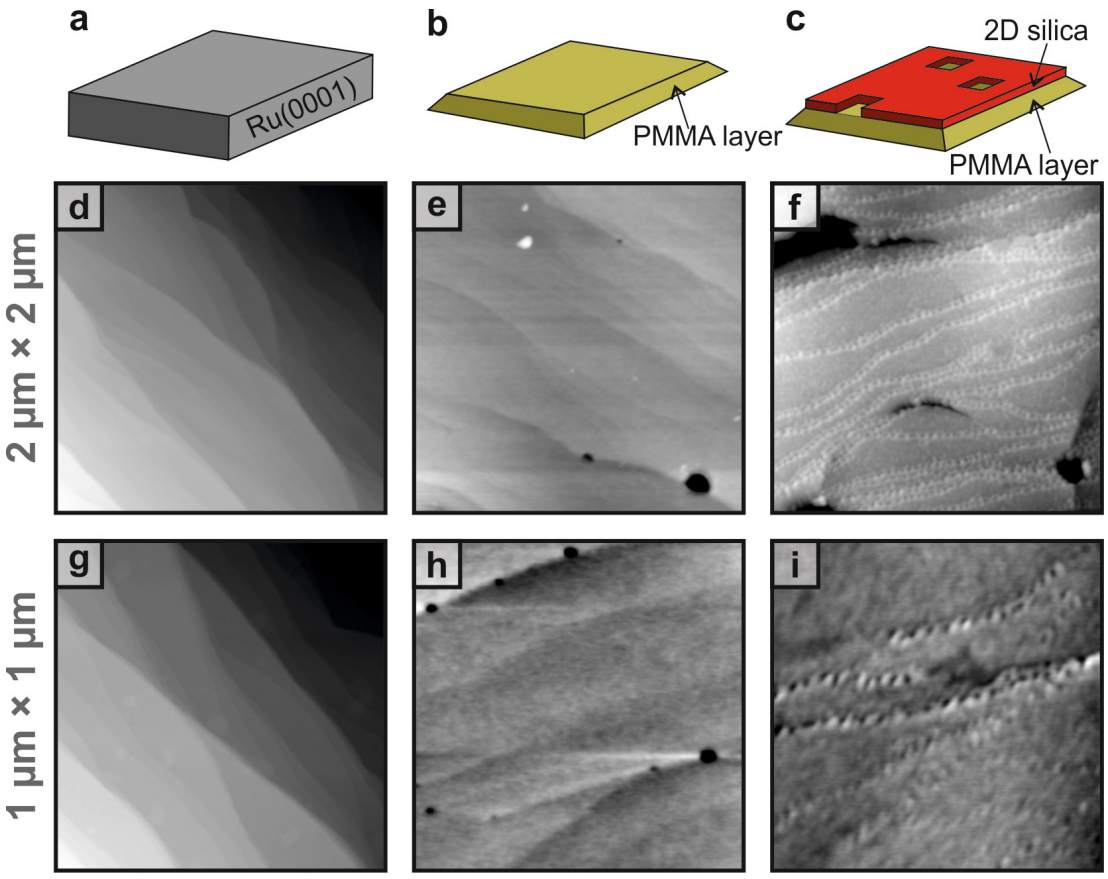

Figure 4.9: Ambient AFM measurements on a clean Ru(0001) crystal (a, d and g) with *f* = 85.9 kHz, on a plain PMMA film (b, e and h) with *f* = 86.4 kHz, and silica supported on PMMA (c, f and i) with *f* = 86.4 kHz.

Figure 4.9 shows the AFM images that were acquired under ambient conditions in air. In order to interpret the specific morphology, we obtained reference images on two additional samples. The panels on the left (schematic a,

images d, g) show a plain Ru(0001) surface, exhibiting mainly atomic steps and flat terraces.

The panels in the middle (schematic b, images e, h) reveal the morphology of a plain PMMA flake. It was prepared by spin-coating a clean Ru(0001)-sample with 0.5 ml of the aforementioned PMMA-solution. The images show that PMMA mainly replicates the morphology of the substrate. Additionally, there are some round protrusions, which are assigned to air bubbles. These are created through the PMMA-solution unevenly wetting the surface. Due to fast drying of the top polymer layer, the bubbles presumably get trapped.

The panels on the right side (schematic c, images f, i) show AFM images of a silica bilayer supported on PMMA. Note that we now observe the silica layer from the underside; due to the way it is exfoliated (in all STM images shown previously, we have always imaged the top layer). The images show bright, elongated features that seem to resemble the atomic steps seen in ruthenium and on plain PMMA. At a closer look, however, the step edges appear to be decorated by round features arranged in chain-like patterns. These could be assigned to air bubbles which form during the spin-coating process. Alternatively, they can be assigned to the open patches in the silica film. In STM studies, these holes are often observed in the vicinity of step edges. Finally, the images on the right exhibit significantly higher roughness than the reference samples, which further indicates, that a silica bilayer, supported on PMMA, is imaged in this case. Besides presumed air bubbles and step edges, no additional topological features can be identified at this length scale. The absence of tears and wrinkles is especially noteworthy, since the mechanical exfoliation procedure leads to significant out-of-plane bending of the 2D silica film. This bending, however, does not seem to damage the thin SiO_2 layer. This corroborates the observation that tensile strength in glasses correlates inversely with the thickness, for example in glass fibres which do not break even at very small bending radii.[126]

The films exfoliated using PMMA-assisted mechanical cleavage all exhibited certain structural features that facilitate successful exfoliation. As illustrated

in the schematic in Figure 4.6, the silica bilayers that were successfully exfoliated, typically exhibited open patches. It was found that exfoliation was only successful for preparations with 1.5 – 1.8 ML coverage. Silica films with coverages above 1.8 monolayers were not affected by exfoliation attempts. We assume that the open patches provide additional step edges that improve adhesion between the silica bilayer and the polymer film. Additionally, silica bilayers at high coverages are more likely to exhibit predominantly crystalline topologies, while films between 1.5 and 1.8 ML are predominantly amorphous. The crystalline silica films possess a honeycomb symmetry that is commensurate with the Ru(0001) substrate. Therefore, a stronger registry is expected for crystalline films, which means a larger adhesion force has to be overcome by the exfoliation procedure.

The exfoliation presented here can serve as a proof of concept, showing that removal of the silica film from its growth substrate is feasible. By modifying the preparation procedure discussed in Section 2.2, different exfoliation methods should, in principle, be possible. The preparation on a ruthenium thin film as a designated sacrificial layer, may allow utilizing the sacrificial etching method. The advantage of this method is that it does not rely as strongly on the adhesion of the PMMA layer and the 2D silica sheet. It is expected that silica films with high coverage (which do not exhibit many open patches) can be exfoliated this way. It is also assumed that films with a larger crystalline fraction which experience stronger registry with the substrate, should be able to be exfoliated using a sacrificial etching protocol.

4.1.3 Summary of 2D material transfer methods

We have applied the most common techniques for exfoliating 2D materials to the system SiO_2/Ru(0001). The silica bilayer adheres strongly to the ruthenium substrate and appears inert against adhesive tape exfoliation as well as solvent intercalation. This was indicated by unchanged features found on LEED and AES before and after these exfoliation procedures. Ultrasound

treatment in water led to a strong decrease of the silica features in LEED and AES, indicating at least partial delamination of the film. At this point, suitable methods for processing the silica sheets dispersed in water are lacking, therefore, this method was not pursued further.

We have found a method to exfoliate a 2D silica film from its growth substrate, using a PMMA-assisted mechanical cleavage protocol. This exfoliation method is cost-efficient and simple to reproduce. We expect that it can be scaled up to deliver larger silica films. Analysis of the plain Ru(0001) crystal after exfoliation indicates that the bilayer is lifted off as an entire sheet. Ambient AFM of the silica sheet supported on PMMA indicates that the film is supported on the transfer medium without any obvious signs of mechanical damage. Due to the PMMA being UHV-incompatible, full characterization of the 2D silica sheet on the transfer medium with LEED, AES and STM was not feasible.

Final evidence for the successful exfoliation can be obtained by transferring the silica film from the PMMA transfer medium to other supports. We present two such transfers in the following sections.

4.2 Transfer of a silica bilayer to a TEM grid

Finding a method to successfully exfoliate a silica bilayer from its growth substrate enables transferring the 2D silica sheet to any desired support, which might be unsuitable for growing 2D silica on it directly. In the previous section, we provided strong evidence that a silica bilayer can be supported on a thin film of PMMA as transfer medium.

Here, we present the transfer of a silica bilayer to a metal grid, which is typically used as sample holder in transmission electron microscopy – in short, a TEM grid. A 2D material supported on a TEM grid would be freely accessible to gases or liquids from either side due to holes in the TEM grid. This is one

approach for preparing so-called freestanding 2D materials. As a consequence, over a certain distance, typically several µm, no supportive interaction, such as a short-range van der Waals force would provide stability. As such a setup requires very high mechanical stability of the 2D film, it is not surprising that very few freely suspended 2D materials have been reported.[30]

We placed a piece of PMMA-supported silica between two TEM grids, as shown by the schematic in Figure 4.10a. We used 200 mesh square TEM grids (hole size 101 µm, pitch 127 µm), with a diameter of 3 mm and made from nickel (manufacturer Pyser).

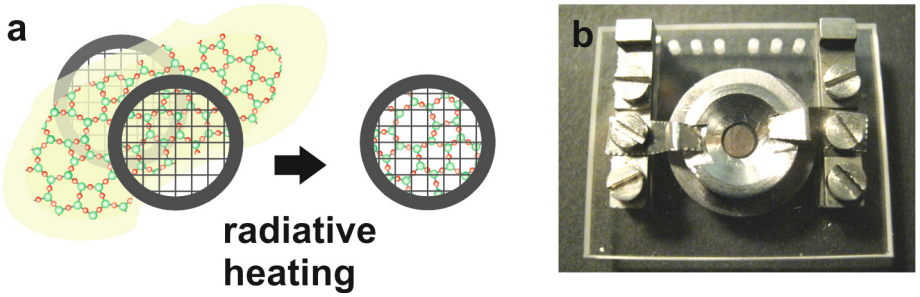

Figure 4.10: a) Schematic of transferring a PMMA-supported silica bilayer to a TEM grid. b) Photo of the two aligned TEM-grids in a sapphire sample holder, custom designed for UHV setup used in this study.

Since PMMA is used frequently as transfer medium for 2D materials, various protocols have been developed to remove it. Initially, PMMA was removed with a gentle flow of organic solvent,[117, 127] however, during the drying of liquid solvents, strong meniscus forces act upon the 2D material, exerting significant mechanical stress.[30] Furthermore, this approach often leaves problematic PMMA residues. In the case of graphene for example, the electron mobility is severely impaired by residual PMMA.[122] In the context of this work, complete removal of PMMA is a requirement for sample analysis. Figure 4.11a shows a TEM grid with visible residues of PMMA. For comparison, Figure 4.11b shows a clean TEM grid without residue. As we use electron-based techniques for identification of the transferred films, non-conductive PMMA-residues lead to charging effects on the sample. This results in both irreproducible measurements and electron-induced decomposi-

tion of PMMA. An example of this decomposition is shown in Figure 4.11c. The organic residue appears charred.

As an alternative to removing PMMA with solvents, thermal treatments can be utilized to develop improved cleaning procedures. PMMA can be annealed in air, vacuum, or in a reducing environment, such as H_2/Ar.[122] Depending on processing conditions, PMMA is expected to evaporate or to decompose, in certain cases catalyzed by the substrate material. During such a heat treatment, the transferred 2D material is exposed to a certain thermal load, which limits the applicability of this method. We decided to use a heat treatment to remove PMMA, as the silica bilayer is expected to withstand the temperature needed to evaporate PMMA.

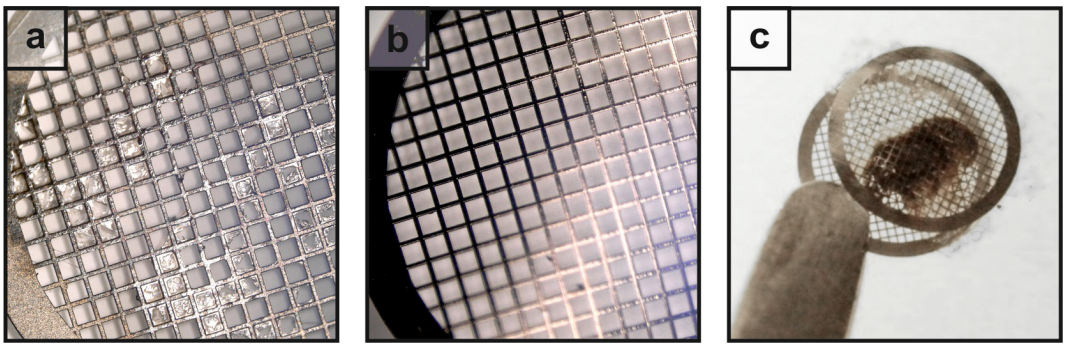

Figure 4.11: Photographs of TEM grids. a) Photograph showing PMMA residue. b) Photograph showing clean grid. c) Residual PMMA decomposes when exposed to an electron beam, leaving charred samples.

The influence of electrons on PMMA has been shown in Figure 4.11c. Hence, heating based on electron bombardment, as used for the preparation of the SiO_2-film on Ru(0001), cannot be employed here. Instead, we tested radiation and conduction based heating setups in order to remove the polymer. The stack of the silica bilayer between two TEM grids was held in place by custom made metal disks with appropriate diameter cutouts. The entire stack was mounted on a sapphire crystal, shown in Figure 4.10b, enabling us to load the samples into the sample clasp in our UHV setup. This sample was brought into close vicinity of a glowing filament to facilitate radiative heating in UHV. PMMA evaporation led to sharp increases in the chamber pressure. A return of

the pressure to the baseline indicated complete removal, after approximately 3 hours. In an optical microscope, the absence of PMMA residue can be ascertained; this should resemble the clean grid shown in Figure 4.11b.

Alternatively, the heat treatment can be delivered by placing the sample holder on a standard heating plate in air. It should be noted, that in the custom built TEM-grid holder, shown in Figure 4.10b, the area of contact of the grids with the bulk of the holder is very small, as the TEM grids provide only a narrow rim which can be used for mounting the grids. The time required for successful PMMA evaporation may therefore vary strongly, depending on how effectively the stack of TEM grids and silica/PMMA are mounted. Complete removal of PMMA can again be determined using an optical microscope. The grids should exhibit no visible residue, as shown in Figure 4.11b.

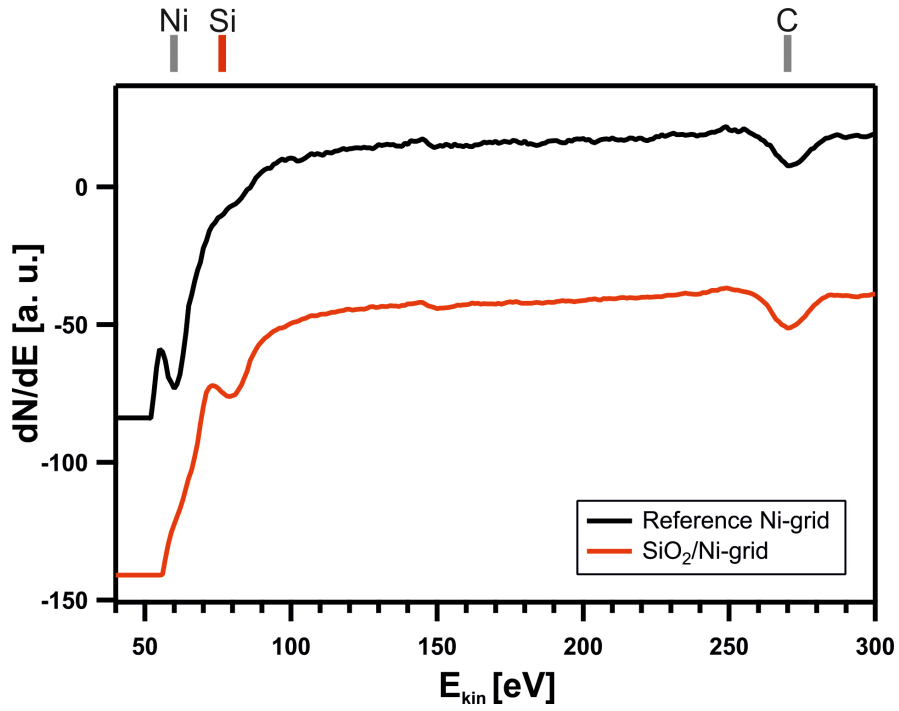

Figure 4.12: AES measurements on TEM grids. The black curve shows a reference spectrum on plain grids. The red curve shows a spectrum on grids that were stacked with SiO_2(PMMA) and exposed to a heat treatment.

Mounting the TEM grids in the sample holder shown in Figure 4.10b enables performing element sensitive Auger electron spectroscopy (AES) in the existing UHV setup. This measurement serves as a first indication for the success-

ful transfer of the 2D silica to the TEM grid. Figure 4.12 presents the AES characterization of the transferred silica film. The black curve shows a reference measurement that was taken on the empty TEM grid for comparison. A peak at 60 eV indicates nickel, the main material that the grids are made of. It must also be noted that the grids already contain a substantial amount of carbon (broad peak at 270 eV) in their unused state.

The red curve in Figure 4.12 shows the AES measurement of the stack of TEM grids and SiO_2/PMMA after a heat treatment and complete removal of PMMA. A peak at 79 eV indicates the presence of Si on the sample, partially obscuring the signature of Ni at 60 eV.

We subsequently investigated the TEM grid using a transmission electron microscope. For these measurements, the stack of TEM grids was unmounted from the UHV-holder shown in Figure 4.10b. Each TEM grid was imaged separately, and similar features were found in each one. Two typical images of silica on TEM grids are shown in Figure 4.13.

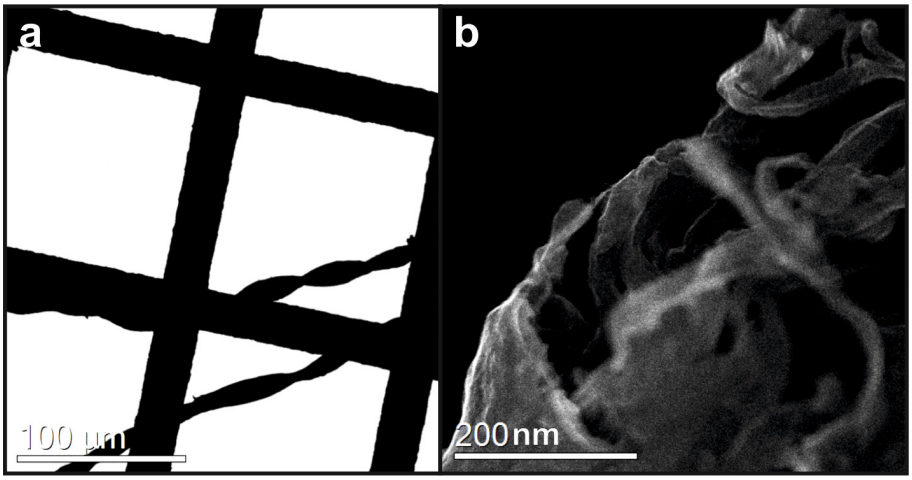

Figure 4.13: Transmission electron microscopy images of silica on TEM grids. a) Overview bright-field image, showing twisted micro-ribbons, recorded with with accelerating voltage V_A = 200 kV. b) High resolution secondary electron image, recorded in STEM mode with V_A = 200 kV, showing rolled up thin film.

Figure 4.13a shows a bright-field overview image. Twisted ribbons are shown, which are several 100 µm long and 10-20 µm in diameter. Figure 4.13b pre-

sents a secondary electron image with higher magnification, recorded in scanning transmission electron (STEM) mode. It shows the tip of a micro-ribbon at higher magnification, revealing a thin sheet in a coiled up shape. These micro-ribbons were found on both TEM grids, but concentrated in a few positions. It was also observed during changing sample position, that the ribbons were able to shift slightly, indicating that they were not bound strongly to the grid. From this it may be concluded, that directly after the PMMA removal, there were significantly higher amounts of SiO_2 supported on the TEM grids, which simply fell off while transferring the sample in and out of UHV, AES measurements, and preparing the grids for TEM imaging.

The setup used for TEM imaging is capable of recording electron energy loss spectra (EELS) as well. To this end, the electron energy after interaction with the sample is recorded, and the energy loss relative to the primary energy is determined. This measurement was performed on the silica micro-ribbons that were shown in the TEM images in Figure 4.13. Two energy regions are plotted in Figure 4.14, which are characteristic for the Si L edge (2s and 2p orbitals) and the O K edge (1s orbital).[128]

Figure 4.14a shows the energy region for electron excitation from the Si L shell. The onset of the absorption edge is marked in with a blue arrow. Its position is shifted several eV with respect to elementary silicon, and in good agreement with typical spectra for the Si^{4+} oxidation state found in amorphous SiO_2.[129–132] Figure 4.14b shows the spectrum for excitation of electrons from the O K shell. The position of the absorption edge is marked with a blue arrow and corresponds well with measurements reported on amorphous SiO_2.[133] Hence, EELS measurements confirm that the electronic structure of the observed micro-ribbons is equivalent to SiO_2.

The observed structures indicate a rolled-up shape for the silica bilayer. Such a change from the flat 2D morphology may occur during different steps in the sample preparation. It is possible that the heat treatment causes the PMMA layer to deform, and the silica sheet conforms to this morphological change. This may be prevented by removing the PMMA in a different way, such as

solvation or through a reducing gas phase. If a liquid solvent must be used to remove PMMA, critical point drying may be employed to prevent damage by meniscus forces.[31]

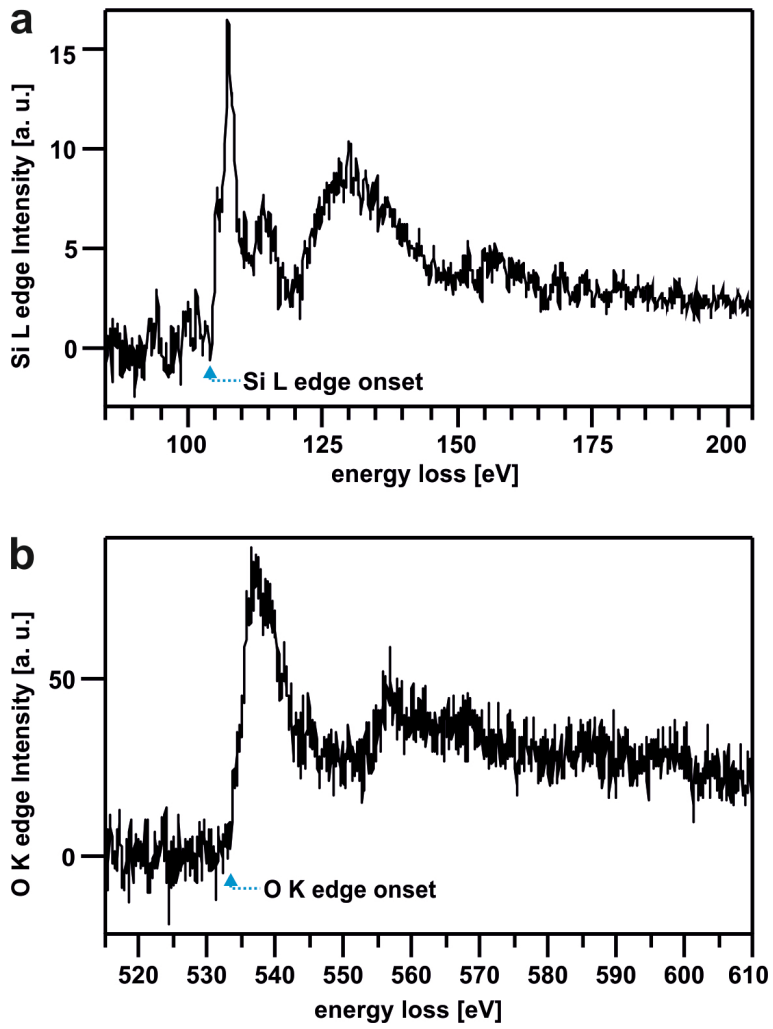

Figure 4.14: EELS spectra of silica bilayer supported on TEM grid. a) Si L edge loss spectrum. b) O K edge loss spectrum.

Damaging effects through an electron beam, either during the AES measurements or the TEM measurements, cannot be excluded. This damage may have caused local detachment, which has been observed to induce deformation in suspended graphene sheets.[31]

A probable assumption is that the chosen TEM grid was not providing sufficient support for the silica film, since the width of 'open space' between rods of the grid is roughly 100 µm. As a consequence, only portions of the film

which were rolled up, and presumably stiffer, remained on the grid while other, less stable morphologies were lost. A TEM grid with a smaller mesh size should be chosen for future experiments to enhance the likelihood of creating a freestanding silica membrane. An example would be so-called holey carbon grids. These are typically based on regular metal grids like the one used in this study. Additionally, a carbon film of several nm thickness is prepared to cover the TEM grid. The carbon film itself provides significantly smaller holes (with diameters of a few µm) and hole spacings than the TEM grid. Such grids are routinely used for supporting single layer graphene.[134] It is expected that a silica bilayer may also assume a flat morphology when supported in this way.

In summary, the exfoliated silica bilayer was successfully transferred to a TEM grid and analyzed with element-specific techniques and microscopy. In this experiment, the film unexpectedly formed micro-ribbon shapes, which has been discussed in the context of preparation procedure and substrate choice. Further experiments with varying these parameters may yield a flat, freestanding silica bilayer supported on a TEM grid.

4.3 Transfer of a silica bilayer to a Pt(111) support

In order to employ the 2D silica film in a variety of technical applications, it is necessary to place the material on the appropriate support. Depending on the intended use, this can be metal surfaces, polymers or stacks of other 2D materials, which may exhibit varying degrees of stability. The initial preparation of the 2D silica film, however, requires UHV conditions and high temperatures, as described in Section 2.2. Therefore, a post-growth transfer is the best option to deposit a silica bilayer on a sensitive substrate. One successful method to exfoliate a 2D silica sheet from its growth substrate has been demonstrated in Section 4.1. In order to provide evidence for the transferabil-

ity of 2D SiO_2, we placed the exfoliated bilayer on a new substrate and analyzed the transferred film.

Figure 4.15 schematically shows the complete transfer of a silica bilayer from the growth substrate to a new substrate. As a proof of concept, we selected platinum as target substrate for the silica film. It is expected to be a suitable support for the transferred 2D sheet, as Pt(111) crystals have been successfully used as growth substrates to prepare well defined silica bilayers.[40] A silica bilayer was exfoliated from Ru(0001), according to panels a-c in Figure 4.15. A detailed analysis of the plain Ru(0001) and the PMMA-supported SiO_2 bilayer is found in Section 4.1.

A Pt(111) crystal was cleaned by cycles of Ar bombardment and annealing. In order to provide a well-defined surface termination, prior to transferring the sample to ambient pressure, an oxygen coverage was prepared by annealing the crystal to 1203 K in 2×10^{-6} mbar O_2 for 5 minutes. By cooling the sample in oxygen partial pressure, a 3O(2×2) coverage is obtained. Subsequently, the sample was transferred from UHV to air.

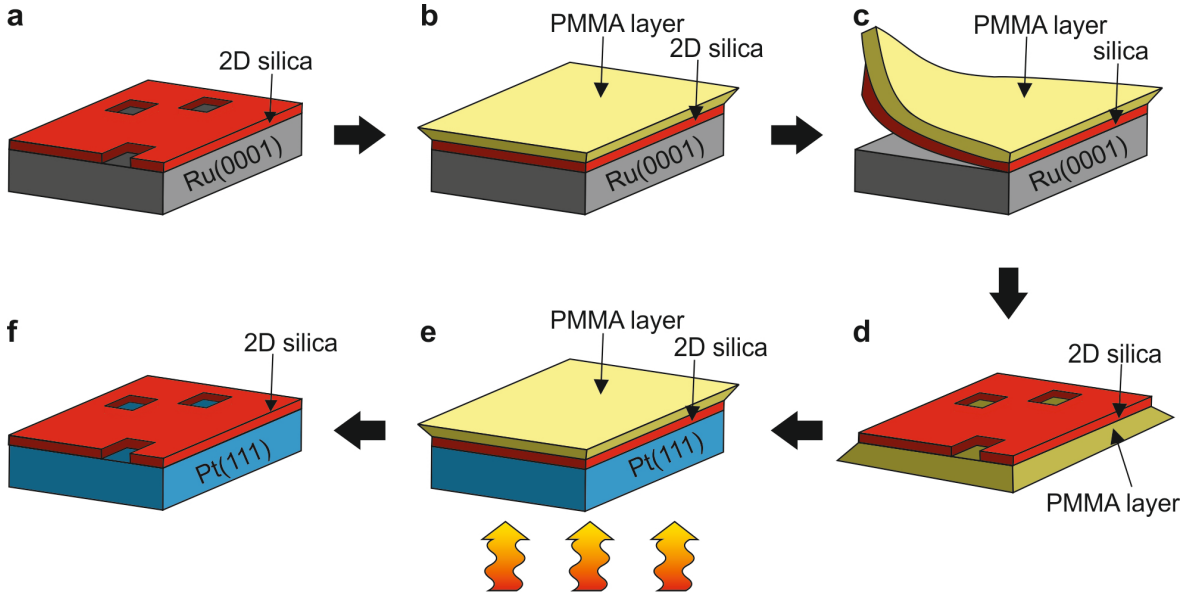

Figure 4.15: Schematic for transfer of silica film. a) A silica bilayer is supported on Ru(0001). b) After spin coating with PMMA. c) Mechanical exfoliation of PMMA. d) Silica bilayer is supported on PMMA. e) Stack of silica on PMMA is placed on Pt(111), heat treatment for removal of PMMA. f) Silica bilayer on Pt(111)

We placed the PMMA-supported silica bilayer (see Figure 4.15d) on the Pt(111) crystal, while enhancing the adhesion of the polymer flake to the new substrate with a few drops of acetone. A heat treatment was used to evaporate the PMMA (Figure 4.15e). This can be conveniently achieved by placing the sample on a standard laboratory-grade hot plate and heating it to 573 K for 3 hours. It should be noted that metallic platinum has previously been observed to catalyze the decomposition of PMMA,[123] however, we expect the catalytic activity of a smooth single crystal surface to be negligible. The silica bilayer was ultimately supported on the Pt(111) single crystal (Figure 4.15f). In order to analyze it, the sample was then transferred into the UHV chamber using an air lock.

The SiO_2/Pt(111) sample can be studied using the same techniques as for the initial characterization of SiO_2/Ru(0001). After transferring the sample from ambient conditions to UHV, a short heating step is useful to remove loosely bound surface adsorbates which would otherwise interfere with LEED, AES and STM. To this end, the sample was heated to 1130 K for 5 minutes in 2×10^{-6} mbar oxygen.

The results from the subsequent sample characterization are shown in Figure 4.16, including corresponding measurements on the clean Pt(111) sample. The plain crystal shows a hexagonal LEED pattern (Figure 4.16c). After the transfer, the LEED pattern shows a characteristic ring feature (panel d). This feature indicates a material that possesses short range order without long range order. This pattern is typical for the silica bilayer, which is comprised of rigid building blocks that are connected without directional order or periodicity. The overall amorphous structure indicated by the LEED pattern allows us to exclude the possibility of significant material loss during the transfer procedure. If a loss of material had occurred, we would either observe significantly lower surface coverage, or the formation of a monolayer instead of a bilayer, provided that the heating steps allow such reconstruction. We observe the same LEED pattern on different positions of the sample surface, indicating even coverage. We also exclude the presence of a monolayer, as silica mono-

layers have only been observed to grow with crystalline morphologies.[35, 36, 41] The amorphous signature of a ring feature in LEED is therefore taken as an indication of a bilayer.

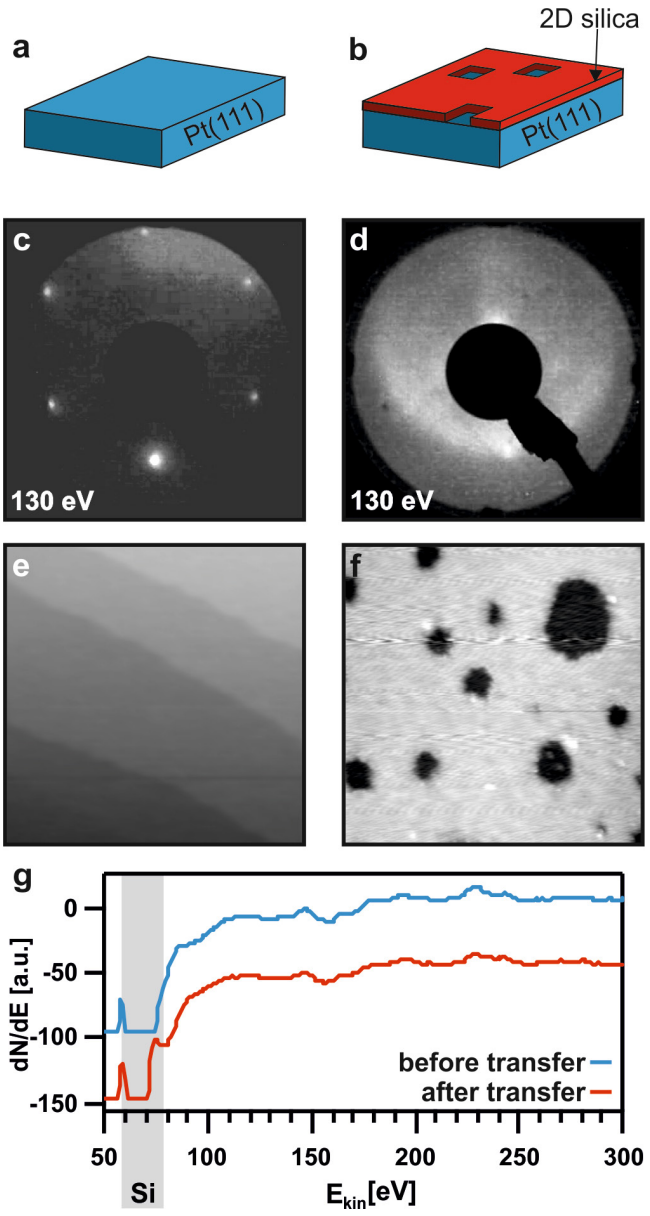

Figure 4.16: PMMA-assisted transfer of a silica bilayer to Pt(111). a) plain Pt(111), c) corresponding LEED, e) corresponding STM, V_S = 0.5 V, I_T = 50 pA, 50 nm × 50 nm. b) Silica bilayer on Pt(111), d) corresponding LEED, f) corresponding STM, V_S = 1 V, I_T = 100 pA, 50 nm × 50 nm. g) AES spectra of Pt(111) before and after transfer of the silica bilayer.

Figure 4.16e shows a typical STM image taken on the clean Pt(111) crystal. It reveals atomic step edges and clean terraces. Panel f shows a typical STM of

the sample after transfer of a silica bilayer sheet. It shows a flat film with open patches that expose the underlying metal. No wrinkles, cracks or tears were found in STM. In the bottom of Figure 4.16, panel g shows AES spectra of the plain Pt(111) crystal (blue curve) and of SiO_2/Pt(111) (red curve). The blue curve shows only features typical for platinum, the most prominent being the sharp peak at 61 eV. After the transfer, an additional feature is observed in the AES spectrum. The peak at 78 eV is assigned to silicon. With symmetry related information from LEED, morphology from STM and chemical identification from AES, we can conclude successful transfer of the silica bilayer from a ruthenium substrate to a platinum substrate.

The silica preparation shown in Figure 4.16 is the same one which was exfoliated from ruthenium, described in Figure 4.7. The overall morphology of the 2D silica film before and after the transfer is shown in direct comparison in Figure 4.17. Both STM images show smooth films covering the metal substrates, with comparable amounts and sizes of holes.

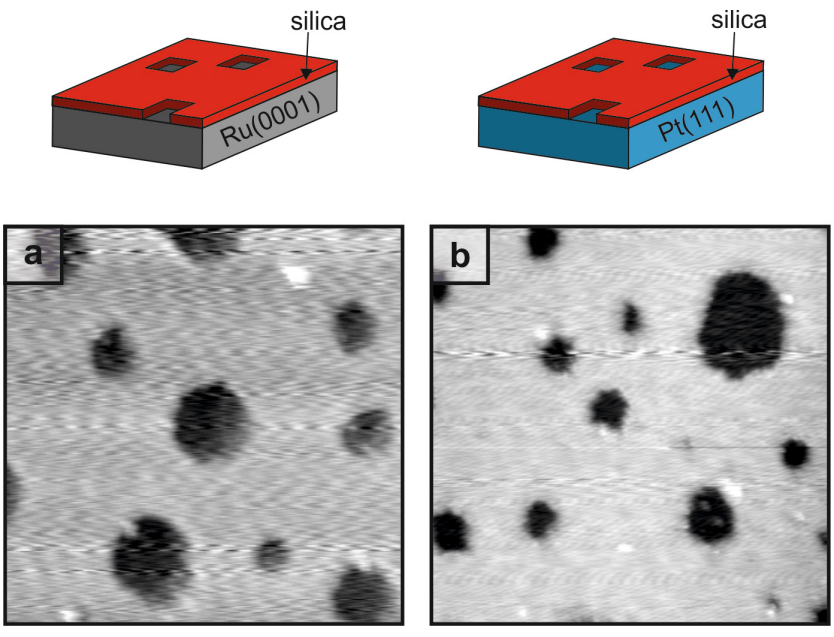

Figure 4.17: Comparing the morphology of the silica bilayer before and after the transfer procedure. a) STM of SiO_2/Ru(0001), V_S = 1 V, I_T = 50 pA, 50 nm × 50 nm. b) STM of SiO_2/Pt(111), V_S = 1 V, I_T = 100 pA, 50 nm × 50 nm.

Several STM images taken before and after the transfer were analyzed for their coverage according to the method illustrated in Figure 2.6. The coverage of the freshly prepared silica film on ruthenium was 1.6 ± 0.1 ML. The coverage of the transferred silica film on platinum was also 1.6 ± 0.1 ML. This comparison indicates that the 2D sheet was transferred under complete retention of the morphology with negligible loss of material in the process.

While the measurement in UHV conditions at low temperatures allows for highly stable STM imaging, it limits the size of surface area that can be imaged. An important benchmark in 2D materials transfer techniques, however, is how large of an area can be transferred dependably.[108, 110] In order to obtain a more comprehensive overview of the sample surface, we imaged the 2D silica film on platinum using an environmental scanning electron microscope (ESEM). This microscope contains a heating stage and a custom-built gas-feeding system, which allows imaging under controlled atmosphere.[52] The electron beam used for imaging is known to induce carbon contaminations of the sample surface, which is mitigated by imaging the sample at 573 K in 0.2 mbar oxygen. The ESEM allows imaging over a large range of magnifications, from mm to µm scale.

Figure 4.18 shows the 2D silica film on a Pt(111) support at different length scales. Panel a is a photograph of the sample, mounted on the typical sapphire holder used for our UHV setup. The diameter of the round single crystal slab is 9.2 mm. Figure 4.18b shows an ESEM image of 500 µm × 500 µm, and panel c contains an ESEM image of 500 nm × 500 nm. The contrast in both ESEM images has been inverted to allow direct comparison with the STM image. Both images verify that the sample surface is covered with a smooth layer that does not exhibit visible cracks, wrinkles or tears. Round hole-like features are observed consistently on the surface. These are assigned to the open patches which result from a sub-bilayer coverage on the metal. The highest resolution in ESEM, shown in Figure 4.18c, reveals holes of 20-30 nm in diameter. The STM of the same sample, shown in panel d, reveals features simi-

lar in size. Furthermore, the higher resolution of STM allows us to resolve holes smaller than 10 nm in diameter, as well.

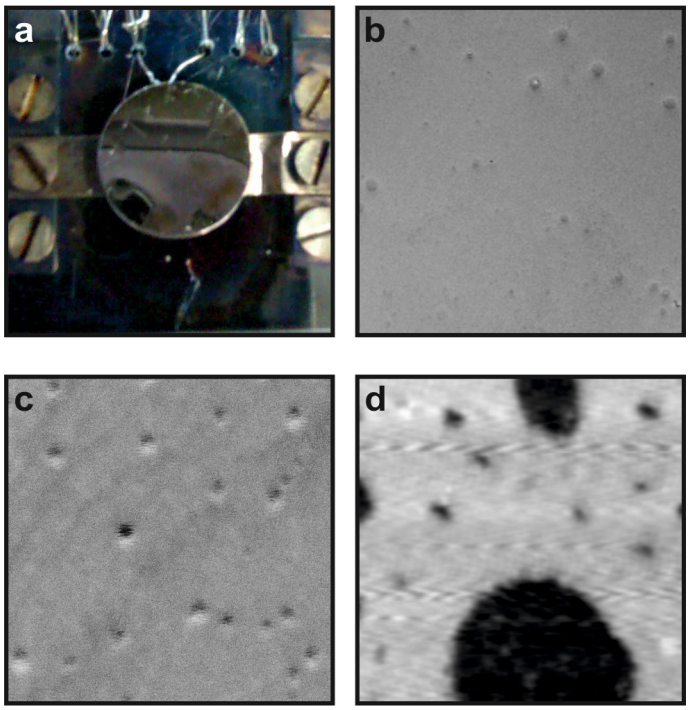

Figure 4.18: Transferred silica bilayer on Pt(111) at different length scales. a) Photo of platinum single crystal mounted on sapphire holder. The crystal slab has a diameter of 9.2 mm. b) ESEM of silica bilayer, V_A = 7.5 kV, 500 µm × 500 µm, contrast inverted. c) ESEM of silica bilayer, V_A = 12.5 kV, 500 nm × 500 nm, contrast inverted. d) STM of silica bilayer, V_S = 0.5 V, I_T = 100 pA, 50 nm × 50 nm.

The ESEM images show that the silica film was transferred from its ruthenium growth substrate to a platinum substrate at a large scale. The only features that were found in ESEM to interrupt the smooth 2D layer were morphological defects from the substrate, such as macroscopic scratches or holes that result from spot welding.

It should be noted that the choice of Pt(111) for this transfer was most likely an ideal one, which facilitated optimal transfer. A platinum single crystal provides atomically flat terraces, which are perfectly suited to support the atomically flat silica film. Furthermore, this crystal facet has been successfully employed for silica bilayer preparations in the past. Some deviation from the perfectly smooth structures may be expected for transfers

to other substrates, such as buckling effects on significantly rougher substrates. However, phenomena that are related to crystallographic mismatch, such as moire patterns, rippling as seen in graphene or nanomesh structures as found in h-BN monolayers are not expected when an amorphous silica sheet is combined with a 2D crystal.[135–137]

In addition to the suitability of the substrate, the success of this transfer indicates a very high stability of the silica film. During the exfoliation and the transfer procedure, considerable mechanical stress in the form of bending and stretching forces likely acted on the thin film. Nonetheless, large-scale ESEM images did not show signs of typical transfer damage. This resilience was recently predicted in DFT calculations, which suggested that strain-engineering might even be a way of tuning the band gap.[37] The perfect retention of morphology and surface coverage is in line with the observed ability of glass to tolerate increasingly smaller bending radii with decreasing material thickness.[138]

In conclusion, a silica bilayer was exfoliated from its growth substrate and transferred to a foreign target substrate while retaining its structure perfectly. This proof-of-concept has paved the way for designing heteroarchitectures including this atomically defined silica film, in order to utilize its properties.

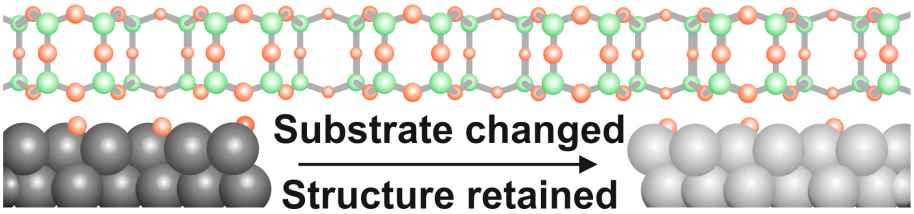

Figure 4.19: Schematic indicating the ability of an atomically defined silica bilayer to be transferred from its growth substrate to a different substrate under retention of its structure.

5. Conclusion and outlook

This dissertation has explored important aspects in the applicability of a recently discovered bilayer SiO_2-structure as a new class of 2D material. Properties facilitating technological applications of the silica bilayer as a 2D material were investigated in the first part of this project. Two main objectives were considered in this characterization. On the one hand, structural properties were described that are promising for particular uses of this system in 2D applications. On the other hand, the suitability of this system for transferring the 2D layer from a growth substrate to a target substrate was successfully demonstrated.

The atomically flat silica sheet exhibits crystalline and amorphous regions. The crystalline form has a hexagonal symmetry with 5.42 Å periodicity. We have conducted a topology study of the amorphous region, characterizing the ring sizes in this network and investigating how they arrange into larger clusters. In this work it was observed that the medium-range arrangement of building blocks is governed by geometric factors and does not happen randomly. A parameter capturing the bond angle deformation was found to correlate with building block occurrence probabilities. This improved understanding of the silica ring network is the basis for utilizing the unique amorphous structure in a technological application of 2D silica. It can also be helpful in shedding light on the nature of the glass state, a topic which is under investigation by many theoretical and experimental groups around the world.

The overall material properties are influenced by the network of different ring sizes, as shown in adsorption studies of metal atoms on the mixed domain film. Pd and Au atoms show selective adsorption behavior, based on different ring sizes available in crystalline domains, domain boundaries and amorphous domains of the film. The selective adsorption behavior can be utilized for gas separation where different species in a mixture have different sizes. Here the different ring sizes may be used to discriminate between different intercalating species. Furthermore, intercalation of reactive species and subsequent

preparation of a foreign 2D layer underneath a silica sheet may be a way for designing van der Waals solids.

As a preliminary study for the transfer of the 2D silica sheet, we investigated the stability of the film against solvents. By exposing the ruthenium-supported silica bilayer to water, ethanol and acetone, respectively, we determined the stability of the system against these environments. After each solvent treatment, the material retained its characteristic LEED pattern and Si spectroscopic signature in AES. These findings profoundly highlight the stability of this structure.

Furthermore, we conducted liquid-AFM measurements of a silica bilayer immersed in water. We were able to show that its structure is retained perfectly inside a liquid environment. This is verified statistically by analyzing coverage related indicators. Further studies have corroborated that ultrathin silica is very unreactive, much like its bulk counterpart. Hence, the 2D membrane may be used as a protective coating layer for sensitive surfaces.

Having established the stability of this silica system, we developed a method to transfer the film from its growth substrate to a target substrate while retaining its structure. Different approaches exist in 2D materials research to achieve this goal. The silica bilayer is bound to the substrate with van der Waals forces, which are strong enough to withstand the widely-known Scotch-tape method. Mechanical exfoliation using a PMMA ‘handle’ can remove the silica layer from its substrate. Analysis of the plain substrate after exfoliation indicates that the entire silica sheet is lifted off the surface as a continuous sheet.

The exfoliated silica bilayer can subsequently be transferred to different supports, depending on the desired application. For this proof of concept, a TEM grid and a platinum metal single crystal have been utilized as new substrates. PMMA flakes carrying a silica bilayer were placed between two TEM grids made from nickel. The PMMA was removed using a heating regimen. AES was used to establish the presence of Si on the grids. TEM imaging revealed that

the silica sheet had curled up into micro-ribbons that were concentrated in few areas of the grids. Further experiments using TEM grids with smaller grid spacings and a modified heating procedure, may yield a flat, freely suspended silica bilayer in the future.

A PMMA-supported silica bilayer was transferred on a Pt(111) single crystal. After removal of the PMMA, analysis using LEED, AES, STM and ESEM revealed an atomically flat, transferred film at mm-scale without typical transfer damage, such as tears and wrinkles. The surface coverage stayed the same throughout the transfer.

These successful transfer experiments have opened up the possibility for using an SiO_2 bilayer as a two-dimensional material. The presented techniques for exfoliating and transferring an ultrathin, atomically flat silica sheet may be employed for creating stacks of several silica films or combined devices using other 2D materials, such as graphene.

In order to create larger exfoliated films without open patches, the preparation of silica bilayer films may be modified, especially the chosen growth substrate, to allow a larger variety of exfoliation methods. Further studies regarding the transfer of bilayers are expected to ultimately yield freestanding flat silica films, perhaps supported on TEM grids. Studying the silica bilayer sheet on different substrates and in its freestanding form, will be key to discover the inherent properties of this new 2D material. Such an arrangement will also allow the experimental verification of the predicted wide band gap for this material.

In summary, an atomically flat silica bilayer has been successfully isolated from its substrate and transferred to a foreign substrate, thereby adding this structure to the library of 2D materials. This addition represents the first fully saturated 2D oxide, the first 2D material exhibiting an amorphous lateral structure, and the 2D dielectric offering the widest band gap at this point.

6. Appendix

6.1 List of abbreviations and frequently used symbols

2D	two-dimensional
3D	three-dimensional
AES	Auger electron spectroscopy
AFM	atomic force microscopy
B_S	sample bias
CVD	chemical vapor deposition
EELS	electron energy loss spectroscopy
ESEM	environmental electron scanning microscopy
FM-DFM	frequency modulation dynamic force microscopy
h-BN	hexagonal boron nitride
HOPG	highly oriented pyrolytic graphite
I_T	tunneling current
LEED	low energy electron spectroscopy
ML	monolayer
nc-AFM	noncontact atomic force microscopy
NMR	nuclear magnetic resonance
PMMA	Poly(methyl methacrylate)

PVD	physical vapor deposition
SEM	scanning electron microscopy
SiO_2	silicon dioxide
SPM	scanning probe microscopy
STM	scanning tunneling microscopy
TEM	transmission electron microscopy
UHV	ultra-high vacuum
V_A	accelerating voltage
XPS	X-ray photoelectron spectroscopy

6.2 Bibliography

[1] M. S. Dresselhaus, A revolution of nanoscale dimensions, *Nat. Rev. Mater.*, **2016**, 1, January, 1–2.

[2] H. P. Boehm, A. Clauss, G. O. Fischer, and U. Hofmann, Das Adsorptionsverhalten sehr dünner Kohlenstoff-Folien, *Zeitschrift für Anorg. und Allg. Chemie*, **1962**, 316, 119–127.

[3] K. S. Novoselov, D. Jiang, F. Schedin, T. J. Booth, V. V Khotkevich, S. V. Morozov, and A. K. Geim, Two-dimensional atomic crystals, *Proc. Natl. Acad. Sci. USA*, **2005**, 102, 30, 10451–10453.

[4] N. R. Gall, E. V. Rut'kov, and A. Y. Tontegode, TWO DIMENSIONAL GRAPHITE FILMS ON METALS AND THEIR INTERCALATION, *Int. J. Mod. Phys. B*, **1997**, 11, 16, 1865–1911.

[5] Y. Pan, L. Zhang, L. Huang, L. Li, L. Meng, M. Gao, Q. Huan, X. Lin, Y. Wang, S. Du, H. J. Freund, and H. J. Gao, Construction of 2D atomic crystals on transition metal surfaces: Graphene, silicene, and hafnene, *Small*, **2014**, 10, 11, 2215–2225.

[6] M. Xu, T. Liang, M. Shi, and H. Chen, Graphene-Like Two-Dimensional Materials, *Chem. Rev.*, **2013**, 113, 3766–3798.

[7] J. Hu, Z. Guo, P. E. Mcwilliams, J. E. Darges, D. L. Druffel, A. M. Moran, and S. C. Warren, Band Gap Engineering in a 2D Material for Solar-to-Chemical Energy Conversion, *Nano Lett.*, **2015**, 16, 74–79.

[8] S. Z. Butler, S. M. Hollen, L. Cao, Y. Cui, J. A. Gupta, H. R. Gutiérrez, T. F. Heinz, S. S. Hong, J. Huang, A. F. Ismach, E. Johnston-Halperin, M. Kuno, V. V Plashnitsa, R. D. Robinson, R. S. Ruoff, S. Salahuddin, J. Shan, L. Shi, M. G. Spencer, M. Terrones, W. Windl, and J. E. Goldberger, Progress, challenges, and opportunities in two-dimensional materials beyond graphene, *ACS Nano*, **2013**, 7, 4, 2898–2926.

[9] A. K. Geim and I. V Grigorieva, Van der Waals heterostructures, *Nature*, **2013**, 499, 419–25.

[10] J. W. May, Platinum Surface LEED Rings, *Surf. Sci.*, **1969**, 17, 267–270.

[11] A. M. Shikin, D. Farías, and K. H. Rieder, Phonon stiffening induced by copper intercalation in monolayer graphite on Ni(111), *Europhys. Lett.*, **1998**, 44, 1, 44–49.

[12] A. Nagashima, N. Tejima, and C. Oshima, Electronic states of the pristine and alkali-metal-intercalated monolayer graphite/Ni(111) systems, *Phys. Rev. B*, **1994**, 50, 23, 17487–17495.

[13] A. Y. Tontegode, Carbon on transition metal surfaces, *Prog. Surf. Sci.*, **1991**, 38, 201–429.

[14] C. Lee, X. Wei, J. W. Kysar, and J. Hone, Measurement of the Elastic Properties and Intrinsic Strength of Monolayer Graphene, *Science*, **2008**, 321, 385–388.

[15] "Class for Physics of the Royal Swedish Academy of Sciences", Scientific Background on the Nobel Prize in Physics 2010 GRAPHENE compiled, *The Royal Swedish Academy of Sciences*, 50005, October, 2010, 0–10.

[16] A. C. Ferrari, F. Bonaccorso, V. Falko, K. S. Novoselov, S. Roche, P. Bøggild, S. Borini, F. Koppens, V. Palermo, N. Pugno, J. A. Garrido, R. Sordan, A. Bianco, L. Ballerini, M. Prato, E. Lidorikis, J. Kivioja, C. Marinelli, T. Ryhänen, A. Morpurgo, J. N. Coleman, V. Nicolosi, L. Colombo, A. Fert, M. Garcia-Hernandez, A. Bachtold, G. F. Schneider, F. Guinea, C. Dekker, M. Barbone, C. Galiotis, A. Grigorenko, G. Konstantatos, A. Kis, M. Katsnelson, C. W. J. Beenakker, L. Vandersypen, A. Loiseau, V. Morandi, D. Neumaier, E. Treossi, V. Pellegrini, M. Polini, A. Tredicucci, G. M. Williams, B. H. Hong, J. H. Ahn, J. M. Kim, H. Zirath, B. J. van Wees, H. van der Zant, L. Occhipinti, A. Di Matteo, I. A. Kinloch, T. Seyller, E. Quesnel, X. Feng, K. Teo, N. Rupesinghe, P. Hakonen, S. R. T. Neil, Q. Tannock, T. Löfwander, and J. Kinaret, Science and technology roadmap for graphene, related two-dimensional crystals, and hybrid systems, *Nanoscale*, **2015**, 7, 11, 4598–4810.

[17] U. of Cambridge, First graphene-based flexible display produced, 2014. [Online]. Available: http://www.cam.ac.uk/research/news/first-graphene-based-flexible-display-produced. [Accessed: 23-Feb-2016].

[18] Y. J. Chabal, Fundamental Aspects of Silicon Oxidation, 1st ed. Springer-Verlag Berlin Heidelberg, **2001**.

[19] C. R. Dean, A. F. Young, I. Meric, C. Lee, L. Wang, S. Sorgenfrei, K. Watanabe, T. Taniguchi, P. Kim, K. L. Shepard, and J. Hone, Boron nitride substrates for high-quality graphene electronics., *Nat. Nanotechnol.*, **2010**, 5, 10, 722–726.

[20] K. M. Burson, W. G. Cullen, S. Adam, C. R. Dean, K. Watanabe, T. Taniguchi, P. Kim, and M. S. Fuhrer, Direct imaging of charged impurity density in common graphene substrates, *Nano Lett.*, **2013**, 13, 3576–3580.

[21] A. N. Rudenko, F. J. Keil, M. I. Katsnelson, and A. I. Lichtenstein, Interfacial interactions between local defects in amorphous SiO2 and supported graphene, *Phys. Rev. B*, **2011**, 84, 1–9.

[22] M. Ishigami, J. H. Chen, W. G. Cullen, M. S. Fuhrer, and E. D. Williams, Atomic structure of graphene on SiO2, *Nano Lett.*, **2007**, 7, 6, 1643–1648.

[23] W. G. Cullen, M. Yamamoto, K. M. Burson, J. H. Chen, C. Jang, L. Li, M. S. Fuhrer, and E. D. Williams, High-Fidelity Conformation of Graphene to SiO2 Topographic Features, *Phys. Rev. Lett.*, **2010**, 105, 21, 215504 1–4.

[24] A. Pakdel, Y. Bando, and D. Golberg, Nano boron nitride flatland, *Chem. Soc. Rev.*, **2014**, 43, 3, 934–59.

[25] Z.-G. Chen, J. Zou, G. Liu, F. Li, Y. Wang, L. Wang, X.-L. Yuan, T. Sekiguchi, H.-M. Cheng, and G. Q. Lu, Novel Boron Nitride Hollow Nanoribbons, *ACS Nano*, **2008**, 2, 10, 2183–2191.

[26] K. Watanabe, T. Taniguchi, and H. Kanda, Direct-bandgap properties and evidence for ultraviolet lasing of hexagonal boron nitride single crystal, *Nat. Mater.*, **2004**, 3, 6, 404–409.

[27] K. K. Kim, A. Hsu, X. Jia, S. M. Kim, Y. Shi, M. Hofmann, D. Nezich, J. F. Rodriguez-Nieva, M. S. Dresselhaus, T. Palacios, and J. Kong, Synthesis of Monolayer Boron Nitride on Cu Foil Using Chemical Vapor Deposition, *Nano Lett.*, **2011**, 12, 161–166.

[28] M. S. Bresnehan, M. J. Hollander, M. Wetherington, M. Labella, K. A. Trumbull, R. Cavalero, D. W. Snyder, and J. A. Robinson, Integration of Hexagonal Boron Nitride High-Performance Devices, *ACS Nano*, **2012**, 6, 6, 5234–5241.

[29] A. K. Geim, Graphene: Status and Prospects, *Science*, **2009**, 324, 1530–1534.

[30] A. Castellanos-Gomez, V. Singh, H. S. J. Van Der Zant, and G. A. Steele, Mechanics of freely-suspended ultrathin layered materials, *Ann. Phys.*, **2015**, 527, 1–2, 27–44.

[31] J. C. Meyer, A. K. Geim, M. I. Katsnelson, K. S. Novoselov, T. J. Booth, and S. Roth, The structure of suspended graphene sheets, *Nature*, **2007**, 446, 1, 60–63.

[32] Y. Sakai, S. Saito, and M. L. Cohen, First-Principles Study on Graphene/Hexagonal Boron Nitride Heterostructures, *J. Phys. Soc. Japan*, **2015**, 84, 121002 1–11.

[33] D. Löffler, J. J. Uhlrich, M. Baron, B. Yang, X. Yu, L. Lichtenstein, L. Heinke, C. Büchner, M. Heyde, S. Shaikhutdinov, H.-J. Freund, R. Włodarczyk, M. Sierka, and J. Sauer, Growth and Structure of Crystalline Silica Sheet on Ru(0001), *Phys. Rev. Lett.*, **2010**, 105, 14,

146104 1–4.

[34] L. Lichtenstein, C. Büchner, B. Yang, S. Shaikhutdinov, M. Heyde, M. Sierka, R. Włodarczyk, J. Sauer, and H.-J. Freund, The Atomic Structure of a Metal-Supported Vitreous Thin Silica Film, *Angew. Chemie, Int. Ed.*, **2012**, 51, 2, 404–407.

[35] B. Yang, W. E. Kaden, X. Yu, J. A. Boscoboinik, Y. Martynova, L. Lichtenstein, M. Heyde, M. Sterrer, R. Włodarczyk, M. Sierka, J. Sauer, S. Shaikhutdinov, and H.-J. Freund, Thin silica films on Ru(0001): monolayer, bilayer and three-dimensional networks of [SiO4] tetrahedra, *Phys. Chem. Chem. Phys.*, **2012**, 14, 11344–11351.

[36] T. Schroeder, M. Adelt, B. Richter, M. Naschitzki, M. Bäumer, and H.-J. Freund, Epitaxial Growth of SiO2 on Mo(112), *Surf. Rev. Lett.*, **2000**, 7, 1 & 2, 7–14.

[37] E. Gao, B. Xie, and Z. Xu, Two-dimensional silica: Structural, mechanical properties, and strain-induced band gap tuning, *J. Appl. Phys.*, **2016**, 119, 1, 014301 1–7.

[38] A. M. Shikin, G. V. Prudnikova, V. K. Adamchuk, F. Moresco, and K. H. Rieder, Surface intercalation of gold underneath a graphite monolayer on Ni(111) studied by angle-resolved photoemission and high-resolution electron-energy-loss spectroscopy, *Phys. Rev. B*, **2000**, 62, 19, 13202–13208.

[39] E. I. Altman, J. Götzen, N. Samudrala, and U. D. Schwarz, Growth and Characterization of Crystalline Silica Films on Pd (100), *J. Phys. Chem. C*, **2013**, 117, 26144–26155.

[40] X. Yu, B. Yang, J. A. Boscoboinik, S. Shaikhutdinov, and H.-J. Freund, Support effects on the atomic structure of ultrathin silica films on metals, *Appl. Phys. Lett.*, **2012**, 100, 151608 1–4.

[41] F. Ben Romdhane, T. Björkman, J. A. Rodríguez-Manzo, O. Cretu, A. V Krasheninnikov, and F. Banhart, In situ growth of cellular two-dimensional silicon oxide on metal substrates., *ACS Nano*, **2013**, 7, 6, 5175–80.

[42] P. Y. Huang, S. Kurasch, A. Srivastava, V. Skakalova, J. Kotakoski, A. V. Krasheninnikov, R. Hovden, Q. Mao, J. C. Meyer, J. Smet, D. A. Muller, and U. Kaiser, Direct Imaging of a Two-Dimensional Silica Glass on Graphene, *Nano Lett.*, **2012**, 12, 1081–1086.

[43] N. Yoshimura, Vacuum Technology, 1st ed. Springer-Verlag Berlin Heidelberg, **2008**.

[44] S. Stuckenholz, Combining Scanning Probe Microscopy with

Temperature Programmed Desorption on Metal Supported MgO Thin Films, Technische Universität Berlin, **2016**.

[45] H.-J. Güntherodt and R. Wiesendanger, Scanning Tunneling Microscopy I, 2nd ed. Springer-Verlag Berlin Heidelberg, **1994**.

[46] N. Nilius, Properties of oxide thin films and their adsorption behavior studied by scanning tunneling microscopy and conductance spectroscopy, *Surf. Sci. Rep.*, **2009**, 64, 12, 595–659.

[47] S. Benedetti, H. M. Benia, N. Nilius, S. Valeri, and H. J. Freund, Morphology and optical properties of MgO thin films on Mo(0 0 1), *Chem. Phys. Lett.*, **2006**, 430, 4–6, 330–335.

[48] I. Soltani Bozchalooi, A. C. Houck, J. AlGhamdi, and K. Youcef-Toumi, Design and control of multi-actuated atomic force microscope for large-range and high-speed imaging, *Ultramicroscopy*, **2016**, 160, 213–224.

[49] K. Kobayashi, N. Oyabu, K. Kimura, S. Ido, K. Suzuki, T. Imai, K. Tagami, M. Tsukada, and H. Yamada, Visualization of hydration layers on muscovite mica in aqueous solution by frequency-modulation atomic force microscopy., *J. Chem. Phys.*, **2013**, 138, 184704 4–7.

[50] J. W. Niemantsverdriet, Spectroscopy in Catalysis, 3rd ed. Wiley-VCH Weinheim, **2007**.

[51] J. Thomas and T. Gemming, Analytical Transmission Electron Microscopy. Springer-Verlag Berlin Heidelberg, **2014**.

[52] Z. Wang, G. Weinberg, Q. Zhang, T. Lunkenbein, A. Klein-Hoffmann, M. Kurnatowska, M. Plodinec, Q. Li, L. Chi, R. Schloegl, and M.-G. Willinger, Direct Observation of Graphene Growth and Associated Copper Substrate Dynamics by In-Situ Scanning Electron Microscopy, *ACS Nano*, **2015**, 9, 2, 1506–1519.

[53] X. Huang, Z. J. Wang, G. Weinberg, X. M. Meng, and M. G. Willinger, In Situ Scanning Electron Microscopy Observation of Growth Kinetics and Catalyst Splitting in Vapor-Liquid-Solid Growth of Nanowires, *Adv. Funct. Mater.*, **2015**, 25, 37, 5979–5987.

[54] S. Hofmann, Auger- and X-Ray Photoelectron Spectroscopy in Materials Science, 1st ed., 49. Springer-Verlag Berlin Heidelberg, **2013**.

[55] S. Hofmann, Recent Progress in Quantitative and High Spatial Resolution AES, *Mikrochim. Acta*, **1994**, 114/115, 21–32.

[56] L. Lichtenstein, C. Büchner, B. Yang, S. Shaikhutdinov, M. Heyde, M. Sierka, R. Włodarczyk, J. Sauer, and H.-J. Freund, Die atomare Struktur eines metallgestützten glasartigen dünnen Silikafilms, *Angew. Chemie*,

2012, 124, 2, 416–420.

[57] L. Lichtenstein, The Structure of Two-Dimensional Vitreous Silica, Freie Universität Berlin, **2012**.

[58] I. Horcas, R. Fernández, J. M. Gómez-Rodríguez, J. Colchero, J. Gómez-Herrero, and A. M. Baro, WSXM: a software for scanning probe microscopy and a tool for nanotechnology., *Rev. Sci. Instrum.*, **2007**, 78, 013705 1–8.

[59] L. Lichtenstein, M. Heyde, and H.-J. Freund, Atomic Arrangement in Two-Dimensional Silica: From Crystalline to Vitreous Structures, *J. Phys. Chem. C*, **2012**, 116, 20426–20432.

[60] L. Lichtenstein, M. Heyde, and H.-J. Freund, Crystalline-Vitreous Interface in Two Dimensional Silica, *Phys. Rev. Lett.*, **2012**, 109, 10, 106101 1–5.

[61] E. I. Altman and U. D. Schwarz, Structural and Electronic Heterogeneity of Two Dimensional Amorphous Silica Layers, *Adv. Mater. Interfaces*, **2014**, 1, 1400108 1–5.

[62] M. Heyde, G. H. Simon, and L. Lichtenstein, Resolving oxide surfaces - From point and line defects to complex network structures, *Phys. Status Solidi B*, **2013**, 250, 5, 895–921.

[63] W. H. Zachariasen, The Atomic Arrangement in Glass, *J. Am. Chem. Soc.*, **1932**, 54, 10, 3841–3851.

[64] T. Nakamura, Y. Hirakoa, A. Hirata, E. G. Escolar, and Y. Nishiura, Persistent homology and many-body atomic structure for medium-range order in the glass, *Nanotechnology*, **2015**, 26, 304001.

[65] C. Büchner, L. Lichtenstein, and M. Heyde, Ein glasklares Modell, *Nachrichten aus der Chemie*, **2012**, 60, 9, 861–864.

[66] C. Büchner, L. Liu, S. Stuckenholz, K. M. Burson, L. Lichtenstein, M. Heyde, H.-J. Gao, and H.-J. Freund, Building block analysis of 2D amorphous networks reveals medium range correlation, *J. Non. Cryst. Solids*, **2016**, 435, 40–47.

[67] R. L. Mozzi and B. E. Warren, The Structure of Vitreous Silica, *J. Appl. Crystallogr.*, **1969**, 2, 164–172.

[68] S. K. Sharma, J. F. Mammone, and M. F. Nicol, Raman investigation of ring configurations in viterous silica, *Nature*, **1981**, 292, 140–141.

[69] S. Kostinski, R. Pandey, S. Gowtham, U. Pernisz, and A. Kostinski, Diffusion of Water Molecules in Amorphous Silica, *Electron Device*

Lett. IEEE, **2012**, 33, 6, 863–865.

[70] P. Hacarlioglu, D. Lee, G. V. Gibbs, and S. T. Oyama, Activation energies for permeation of He and H2 through silica membranes: An ab initio calculation study, *J. Memb. Sci.*, **2008**, 313, 277–283.

[71] D. Lee and S. T. Oyama, Gas permeation characteristics of a hydrogen selective supported silica membrane, *J. Memb. Sci.*, **2002**, 210, 2, 291–306.

[72] D. Lee, L. Zhang, S. T. Oyama, S. Niu, and R. F. Saraf, Synthesis, characterization, and gas permeation properties of a hydrogen permeable silica membrane supported on porous alumina, *J. Memb. Sci.*, **2004**, 231, 117–126.

[73] R. M. Barrer and D. E. W. Vaughan, Solution and Diffusion of Helium and Neon in Tridymite and Cristobalite, *Trans. Faraday Soc.*, **1967**, 63, 2275–2290.

[74] L. F. Gladden, T. A. Carpenter, and S. R. Elliott, 29Si MAS NMR studies of the spin-lattice relaxation time and bond-angle distribution in vitreous silica, *Philos. Mag. Part B*, **1986**, 53, 4, L81–L87.

[75] T. M. Clark, P. J. Grandinetti, P. Florian, and J. F. Stebbins, Correlated structural distributions in silica glass, *Phys. Rev. B*, **2004**, 70, 6, 1–8.

[76] J. V. Smith, Nuclear magnetic resonance of silica polymorphs, *Nature*, **1983**, 303, 223–225.

[77] L. Lichtenstein, C. Büchner, S. Stuckenholz, M. Heyde, and H.-J. Freund, Enhanced atomic corrugation in dynamic force microscopy—The role of repulsive forces, *Appl. Phys. Lett.*, **2012**, 100, 12, 123105 1–3.

[78] D. Weaire and N. Rivier, Soap , cells and statistics — random patterns in two dimensions, *Contemp. Phys.*, **1984**, 25, 1, 59–99.

[79] F. T. Lewis, A comparison between the mosaic of polygons in a film of artificial emulsion and the pattern of simple ephithelium in surface view (cucumber epidermis and human amnion), *Anat. Rec.*, **1931**, 50, 3, 235–265.

[80] S. Chiu, Aboav-Weaire's and Lewis' Laws - A Review, *Mater. Charact.*, **1995**, 34, 149–165.

[81] I. Zsoldos and A. Szasz, Appearance of collectivity in two-dimensional cellular structures, *Comput. Mater. Sci.*, **1999**, 15, 441–448.

[82] D. A. Aboav, The Arrangement of Cells in a Net. II, *Metallography*,

1983, 16, 265–273.

[83] D. A. Aboav, The Arrangement of Cells in a Net, *Metallography*, **1980**, 13, 1, 43–58.

[84] D. A. Aboav, The Arrangement of Cells in a Net. III, *Metallography*, **1984**, 17, 383–396.

[85] D. Cohen-Tanugi and J. C. Grossman, Water desalination across nanoporous graphene, *Nano Lett.*, **2012**, 12, 7, 3602–3608.

[86] D. Cohen-Tanugi, L. Lin, and C. Grossman, Multilayer Nanoporous Graphene Membranes for Water Desalination, *Nano Lett.*, **2016**, 16, 2, 1027–1033.

[87] Z. Yuan, X. Zhu, M. Li, W. Lu, X. Li, and H. Zhang, A Highly Ion-Selective Zeolite Flake Layer on Porous Membranes for Flow Battery Applications, *Angew. Chemie*, **2016**, 128, 9, 3110–3114.

[88] A. Varykhalov, J. Sánchez-Barriga, A. M. Shikin, C. Biswas, E. Vescovo, A. Rybkin, D. Marchenko, and O. Rader, Electronic and magnetic properties of quasifreestanding graphene on Ni, *Phys. Rev. Lett.*, **2008**, 101, 15, 1–4.

[89] S. Lizzit, R. Larciprete, P. Lacovig, M. Dalmiglio, F. Orlando, A. Baraldi, L. Gammelgaard, L. Barreto, M. Bianchi, E. Perkins, and P. Hofmann, Transfer-free electrical insulation of epitaxial graphene from its metal substrate, *Nano Lett.*, **2012**, 12, 9, 4503–4507.

[90] R. Larciprete, P. Lacovig, F. Orlando, M. Dalmiglio, L. Omiciuolo, A. Baraldi, and S. Lizzit, Chemical gating of epitaxial graphene through ultrathin oxide layers, *Nanoscale*, **2015**, 7, 29, 12650–12658.

[91] A. Dahal and M. Batzill, Growth from behind: Intercalation-growth of two-dimensional FeO moiré structure underneath of metal-supported graphene, *Sci. Rep.*, **2015**, 5, 11378 1–9.

[92] C. Büchner, L. Lichtenstein, S. Stuckenholz, M. Heyde, F. Ringleb, M. Sterrer, W. E. Kaden, L. Giordano, G. Pacchioni, and H. Freund, Adsorption of Au and Pd on Ruthenium-Supported Bilayer Silica, *J. Phys. Chem. C*, **2014**, 118, 20959–20969.

[93] H.-P. Rust, T. König, G. H. Simon, M. Nowicki, V. Simic-Milosevic, G. Thielsch, M. Heyde, and H.-J. Freund, A portable microevaporator for low temperature single atom studies by scanning tunneling and dynamic force microscopy., *Rev. Sci. Instrum.*, **2009**, 80, 11, 113705 1–4.

[94] W. E. Kaden, C. Büchner, L. Lichtenstein, S. Stuckenholz, F. Ringleb, M. Heyde, M. Sterrer, H.-J. Freund, L. Giordano, G. Pacchioni, C. J.

Nelin, and P. S. Bagus, Understanding Surface Core-Level Shifts using the Auger Parameter; a study of Pd atoms adsorbed on SiO2 ultra-thin films, *Phys. Rev. B*, **2014**, 89, 11, 115436 1–8.

[95] S. Ulrich, N. Nilius, H.-J. Freund, U. Martinez, L. Giordano, and G. Pacchioni, Realization of an atomic sieve : Silica on Mo(112), *Surf. Sci.*, **2009**, 603, 8, 1145–1149.

[96] A. Bondi, van der Waals Volumes and Radii, *J. Phys. Chem.*, **1964**, 68, 3, 441–451.

[97] P. Schlexer, L. Giordano, and G. Pacchioni, Adsorption of Li, Na, K, and Mg Atoms on Amorphous and Crystalline Silica Bilayers on Ru(0001): A DFT Study, *J. Phys. Chem. C*, **2014**, 118, 15884–15897.

[98] E. Emmez, B. Yang, S. Shaikhutdinov, and H.-J. Freund, Permeation of a Single-Layer SiO2 Membrane and Chemistry in Confined Space, *J. Phys. Chem. C*, **2014**, 118, 29034–29042.

[99] P. Schlexer, G. Pacchioni, R. Włodarczyk, and J. Sauer, CO Adsorption on a Silica Bilayer Supported on Ru(0001), *Surf. Sci.*, **2016**, 648, 2–9.

[100] B. Yang, S. Shaikhutdinov, and H. J. Freund, Ultrathin silicatene/silicon-carbide hybrid film on a metal substrate, *Surf. Sci.*, **2015**, 632, 9–13.

[101] S. Morita, F. J. Giessibl, and R. Wiesendanger, Noncontact Atomic Force Microscopy - Volume 2, 1st ed. Springer-Verlag Berlin Heidelberg, **2009**.

[102] K. S. Novoselov, A. K. Geim, S. V Morozov, D. Jiang, Y. Zhang, S. V Dubonos, I. V Grigorieva, and A. A. Firsov, Electric Field Effect in Atomically Thin Carbon Films, *Science*, **2004**, 306, 5696, 666–669.

[103] O. Shoseyof and I. Levy, Eds., NanoBioTechnology BioInspired Devices and Materials of the Future, 1st ed. Humana Press, **2008**.

[104] S. Zhang, Fabrication of novel biomaterials through molecular self-assembly, *Nat. Biotechnol.*, **2003**, 21, 10, 1171–1178.

[105] Z. Tang, Z. Zhang, Y. Wang, S. C. Glotzer, and N. A. Kotov, Self-Assembly of CdTe Nanocrystals into Free-Floating Sheets, *Science*, **2006**, 314, 274–278.

[106] J.-Y. Hong, Y. C. Shin, A. Zubair, Y. Mao, T. Palacios, M. S. Dresselhaus, S. H. Kim, and J. Kong, A Rational Strategy for Graphene Transfer on Substrates with Rough Features, *Adv. Mater.*, **2016**, 1–11.

[107] A. Gurarslan, Y. Yu, L. Su, Y. Yu, F. Suarez, S. Yao, Y. Zhu, M. Ozturk,

Y. Zhang, and L. Cao, Surface-Energy-Assisted Perfect Transfer of Centimeter-Scale Monolayer and Few-Layer MoS2 Films onto Arbitrary Substrates, *ACS Nano*, **2014**, 8, 11, 11522–11528.

[108] X. Li, Y. Zhu, W. Cai, M. Borysiak, B. Han, D. Chen, R. D. Piner, L. Colomba, and R. S. Ruoff, Transfer of large-area graphene films for high-performance transparent conductive electrodes, *Nano Lett.*, **2009**, 9, 12, 4359–4363.

[109] S. Kim, S. Shin, T. Kim, H. Du, M. Song, C. Lee, K. Kim, S. Cho, D. H. Seo, and S. Seo, Use of lower-molecular-weight polymethylmethacrylate improves graphene wet transfer, *Carbon*, **2016**, 98, 352–357.

[110] Y. Hernandez, V. Nicolosi, M. Lotya, F. M. Blighe, Z. Sun, S. De, I. T. McGovern, B. Holland, M. Byrne, Y. K. Gun'Ko, J. J. Boland, P. Niraj, G. Duesberg, S. Krishnamurthy, R. Goodhue, J. Hutchison, V. Scardaci, A. C. Ferrari, and J. N. Coleman, High-yield production of graphene by liquid-phase exfoliation of graphite., *Nat. Nanotechnol.*, **2008**, 3, 9, 563–568.

[111] A. Gupta, T. Sakthivel, and S. Seal, Recent Development in 2D Materials Beyond Graphene, *Prog. Mater. Sci.*, **2015**, 73, 44–126.

[112] M. Osada and T. Sasaki, Two-Dimensional Dielectric Nanosheets: Novel Nanoelectronics From Nanocrystal Building Blocks, *Adv. Mater.*, **2012**, 24, 2, 210–228.

[113] M. Lotya, P. J. King, U. Khan, S. De, and J. N. Coleman, High-Concentration, Surfactant-Stabilized Graphene Dispersions, *ACS Nano*, **2010**, 4, 6, 3155–3162.

[114] U. Khan, A. O'Neill, M. Lotya, S. De, and J. N. Coleman, High-concentration solvent exfoliation of graphene, *Small*, **2010**, 6, 7, 864–871.

[115] E.-Y. Choi, W. S. Choi, Y. B. Lee, and Y.-Y. Noh, Production of graphene by exfoliation of graphite in a volatile organic solvent, *Nanotechnology*, **2011**, 22, 36, 365601.

[116] A. Gölzhauser, C. Nottbohm, and A. Beyer, Method for Transferring a Nanolayer, 8,377,243 B2, 2013.

[117] X. Li, W. Cai, J. An, S. Kim, J. Nah, D. Yang, R. Piner, A. Velamakanni, I. Jung, E. Tutuc, S. K. Banerjee, L. Colombo, and R. S. Ruoff, Large-Area Synthesis of High-Quality and Uniform Graphene Films on Copper Foils, *Science*, **2009**, 324, 5932, 1312–1314.

[118] X. Li, W. Cai, J. An, S. Kim, J. Nah, D. Yang, R. Piner, A. Velamakanni, I. Jung, E. Tutuc, S. K. Banerjee, L. Colombo, and R. S. Ruoff, Large-

Area Synthesis of High-Quality and Uniform Graphene Films on Copper Foils, *Science*, **2009**, 324, 5932, 1312–1314.

[119] C. Gong, H. C. Floresca, D. Hinojos, S. McDonnell, X. Qin, Y. Hao, S. Jandhyala, G. Mordi, J. Kim, L. Colombo, R. S. Ruoff, M. J. Kim, K. Cho, R. M. Wallace, and Y. J. Chabal, Rapid Selective Etching of PMMA Residues from Transferred Graphene by Carbon Dioxide, *J. Phys. Chem. C*, **2013**, 117, 44, 23000–23008.

[120] G. Borin Barin, Y. Song, I. de Fátima Gimenez, A. G. Souza Filho, L. S. Barreto, and J. Kong, Optimized graphene transfer: Influence of polymethylmethacrylate (PMMA) layer concentration and baking time on graphene final performance, *Carbon*, **2015**, 84, 82–90.

[121] S. Bae, H. Kim, Y. Lee, X. Xu, J.-S. Park, Y. Zheng, J. Balakrishnan, T. Lei, H. Ri Kim, Y. Il Song, Y.-J. Kim, K. S. Kim, B. Ozyilmaz, J.-H. Ahn, B. H. Hong, and S. Iijima, Roll-to-roll production of 30-inch graphene films for transparent electrodes, *Nat Nano*, **2010**, 5, 8, 574–578.

[122] A. Pirkle, J. Chan, A. Venugopal, D. Hinojos, C. W. Magnuson, S. McDonnell, L. Colombo, E. M. Vogel, R. S. Ruoff, and R. M. Wallace, The effect of chemical residues on the physical and electrical properties of chemical vapor deposited graphene transferred to SiO2, *Appl. Phys. Lett.*, **2011**, 99, 12, 10–13.

[123] J.-N. Longchamp, C. Escher, and H.-W. Fink, Ultraclean freestanding graphene by platinum-metal catalysis, *J. Vac. Sci. Technol. B*, **2013**, 31, 2, 020605 1–3.

[124] B. Cappella, H. Sturm, and S. M. Weidner, Breaking polymer chains by dynamic plowing lithography, *Polymer*, **2002**, 43, 16, 4461–4466.

[125] M. F. Kemmere, M. W. A. Kuijpers, and J. T. F. Keurentjes, Reaction Calorimetry for the Development of Ultrasound-Induced Polymerization Processes in CO2-Expanded Fluids, *Macromol. Symp.*, **2007**, 248, 1, 182–188.

[126] L. Tong, R. R. Gattass, J. B. Ashcom, S. He, J. Lou, M. Shen, I. Maxwell, and E. Mazur, Subwavelength-diameter silica wires for low-loss optical wave guiding., *Nature*, **2003**, 426, 6968, 816–819.

[127] A. Reina, H. Son, L. Jiao, B. Fan, M. S. Dresselhaus, Z. Liu, and J. Kong, Transferring and Identification of Single- and Few-Layer Graphene on Arbitrary Substrates, *J. Phys. Chem. C*, **2008**, 112, 46, 17741–17744.

[128] R. F. Egerton, Electron Energy-Loss Spectroscopy in the Electron Microscope, 1st ed. Springer-Verlag Berlin Heidelberg, **2011**.

[129] M. Schade, N. Geyer, B. Fuhrmann, F. Heyroth, and H. S. Leipner, High-resolution analytical electron microscopy of catalytically etched silicon nanowires, *Appl. Phys. A*, **2009**, 95, 2, 325–327.

[130] W. Windl, T. Liang, S. Lopatin, and G. Duscher, Modeling and characterization of atomically sharp "perfect" Ge/SiC2 interfaces, *Mater. Sci. Eng. B*, **2004**, 114–115, 156–161.

[131] S. Schamm, R. Berjoan, and P. Barathieu, Study of the chemical and structural organization of SIPOS films at the nanometer scale by TEM-EELS and XPS, *Mater. Sci. Eng. B*, **2004**, 107, 1, 58–65.

[132] P. E. Batson, Current trends for EELS studies in physics, *Microsc. Microanal. Microstruct.*, **1991**, 2, 2–3, 395–402.

[133] D. A. Muller, T. Sorsch, S. Moccio, F. H. Baumann, K. Evans-Lutterodt, and G. Timp, The electronic structure at the atomic scale of ultrathin gate oxides, *Nature*, **1999**, 399, June, 758–761.

[134] J. C. Meyer, C. O. Girit, M. F. Crommie, and A. Zettl, Hydrocarbon lithography on graphene membranes, *Appl. Phys. Lett.*, **2008**, 92, 12, 123110 1–3.

[135] S. J. Chae, F. Güneş, K. K. Kim, E. S. Kim, G. H. Han, S. M. Kim, H. Shin, S. M. Yoon, J. Y. Choi, M. H. Park, C. W. Yang, D. Pribat, and Y. H. Lee, Synthesis of large-area graphene layers on poly-nickel substrate by chemical vapor deposition: Wrinkle formation, *Adv. Mater.*, **2009**, 21, 22, 2328–2333.

[136] S. Lizzit, R. Larciprete, P. Lacovig, K. L. Kostov, and D. Menzel, Ultrafast Charge Transfer at Monolayer Graphene Surfaces with Varied Substrate Coupling Ultrafast Charge Transfer at Monolayer Graphene Surfaces with Varied Substrate Coupling, *Nano*, **2013**, 5, 4359–4366.

[137] M. Corso, W. Auwärter, M. Muntwiller, A. Tamai, T. Greber, and J. Osterwalder, Boron Nitride Nanomesh, *Science*, **2004**, 303, 217–220.

[138] H. A. Schaeffer and R. Langfeld, Werkstoff Glas, 1st ed. Berlin, Heidelberg: Springer Berlin Heidelberg, **2014**.

[139] T. König, G. H. Simon, L. Heinke, L. Lichtenstein, and M. Heyde, Defects in oxide surfaces studied by atomic force and scanning tunneling microscopy, *Beilstein J. Nanotechnol.*, **2011**, 2, 1–14.

Danksagung

Zu dieser Arbeit haben viele Menschen auf vielfältige Art beigetragen. Einige möchte ich hier benennen und meinen Dank ausdrücken. Zuerst danke ich meinem Doktorvater, Hans-Joachim Freund, für sein Vertrauen in mich und die zahlreichen Möglichkeiten zum Lernen und Wachsen. Auch Klaus Rademann bin ich sehr dankbar für die Unterstützung und hilfreichen Ratschläge während meiner gesamten Promotion. Von Bodil Holst konnte ich viel lernen und ich danke ihr für die gute Zusammenarbeit, bisher und sicher auch weiterhin.

Der Alltag der Forschung ist ein Auf und Ab, aber auf hoher See war ich nie allein. Von Markus Heyde habe ich vieles gelernt, vor allem aber, ausgefallenen Ideen eine Chance zu geben. Und Steffi, ohne dich wär ich bestimmt seekrank geworden. Den übrigen Kollegen der SPM-Gruppe und der CP-Abteilung danke ich für den guten Zusammenhalt und die angenehme Arbeitsatmosphäre.

Für ganz konkrete Beiträge zu meiner Arbeit möchte ich noch einzelne Kollegen hervorheben: Liwei Liu und Philomena Schlexer danke ich für die Zusammenarbeit in der Netzwerkstudie, Leonid Lichtenstein für die Zusammenarbeit bei den Adsorptionsexperimenten, Kristen Burson und Burkhard Kell danke ich für Messungen mit dem CypherAFM, Zhu-Jun Wang und Marc Willinger danke ich für ESEM und TEM Messungen.

Ich möchte meinen Eltern, Johannes und Jule danken; mit eurer beständigen Unterstützung und Ehrlichkeit seid ihr stets mein Kompass.

Selbständigkeitserklärung

Ich erkläre hiermit, dass ich die vorliegende Arbeit selbständig und nur unter Verwendung der angegebenen Literatur und Hilfsmittel angefertigt habe.

Berlin, den Christin Büchner